

**QUASI BALLISTIC ELECTRON REFLECTION IN  
LOW-DIMENSIONAL SEMICONDUCTOR FOR  
TERAHERTZ SIGNAL GENERATION**

By

**BADRUL IMAN ABIDIN**

A dissertation submitted to the Department of Electrical and Electronic  
Engineering,  
Lee Kong Chian Faculty of Engineering and Science,  
Universiti Tunku Abdul Rahman,  
in partial fulfillment of the requirements for the degree of  
Master of Science  
April 2019

## **ABSTRACT**

### **QUASI BALLISTIC ELECTRON REFLECTION IN LOW-DIMENSIONAL SEMICONDUCTOR FOR TERAHERTZ SIGNAL GENERATION**

**Badrul Iman Abidin**

Graphene is in the forefront of low dimensional materials due to its high electron mobility in comparison to bulk materials because it has a Dirac cone band structure. Single layer silicon, silicene also has a similar Dirac cone structure as graphene. Manipulation of these materials gather a lot of interest from researchers. To investigate the electron transport properties in a monolayer free-standing graphene and silicene, an Analytical Band Monte Carlo (AMC) model has been developed. The energy band structure utilised in this model focused on the linear band dispersion close to the Dirac point. The AMC model is validated via comparison to the Full Band Monte Carlo (FMC) results such as electron mobility and drift velocity. In comparison to the FMC method, the AMC model requires significantly less computational time.

The effects of carrier concentration in monolayer graphene and silicene were investigated in this study. It is found that a higher carrier concentration will degrade the steady-state drift velocity. Additionally, the carrier concentration has a noticeable effect on the electron mobility and mean free path. Higher carrier concentrations result in lower electron mobility and longer

mean free path. This is attributed to the collective effects of degeneracy and the dependency of the scattering rate and electrons energies. The electron mobility and mean free path for silicene are far inferior to graphene due to the higher phonon scattering rate. Particularly, graphene has negligible low optical and acoustic out-of-plane (ZA and ZO) scattering compared to silicene.

The AMC model was further extended to explore the possibility of THz signal generation by using Quasi-Ballistic Electron Reflection (QBER). As a proof-of-concept, a numerical model was developed to study the electron oscillation in graphene or silicene confined between two energy barrier of infinite height. Due to the high electron mobility and long mean free path, QBER device based on graphene is able to produce radiation with peak frequency up to 1.6 THz and the frequency of the radiation can be varied by controlling the device length. On the other hand, the simulation results show that silicene is not a promising material in producing THz signal using the QBER concept due to short mean free path and high phonon scattering rate which lead to rapid loss of electron energy during the transport.

## LIST OF PUBLICATIONS

### Peer Reviewed Paper (ISI Indexed Journal)

**Abidin, B.I.**, Yeoh, K.H., Ong, D.S. and Yong, T.K., 2017. Effects of Carrier Concentrations on The Charge Transport Properties in Monolayer Silicene. *Journal of Physics D: Applied Physics*, vol. 50, no. 425103, 6pp.

### Paper in Conference Proceeding

**Abidin, B.I.**, Yeoh, K.H., Yong, T.K. and Ong, D.S., 2017. THz Radiation in Graphene Based on Quasi-Ballistic Electron Reflection. 2017 IEEE Asia Pacific Conference on Postgraduate Research in Microelectronics and Electronics (PrimeAsia), Kuala Lumpur, Malaysia, pp. 13-16. (***Best Paper Award***)

## **ACKNOWLEDGEMENTS**

I would like to express my sincere gratitude to my supervisor, Dr. Yeoh Keat Hoe and my co-supervisor, Prof. Ong Duu Sheng and Dr. Yong Thian Khok for their direction, assistance, and guidance throughout the MSc period, leading to the submission of this dissertation. It is difficult to imagine what will happen without their valuable inputs to my MSc research. In particular, Prof Ong who willing to travel from Multimedia University to UTAR and keep provide critical input and new idea throughout my research. I also like to acknowledge my friend who helped me all these years, providing moral support and food when the hard time came by. Last but not least, I offer my deepest appreciation to those who supported me in any way during the completion of this work.

## APPROVAL SHEET

This dissertation entitled “QUASI BALLISTIC ELECTRON REFLECTION IN LOW-DIMENSIONAL SEMICONDUCTOR FOR TERAHERTZ SIGNAL GENERATION” was prepared by BADRUL IMAN ABIDIN and submitted as partial fulfillment of the requirements for the degree of Master of Science at Universiti Tunku Abdul Rahman.

Approved by:

---

(Dr. YEOH KEAT HOE)

Date: .....

Supervisor

Department of Electrical and Electronic Engineering  
Lee Kong Chian Faculty of Engineering and Science  
Universiti Tunku Abdul Rahman

---

(Dr. YONG THIAN KHOK)

Date: .....

Co-supervisor

Department of Electrical and Electronic Engineering  
Lee Kong Chian Faculty of Engineering and Science  
Universiti Tunku Abdul Rahman

**FACULTY OF ENGINEERING AND SCIENCE**  
**UNIVERSITI TUNKU ABDUL RAHMAN**

Date: 15 August 2018

**SUBMISSION OF DISSERTATION**

It is hereby certified that **BADRUL IMAN ABIDIN** (ID No: **16UEM06274** ) has completed this dissertation entitled “QUASI BALLISTIC ELECTRON REFLECTION IN LOW-DIMENSIONAL SEMICONDUCTOR FOR TERAHERTZ SIGNAL GENERATION” under the supervision of Dr. YEOH KEAT HOE (Supervisor) from the Department of Electrical and Electronic Engineering, Lee Kong Chian Faculty of Engineering and Science, and Dr. YONG THIAN KHOK (Co-Supervisor) from the Department of Electrical and Electronic Engineering, Lee Kong Chian Faculty of Engineering and Science.

I understand that University will upload softcopy of my dissertation in pdf format into UTAR Institutional Repository, which may be made accessible to UTAR community and public.

Yours truly,

---

**(BADRUL IMAN ABIDIN)**

## DECLARATION

I hereby declare that the dissertation is based on my original work except for quotations and citations which have been duly acknowledged. I also declare that it has not been previously or concurrently submitted for any other degree at UTAR or other institutions.

\_\_\_\_\_  
(BADRUL IMAN ABIDIN)

Date: \_\_\_\_\_

## TABLE OF CONTENTS

	<b>Page</b>
<b>ABSTRACT</b>	<b>ii</b>
<b>LIST OF PUBLICATIONS</b>	<b>iv</b>
<b>ACKNOWLEDGEMENTS</b>	<b>v</b>
<b>APPROVAL SHEET</b>	<b>vi</b>
<b>DECLARATION</b>	<b>viii</b>
<b>LIST OF TABLES</b>	<b>xi</b>
<b>LIST OF FIGURES</b>	<b>xii</b>
<b>LIST OF ABBREVIATIONS</b>	<b>xvii</b>
<b>CHAPTER</b>	
<b>1.0 INTRODUCTION</b>	<b>1</b>
1.1 Background	1
1.2 Motivations and Objectives	4
1.3 Dissertation Overview	5
<b>2.0 TERAHERTZ SIGNAL GENERATION AND LOW DIMENSIONAL MATERIALS</b>	<b>7</b>
2.1 Introduction	7
2.2 Review of THz Signal Generation	8
2.3 Low Dimensional Materials	17
2.3.1 Graphene	18
2.3.2 Silicene	21
2.4 Quasi Ballistic Electron Reflection (QBER)	26
<b>3.0 CHARGE TRANSPORT THEORY AND MONTE CARLO METHOD</b>	<b>29</b>
3.1 Introduction	29
3.2 Analytical band Structure	29
3.3 Scattering Mechanism	32
3.4 Monte Carlo Method	35
3.5 Degeneracy Effect	39
3.6 Monte Carlo Model for QBER Device	41
<b>4.0 MODELLING OF CHARGE TRANSPORT IN TWO-DIMENSIONAL MATERIALS</b>	<b>46</b>
4.1 Introduction	46
4.2 The Applicability of Analytical Monte Carlo	47
4.3 Electron Transport in Graphene	50
4.4 Electron Transport in Silicene	60
4.5 Summary	69

<b>5.0</b>	<b>TERAHERTZ SIGNAL GENERATION IN TWO-DIMENSIONAL MATERIALS</b>	<b>70</b>
5.1	Introduction	70
5.2	Device Structure and Simulation Approach	71
5.3	Graphene Based Structure	73
	5.3.1 Square Wave Bias Excitation	73
	5.3.2 Sinusoidal Wave Bias Excitation	80
5.4	Silicene Based Structure	85
	5.4.1 Square Wave Bias Excitation	86
5.5	Summary	90
<b>6.0</b>	<b>CONCLUSIONS AND RECOMMENDATIONS</b>	<b>92</b>
6.1	Conclusions	92
6.2	Future Works	94
<b>7.0</b>	<b>REFERENCES</b>	<b>96</b>

## LIST OF TABLES

<b>Tables</b>		<b>Page</b>
2.1	Some of the reported THz systems and its operating frequency using several technologies. P, E and C letter after the device is to indicate either the method that the device used falls into photonic, electronic or combination (hybrid) method. Respectively, QCL and UTC-PD denotes quantum cascade laser and uni-travelling carrier photodiode	16
2.2	Comparison between mechanical and electronic properties of graphene and silicene at 300 K	26
4.1	Table 4.1: Graphene and silicene simulation parameters used in this work. These parameters are taken from Hirai et al. (2014) <sup>1</sup> and Yeoh et al (2016) <sup>2</sup> .	48
4.2	Comparison between electron mobility of the graphene obtained from this study with other semiconductor materials	55

## LIST OF FIGURES

Figures		Page
2.1	THz region in electromagnetic spectrum loosely defined as frequency in the range of 100 GHz to 10 THz.	8
2.2	Typical device structure for a quantum cascade laser (Hangyo, 2015).	10
2.3	Schematic setup of THz generation using optical rectification in an organic material DAST and its detection is using a GaP sensor, quarter wave plate (QWP), Wollaston prism (WP) and a photodiode detector (PD) (Hauri et al., 2011).	11
2.4	Schematic diagram of THz-FEL with wiggler and electron bunch source (Liu, 2018). The wiggler is a magnetic field distorter in the electron path.	11
2.5	Conceptual design of a vacuum electron amplifier that includes the electron beam source, interaction circuit, confinement magnet and radiation port (Barker, 2005).	12
2.6	A typical layer structure of resonant tunnelling diode and its current-voltage profile (Asada and Suzuki, 2011).	14
2.7	UTC-PD band diagram (Ito et al., 2005).	15
2.8	(a) Honeycomb lattice arrangement found in graphene. $A$ and $B$ is the lattice point, $a_i$ is the lattice vector and $\delta_i$ is the sub-lattice vector. (b) The $K$ and $K'$ point in the hexagonal Brillouin zone where the Dirac points are located. The bond length $a_n$ of C-C atoms is 1.43 Å (Harrison, 2012).	19
2.9	(a) Top view and (b) side view of the monolayer graphene atomic structure. (c) Electronic band structures of monolayer graphene along the high symmetry direction in the Brillouin zone.	20
2.10	(a) Top view and (b) side view of the monolayer silicene atomic structure. (c) Electronic band structures of monolayer silicene along the high symmetry direction in the Brillouin zone.	22
2.11	Fabrication process of a back-gate silicene FET. Illustration adapted from Tao et al. (2015).	25

2.12	Schematic illustration of QBER mechanism for the carrier in a simplified (a) E-k diagram and (b) potential well for the first half of the AC bias. For the second half of the AC cycle, the E-k diagram and potential well is illustrated in (c) and (d) respectively.	28
3.1	Flow chart of analytical band Monte Carlo simulation.	36
3.2	Rejection routine in the ensemble Monte Carlo model.	41
3.3	Analytical band Monte Carlo simulation flow for QBER device.	44
4.1	(a) Drift velocity against applied electric field for suspended monolayer graphene in comparison to the works done by Li et al. (2010; 2011). (b) The scattering parameters used to calculate the silicene drift velocity are taken from Yeoh et al. (2016). The results are exactly the same as those published by Yeoh et al. since the same Monte Carlo code was used to calculate the drift velocity in this work.	49
4.2	Energy band diagram for monolayer (a) graphene and (b) silicene. The inset in (a) and (b) shows expanded view of the Dirac cone. As shown by the red line, linearity of the band structure is maintained at 1eV for graphene and 0.6 eV for silicene.	49
4.3	Drift velocity against applied electric field with carrier concentration ranging from $10^{11} \text{ cm}^{-2}$ to $10^{13} \text{ cm}^{-2}$ .	51
4.4	Average energy against applied electric field with carrier concentration ranging from $10^{11} \text{ cm}^{-2}$ to $10^{13} \text{ cm}^{-2}$ .	51
4.5	Electron scattering rate for graphene at room temperature for acoustic phonon and optical phonon. AP and OP denotes acoustic phonon optical phonon respectively.	52
4.6	Electron energy distribution for suspended monolayer graphene at applied fields of 1 kV/cm, 10 kV/cm and 20 kV/cm. Subplot in (b), (c) and (d) shows the same plot that overlapping 1 kV/cm, 10 kV/cm and 20 kV/cm with different carrier concentrations. Brown, orange, purple and blue refer respectively to $1 \times 10^{11} \text{ cm}^{-2}$ , $1 \times 10^{12} \text{ cm}^{-2}$ , $5 \times 10^{12} \text{ cm}^{-2}$ and $1 \times 10^{13} \text{ cm}^{-2}$ .	53
4.7	Standard deviation of $k_x$ as a function of electric field and carrier concentration for suspended monolayer graphene.	54
4.8	Electron mobility of suspended monolayer graphene as a function of carrier concentration.	55

4.9	Electron drift velocity against travelled distance in a monolayer graphene. In (a) the carrier concentration is fixed at $1 \times 10^{12} \text{ cm}^{-2}$ whereas in (b) the applied electric field is fixed at 10 kV/cm.	57
4.10	Mean free path of a suspended monolayer graphene.	58
4.11	Electron drift velocity against time with a fixed (a) carrier concentration at $1 \times 10^{12} \text{ cm}^{-2}$ and (b) applied field at 10 kV/cm in a suspended monolayer graphene.	59
4.12	Drift velocity against applied electric field with carrier concentration ranging from $10^{11} \text{ cm}^{-2}$ to $10^{13} \text{ cm}^{-2}$ .	60
4.13	Average energy attained by the electrons as a function electric field with carrier concentration ranging from $10^{11} \text{ cm}^{-2}$ to $10^{13} \text{ cm}^{-2}$ .	61
4.14	Electron scattering rates in silicene at room temperature for different phonon modes. ZA, TA, LA, ZO, TO and LO denote out-of-plane acoustic, transverse acoustic, longitudinal acoustic, out-of-plane optical, transverse optical and longitudinal optical respectively.	62
4.15	Electron energy distribution in a suspended monolayer silicene with applied fields of 1 kV/cm, 20 kV/cm and 40 kV/cm. The distribution was simulated with 105 particles and mesh size of 50 meV. The energy distribution is skewed to higher energy level with a higher carrier concentration due to degeneracy effect. Subplot in (b), (c) and (d) shows the same plot that overlapping 1 kV/cm, 20 kV/cm and 40 kV/cm with different carrier concentrations. Brown, orange, purple and blue refer respectively to $1 \times 10^{11} \text{ cm}^{-2}$ , $1 \times 10^{12} \text{ cm}^{-2}$ , $5 \times 10^{12} \text{ cm}^{-2}$ and $1 \times 10^{13} \text{ cm}^{-2}$ .	63
4.16	Standard deviation of $k_x$ against the electric field and carrier concentration for suspended monolayer silicene.	64
4.17	Electron mobility of a suspended monolayer silicene as a function of carrier concentration.	65
4.18	(a) Electron drift velocity in a suspended monolayer silicene againsts the travelled distance for various electric fields with fixed carrier density $1 \times 10^{12} \text{ cm}^{-2}$ . (b) Comparison of the electron drift velocities attained with carrier concentrations varied from $1 \times 10^{11} \text{ cm}^{-2}$ to $1 \times 10^{13} \text{ cm}^{-2}$ . The electric field is fixed at 20 kV/cm.	66
4.19	Electron mean free path of suspended monolayer silicene againsts the carrier concentrations for various applied electric fields.	67

4.20	Time evolution of instantaneous drift velocity of suspended monolayer silicene with (a) carrier concentration of $1 \times 10^{12} \text{ cm}^{-2}$ (b) carrier concentrations varied from $1 \times 10^{11} \text{ cm}^{-2}$ to $1 \times 10^{13} \text{ cm}^{-2}$ with fixed electric field at 20 kV/cm.	68
5.1	Schematic diagram of the quasi-ballistic electrons experiencing multiple reflection at the potential barriers.	71
5.2	Blue lines indicate the temporal evolution of electron current under $\pm 7 \text{ V}$ square wave bias (black dotted line) at switching frequency of 100 GHz. The device length is varied from 5 $\mu\text{m}$ to 7 $\mu\text{m}$ .	74
5.3	Expanded view of the electron current oscillation in Figure 5.2 for the first-half cycle of the square-wave.	75
5.4	(a) Fractional electron reflection per fs. The applied bias is $\pm 7 \text{ V}$ with switching frequency 100 GHz. The device length is 5 $\mu\text{m}$ . (b) Schematic diagram of the electrons in graphene confined between two potential barriers.	76
5.5	Electron density distribution as a function of position and propagation time. The device is bias with $\pm 7 \text{ V}$ square wave potential. The switching frequency is 100 GHz and the device length is 5 $\mu\text{m}$ .	77
5.6	Radiation spectra for the graphene QBER devices with $\pm 7 \text{ V}$ excitation signal at switching frequency of 100 GHz.	78
5.7	Peak radiation frequency against device length at different bias.	79
5.8	Blue lines indicate the temporal evolution of electron current under $\pm 10 \text{ V}_p$ ( $7 \text{ V}_{\text{rms}}$ ) sinusoid potential (black dotted line) at switching frequency of 100 GHz. The device length is varied from 5 $\mu\text{m}$ to 7 $\mu\text{m}$ .	80
5.9	Expanded view of the electron current oscillation in Figure 5.9 for the first-half cycle of the sinusoid bias.	81
5.10	(a) Fractional electron reflection per fs. The applied bias is $\pm 10 \text{ V}_p$ ( $10 \text{ V}_{\text{rms}}$ ) sinusoid signal with switching frequency of 100 GHz. The device length is 5 $\mu\text{m}$ . (b) Schematic diagram of the electrons in graphene confined between two potential barriers.	82
5.11	Electron density distribution as a function of position and propagation time. The device is bias with $\pm 10 \text{ V}_p$ ( $10 \text{ V}_{\text{rms}}$ ) sinusoid signal. The switching frequency is 100 GHz and the device length is 5 $\mu\text{m}$ .	83

5.12	Radiation spectra for the graphene QBER devices with $\pm 10 V_p$ ( $7 V_{rms}$ ) excitation signal at switching frequency of 100 GHz.	84
5.13	Peak radiation frequency against device length at different bias.	85
5.14	Blue lines indicate the temporal evolution of electron current under $\pm 0.2 V$ square wave bias (black dotted line) at switching frequency of 100 GHz. The device length is varied from 50 nm to 200 nm.	86
5.15	(a) Fractional electron reflection per fs. The applied bias is $\pm 0.2 V$ square-wave with switching frequency of 100 GHz. The device length is 100 nm. (b) Schematic diagram of the electrons in silicene confined between two potential barriers.	88
5.16	Electron density distribution as a function of position and propagation time. The device is biased with $\pm 0.2 V$ . The switching frequency is 100 GHz and the device length is 100 nm.	88
5.17	Radiation spectra of the silicene based devices at different device lengths.	89

## LIST OF ABBREVIATIONS

AMC	Analytical band Monte Carlo
AP	Acoustic phonon
CVD	Chemical vapour deposition
DAST	4- <i>N</i> , <i>N</i> -dimethylamino-4'- <i>N'</i> -methyl-stilbazolium tosylate
DFT	Density functional theory
EM	Electromagnetic
ERL	Energy recovery linac
FEL	Free electron laser
FET	Field effect transistor
FMC	Full band Monte Carlo
GaAs	Gallium arsenide
GaP	Gallium phosphide
InGaAs	Indium gallium arsenide
IR	Infrared
LA	Lateral acoustic phonon mode
LO	Lateral optical phonon mode
PD	Photodiode detector
QBER	Quasi-ballistic electron reflection
QCL	Quantum cascade laser
QWP	Quarter wave plate
OP	Optical phonon
RTD	Resonant tunnelling diode
Si	Silicon

TA	Transverse acoustic phonon mode
TO	Transverse optical phonon mode
UTC-PD	Uni-travelling carrier photodiode
UV	Ultraviolet
VED	Vacuum electronics device
WP	Wollaston prism
ZA	Out-of-plane acoustic phonon mode
ZO	Out-of-plane optical phonon mode
$E_D$	Deformation potential for elastic scattering
$E_f$	Deformation potential for inelastic scattering
$\rho_s$	Mass density
$v_f$	Fermi velocity
$v_s$	Sound velocity

# CHAPTER 1

## INTRODUCTION

### 1.1 Background

Terahertz (THz) radiation has various unique properties such as non-ionizing, attenuates in water and able to carry data at extremely fast speed. Its unique features allow for detailed material characterization, as it is able to probe at picosecond scale which is one of the key points of THz time-domain spectroscopy. This allows for superior spatial resolution image than microwaves (Mittleman, 2018). Over the years, many research works were carried out to produce THz radiation. The commonly used approaches were the photonic methods such as laser, optical rectification in nonlinear crystal, synchrotron infrared beamlines and photoconductive antennas (Dhillon et al., 2017). Technically, the photonic methods covered above 1 THz with output power of at least 1 mW (Booske et al., 2011). However, THz sources based on these methods were typically bulky. Integration to the modern small electronic device is physically impossible.

Another approaches of generating THz radiation were by using electronic methods such as resonant tunnelling diode (RTD), uni-travelling carrier photodiode (UTC-PD) and spintronic emitter (Asada, Suzuki and Kishimoto, 2008; Ducournau et al., 2014; Seifert et al., 2017). These methods

enable the realization of a compact and portable THz source. However, its applications were limited by low frequency and low output power (i.e. typically around 500 GHz and 20  $\mu$ W) (Asada, Suzuki and Kishimoto, 2008; Dhillon et al., 2017). Attempt to improve the radiation frequency and output powers of the electronic-based THz sources are currently an active area of research.

Low dimensional materials have garnered attention from researchers since the discovery of graphene (Novoselov et al., 2004). Graphene has a linear band structure near the Dirac point at its hexagonal Brillouin zone which results in massless electron. This unique feature is absent in the bulk semiconductor and it leads to a very high electron mobility, a physical property that is highly desirable for high speed electronics applications. However, graphene which consists of carbon may have difficulties in integrating into the current microelectronics industry which is based on silicon (Houssa, Dimoulas and Molle, 2015). This short coming has motivated many researchers to look for other two-dimensional (2D) materials similar to graphene. One of these materials are monolayer silicon or widely known as silicene (Vogt et al., 2012). Silicon and carbon share the same elemental group in the periodic table and therefore silicene is expected to share many similarities with graphene. Similar to graphene, Dirac cone exist in silicene and both of these materials exist in the form of honeycomb structure. More importantly, silicene was experimentally demonstrated by few research groups over the past few years (Houssa, Dimoulas and Molle, 2015).

Integrating 2D materials into current technology has been in progress in various areas of electronic applications. A theoretical study is very important before implementing an experimental setup using these materials. First-principle approaches such as density functional theory (DFT) and full-band Monte Carlo Method (FMC) are some of the commonly used techniques to simulate the material properties. However, these methods are computationally expensive. Another approach is the analytical band Monte Carlo (AMC) which offers a faster computational time with good accuracy. In contrast to the FMC method, the band structure and scattering mechanism in AMC method are modelled using analytical equations which can reduce the computational time.

Quasi-ballistic electron reflection (QBER) is a new approach in generating THz radiation which was first proposed by (Ong and Hartnagel, 2007; 2008; 2015). Theoretically, this concept was implemented on bulk compound semiconductor such as InAlAs/InGaAs/InAlAs and able to generate THz signal up to 4 THz. It based on the fast electron oscillation driven by alternating bias (AC) signal. In this manner, the electron was confined between two wide bandgap materials. This concept holds promising potential towards the development of compact THz source and it had not been tested on a 2D material.

In this dissertation, the possibility of generating THz radiation using QBER concept was explored for low dimensional materials such as graphene and silicene. A Monte Carlo frame-work based on analytical band was developed to investigate the charge transport properties of silicene and graphene.

Then, this model was modified to simulate the QBER effect for electrons confined between two wide bandgap materials. From this simulation, the THz signal radiation was calculated and analysed.

## **1.2 Motivations and Objectives**

Currently, THz radiation sources that are capable of producing radiation beyond 1 THz are usually bulky and physically unable to fit into the modern electronic devices. Developing a compact and portable THz source is highly desirable for applications like data transfer, illicit material detection, non-destructive test, ultrafast spectroscopy and fault detection in microelectronics. QBER was shown as a promising method to realize a compact THz source that is capable of producing radiation above 1 THz. Although 2D materials are known to have many unique physical properties, generating THz signal using QBER on 2D materials was not fully explored.

The objectives of this dissertation are as follows:

1. To develop an analytical band Monte Carlo model for investigating the electron transport properties in graphene and silicene.
2. To develop a numerical model to investigate the effects of QBER in graphene and silicene towards the possibility of generating of THz signal.

### 1.3 Dissertation Overview

Chapter 1 serves to provide introduction to the current development in THz signal generation. It also highlights two types of low dimensional materials i.e. graphene and silicene and a brief review of these materials are given. Introduction to the analytical model used and the QBER concept are also presented in this chapter. This chapter is followed by the dissertation overview and ended with the dissertation objectives.

Chapter 2 begins with a brief literature review on the THz signal application. A detailed literature review on the current development of THz signal generation is presented after that. This followed by a review on the electronic and mechanical properties of graphene and silicene. This chapter end with the explanation on QBER concept, emphasizing on how the confined electrons oscillate to produce THz radiation.

Chapter 3 presents the methodology of the research starting with the analytical band structure of graphene and silicene. This is followed by the electron transport theory for graphene and silicene. The phonon scattering mechanisms of graphene and silicene are discussed in detail. This chapter continues with the explanation of the Monte Carlo method used in modelling the charge transport properties of graphene and silicene. This chapter also explains how the degeneracy effect is incorporated into the standard Monte Carlo framework with the consideration of Pauli exclusion principle. At the end

of this chapter, the implementation QBER into the Monte Carlo model is presented.

Chapter 4 presents the studies of the charge transport properties of graphene and silicene. The applicability of the Monte Carlo is validated by comparing the calculated drift velocity and mobility to those calculated using first-principles method. The steady-state and transient charge transport properties of graphene and silicene is systematically studied and analysed, paying specific attention to the physical properties such as drift velocity, mobility, carrier concentrations, mean-free path and electrons energy. This chapter ends with the comparisons of the charge transport properties between graphene and silicene.

Chapter 5 details the studies of the QBER in graphene and silicene. This chapter discuss the structure of QBER device and continues with the study of THz signal generation using QBER approach in graphene by using square wave and sinusoidal wave excitation. The second part of this chapter is dedicated to exploring the possibilities of generating QBER-based THz signal in silicene.

Chapter 6 concludes the achievement of research objectives and summarises the results obtained. Further improvements and suggestions for the future works are discussed.

## CHAPTER 2

### TERAHERTZ SIGNAL GENERATION AND LOW DIMENSIONAL MATERIALS

#### 2.1 Introduction

Terahertz (THz) radiation is typically sandwiched between the infrared (IR) and microwave region in the electromagnetic (EM) spectrum that is having frequency from 100 GHz to 10 THz as shown in Figure 2.1 (Nagatsuma, Ducournau and Renaud, 2016; Kang et al., 2017). THz radiation remains the least exploited spectral region and historically, the applications are limited to astronomy and analytical chemistry to identify vibrational and thermal-emission lines of simple molecules. This creates a gap in the applications using THz spectra in comparison to other frequency regions. However, over the past decades, due to the advancement of nanotechnology and photonics, the THz radiation applications have expanded but not limited to: bio-security imaging, information and communication technology, illicit material detection, non-destructive test, ultrafast spectroscopy and fault detection in microelectronics industry (Tonouchi, 2007; Rieh, Jeon and Kim, 2011; Lewis, 2014). Since the beginning of 21<sup>st</sup> century, the number of literatures regarding THz have increased tremendously (Lewis, 2014). Current works are focusing on expanding the usage of THz sources and its detection, increasing the efficiency of the current technology and searching for a new THz radiation source.

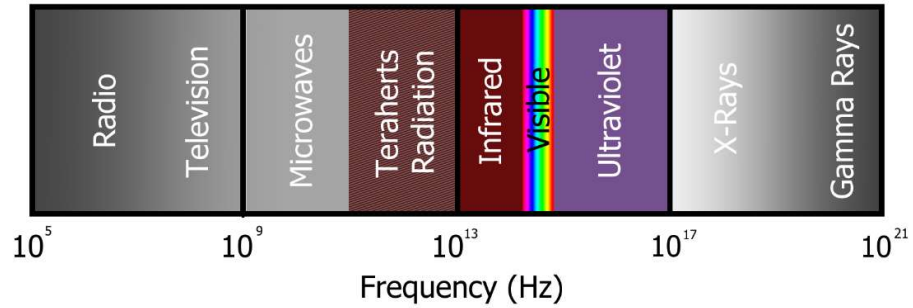


**Figure 2.1: THz region in electromagnetic spectrum loosely defined as frequency in the range of 100 GHz to 10 THz.**

## 2.2 Review of THz Signal Generation

THz radiation attracts a lot of attentions due to some of its unique qualities. For instance, it can move large data rapidly and provides a very high-resolution images without surface ionization. This means, unlike UV radiation, it does not trigger harmful chemical reaction when human tissues are exposed to THz radiation (Armstrong, 2012). Another example is THz radiation can stimulate inter-molecular vibration in organic molecules. These features found its applications in medical imaging, for example, skin cancer diagnosis and classifying drugs and medicines (Tonouchi, 2007). THz radiation also can penetrate a variety of non-conducting materials such as plastics, fabrics, papers, woods and ceramics (Rahman et al., 2016). It cannot penetrate metals and is strongly attenuated by water. Interaction with these materials will give certain unique properties in the form of phase and intensity variation. If these properties can be quantified, it allows for differentiation of materials using THz sensing. THz technology also allows for a tremendous speed of data transfer in comparison to the current mass product utilizing 5 GHz frequency with

maximum data rate of 3.46 Gbps with 802.11ac standard (Intel Corporation, 2017). Wireless transfer of real time video with data rate up to 50 Gbps using THz technology has been reported by Ma et al. (2017).

Several methods have been developed in the past years to generate a controlled THz signal. THz signal can be generated using two methods, i.e. electronic and photonic methods. Photonic method typically uses a laser source to convert the optical energy to THz radiation while electronic method is aimed to multiply the frequency of millimetre wave oscillator to sub-millimetre radiation (Nagatsuma, Ducournau and Renaud, 2016). Currently, photonic method shows a promising path in generating a usable THz signal (Rieh, Jeon and Kim, 2011). Another popular approach in photonic method is quantum cascade laser (QCL) which was first demonstrated by Köhler et al. (2002). The typical structure of QCL is shown in Figure 2.2. The QCL uses a femtosecond laser with continuous wave pulses to produce a THz radiation. Their work was able to deliver coherent average power more than 2 mW with consistent frequency from 4.0 THz to 4.4 THz at temperature of 8 K (Köhler et al., 2002). The THz QCLs now are able to produce peak output power of 6 mW at 186 K and has risen its operating temperature up to 199.5 K without having interference from the applied magnetic field (Fatholouloumi et al., 2012). The main challenge now is to develop QCL that is capable of operating at room temperature with higher output power. Despite this challenge, the QCL concept has allowed for a strong and compact source to be available in the inaccessible regions of electromagnetic spectrum. QCL also is the only high output power

devices above 1 mW and at the same time operating above 1 THz that may find its application in fundamental and applied science (Dhillon et al., 2017).

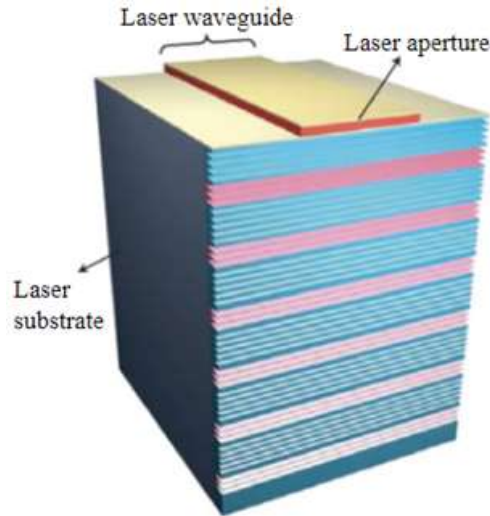


**Figure 2.2: Typical device structure for a quantum cascade laser (Hangyo, 2015).**

Current laser-based sources can generate a single-cycle pulses at 1 THz which maximum field is 1 MV/cm. This has been done by optical rectification on  $\text{LiNbO}_3$  using tilted pulse front pumping method (Hebling et al., 2002) or using organic crystals with a very high nonlinear optical susceptibility constant like DAST (Jazbinsek, Mutter and Gunter, 2008; Hauri et al., 2011). The tilted pulse front pumping can be used with many pump wavelengths. The powerful laser sources were used at their fundamental wavelength to control the rectification process. The spectral output for a single cycle THz pulse is below 3 THz with conversion efficiency more than 2 % based on the organic material absorption (Hauri et al., 2011). The schematic setup of this work is shown in Figure 2.3. Tunable, phase stable multicycle pulses with peak electric fields of

108 MV/cm and frequency ranging from 10 THz to 72 THz has been demonstrated to be effectively obtained by difference frequency mixing in materials like GaSe (Sell, Leitenstorfer and Huber, 2008). Recently, free electron laser (FEL) source passing through magnetic field distorter as shown in Figure 2.4 has been demonstrated as a THz source which is able to produce up to 2 THz signal (Liu, 2018).

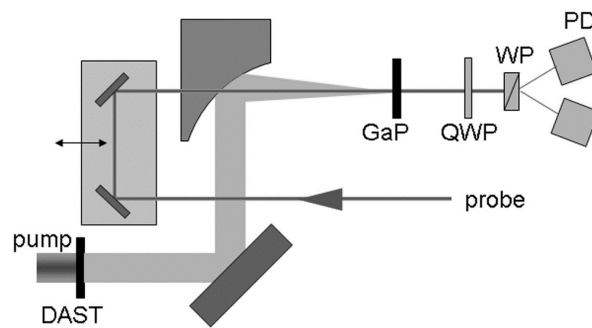


**Figure 2.3: Schematic setup of THz generation using optical rectification in an organic material DAST and its detection is using a GaP sensor, quarter wave plate (QWP), Wollaston prism (WP) and a photodiode detector (PD) (Hauri et al., 2011).**

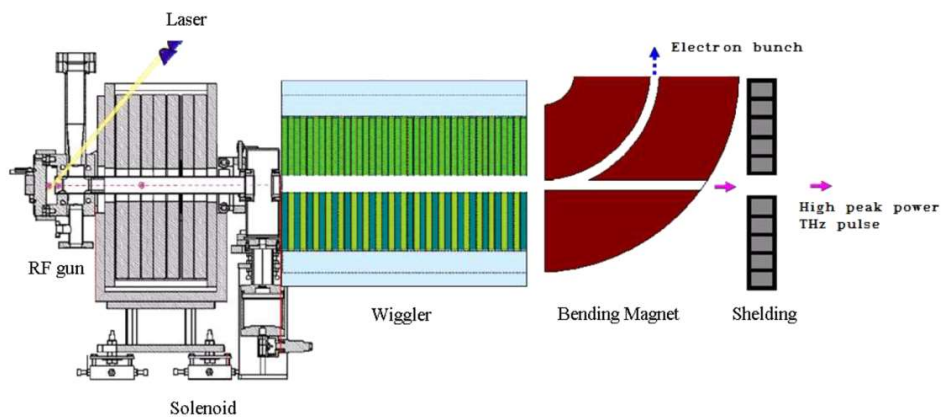


**Figure 2.4: Schematic diagram of THz-FEL with wiggler and electron bunch source (Liu, 2018). The wiggler is a magnetic field distorter in the electron path.**

Vacuum electronics devices (VEDs) also have been used to generate THz radiation (Booske, 2008). These devices have been widely used as THz source and found its way in various applications such as scientific researches, space explorations, radars and military purposes thanks to its long development history, although not many of them are commercially developed (Booske et al., 2011). VEDs use electrical energy to power an accelerated electron beam passing through electromagnetic waveguide known as interaction circuit and convert it into electromagnetic energy. Conceptual illustration of this operation is shown in Figure 2.5. Currently, VEDs are only operable in the range of 0.1 THz to 1.0 THz with operating power up to 1 MW (Dhillon et al., 2017). The efficiency of VEDs are also high in comparison to other THz sources. In order to cover the THz region, the circuit dimension of VEDs must be smaller than the free space wavelength or in sub-millimetre size (Booske, 2008). Yet, the main challenge in developing a compact size VED to operate above 1 THz is that it must be able to tolerate the high intensity beam and radiation power in the 1 mW regime.

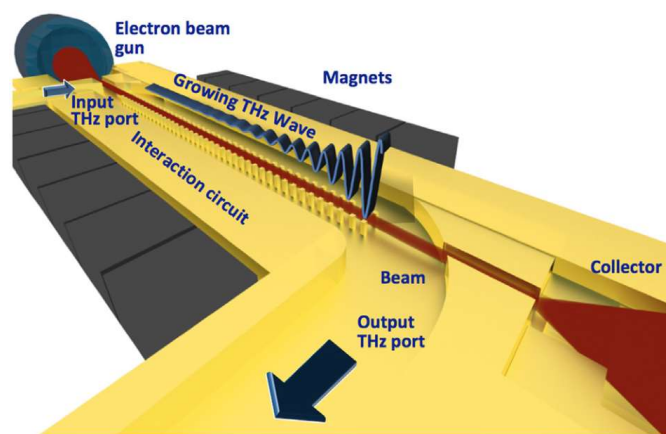


**Figure 2.5: Conceptual design of a vacuum electron amplifier that includes the electron beam source, interaction circuit, confinement magnet and radiation port (Barker, 2005).**

The most common sources for accelerator-based THz radiation devices are synchrotron infrared beamlines that accessible on the synchrotron storage rings facility (Muller, 2010). The first free electron laser (FEL) operated in IR and produced radiation with wavelength of 3.4  $\mu\text{m}$  (Deacon et al., 1977). Another accelerator type is energy recovery linac (ERL) which was firstly demonstrated by Carr et al. (2002), producing radiation up to 1 THz. This source provided a radiation in a similar frequency range to the synchrotron storage with average output power in the range of 10 W and maximum power peak in the kW range. Operational frequency using accelerator base sources was reported tunable from 0.1 THz up to  $10^3$  THz at various output power (Muller, 2010).

The generation of THz signal using various photonic methods have been reviewed in the previous discussions. However, all these methods require bulky experimental setup. For example, although the lasing device of QCL is merely in sub-millimetre size, the cooling system required to cool it to near to zero Kelvin made the setup bulky (Hangyo, 2015; Dhillon et al., 2017). On the other hand, generating THz signal using electronic approach enables the realization of compact and portable THz sources. The advantage of electronic method is that the size of signal generator is usually significantly smaller. One of the promising product of the electronic approach is resonant tunnelling diode (RTD) where it utilized fast electron transport in semiconductor layer (Asada, Suzuki and Kishimoto, 2008; Asada and Suzuki, 2011). The electron in RTD was confined within a quantum well built between two heterobarriers. When the resonant level in the quantum well was near to conduction band edge of the emitter, peak current will occur as shown in Figure 2.6 (Asada and Suzuki,

2011). Increasing the voltage resulted in negative differential conductance which can be utilized by the carrier oscillator. The reported fundamental frequency up to 0.65 THz was obtained at room temperature (Asada, Suzuki and Kishimoto, 2008). Attempt to increase the produced frequency of the THz signal using RTD is still an ongoing research.

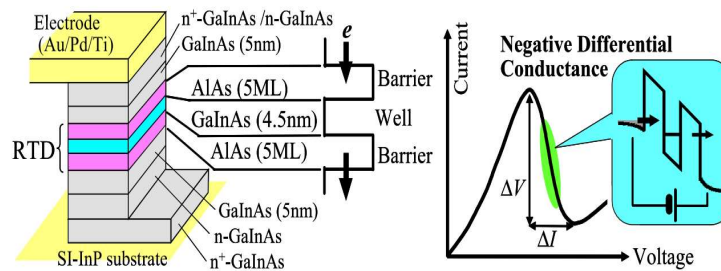


**Figure 2.6: A typical layer structure of resonant tunnelling diode and its current-voltage profile (Asada and Suzuki, 2011).**

A uni-travelling carrier photodiode (UTC-PD) was reported to produce stable radiation signal below 1 THz (Song et al., 2009; Ducournau et al., 2014). The design of UTC-PD was first proposed by Pearsall et al. (1981) with the purpose to reduce dark current in diode. The design utilized the electron velocity overshoot in its operation where a thick electron travelling layer was introduced (Pearsall et al., 1981; Ishibashi et al., 2014). UTC-PD typically comprised a p-doped absorption region where incident photons were absorbed and generated free carriers of electrons and holes. The following absorption layer was a lightly doped transparent layer known as the collector. Due to photons absorption happened in a p-doped layer, holes became the majority carriers and only electrons were the active carriers. These photo-generated electrons will diffuse through the p-doped region and reached the depleted collector region. When a

reverse bias voltage was applied to the collector region, electrons will accelerate further and collected in an n-doped region. This will create a reverse current that was proportional to the incident optical power. The UTC-PD typically can achieve a higher electron speed as it operated at the velocity overshoot regime in the collector region (Ito et al., 2005; Ishibashi et al., 2014). The simplified band diagram of a typical UTC-PD is illustrated in Figure 2.7.

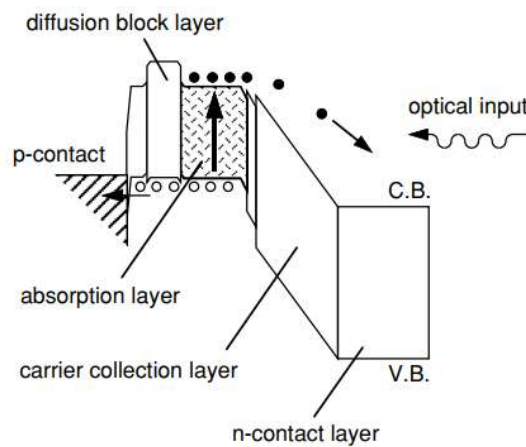


**Figure 2.7: UTC-PD band diagram (Ito et al., 2005).**

Currently, electronic based THz sources are still behind in covering the high region of THz spectrum especially above 1 THz. Studies done by Ong and Hartnagel (2007; 2008; 2015) showed that ballistic reflection can be utilized to generate THz radiation. The generation of THz signal using this method will be discussed in detail in section 2.4. In recent years, a combination of photonic and electronic approach was reported like spintronic emitter that utilizing spin properties. A spintronic emitter uses spin properties to pass a polarized current through a ferromagnetic material was demonstrated by Seifert et al. (2017). In this work, the device current was passed through a ferromagnetic

**Table 2.1: Some of the reported THz systems and its operating frequency using several technologies. P, E and C letter after the device is to indicate either the method that the device used falls into photonic, electronic or combination (hybrid) method. Respectively, QCL and UTC-PD denotes quantum cascade laser and uni-travelling carrier photodiode.**

<b>Device</b>	<b>Freq. (THZ)</b>	<b>Year</b>	<b>Ref.</b>
GaAs/AlGaAs QCL (P)	4.40	2001	(Köhler et al., 2002)
Energy-recovered inac (P)	1.00	2002	(Carr et al., 2002)
InAlAs/InGaAs/InAlAs heterojunction (E)	3.5	2007	(Ong and Hartnagel, 2007)
Resonant tunnelling diode (E)	0.65	2008	(Asada, Suzuki and Kishimoto, 2008)
UTC-PD (E)	0.25	2009	(Song et al., 2009)
GaAs/AlGaAs QCL (P)	3.22	2012	(Fatholouloumi et al., 2012)
UTC-PD (E)	0.40	2014	(Ducournau et al., 2014)
AlSb/InAs/AlSb heterojunction (E)	2.00	2015	(Ong and Hartnagel, 2015)
InAs/AlAsSb QCL (P)	4.00	2016	(Brandstetter et al., 2016)
Spintronics emitter (C)	10.0	2017	(Seifert et al., 2017)
Free electron laser (P)	2.00	2017	(Liu, 2018)

material W/CoFeB/Pt tri-layer with 6 nm thickness on a glass substrate. This material was excited by an 800 nm laser pulse on a specially design W and Pt layers which had an opposite spin Hall angles, created a sub-picosecond current under excitation. The spintronic emitter was reported to be able to produce radiation frequency up to 2 THz. This work shows that it is possible to create a THz current other than the electronic and photonic approaches.

In summary, several of THz sources developed in the area of the photonic and electronic up to the recent years together with its radiated frequency are presented in Table 2.1.

### **2.3 Low Dimensional Materials**

Until the discovery of graphene in 2004, a single atom thick monolayer material was just a mathematical concept that was impossible to be manufactured (Novoselov et al., 2004). However today, the research on monolayer material has attracting lot of attentions. The reduced dimensionality of the space results in electrons exhibit many unusual quantum mechanical effects such as tunnelling, quantum Hall effect, spin valley effect and superconductivity which was never been observed before if the material was in bulk form. Carbon is on the front line in the discovery of low dimensional carbon allotropes (Kroto et al., 1985; Iijima, 1991; Novoselov et al., 2004). The 2D form of carbon nanostructure which is known as graphene had been predicted by Philip Wallace (1947) more than 60 years ago but only successfully demonstrated in 21<sup>st</sup> century. The success of graphene has motivated many

researchers to search for other 2D materials such as silicene (Vogt et al., 2012), bismuthene (Reis et al., 2017), monolayer MoS<sub>2</sub> (Mak et al., 2010), germanene (Bampoulis et al., 2014), monolayer GeSe (Zhao et al., 2018), phosphorene (Koenig et al., 2014), arsenene (Kamal and Ezawa, 2015) and antimonene (Ares et al., 2017).

### **2.3.1 Graphene**

Graphene is a single 2D sheet of carbon atoms, bonded together in a hexagonal honeycomb lattice as shown in Figure 2.8. It is the lightest material known at 0.77 mg/m<sup>2</sup>, the strongest compound discovered i.e. between 100-300 times stronger than steel and with a tensile stiffness of 42 N/m (Lee et al., 2008), the best heat conductor at room temperature at  $1.69 \times 10^3$  to  $1.81 \times 10^3$  W/mK and also the best conductor of electricity with the Fermi velocity is 1/300 of the speed of light and mobility up to  $2 \times 10^6$  cm/s (Borysenko et al., 2010; Hirai et al., 2014). Over the years, many electronic applications based on graphene have been reported. A graphene-based FET was demonstrated as a mixer circuit operational at 185 GHz -215 GHz (Andersson, Zhang and Stake, 2016) and graphene based rectennas was reported to rectify 28 THz frequency (Zhu et al., 2013). These show that graphene-based devices are working in the THz spectrum. Furthermore, THz signal detection using graphene was successfully reported in recent years (Zak et al., 2014; Suzuki, Oda and Kawano, 2016; Yang et al., 2017).

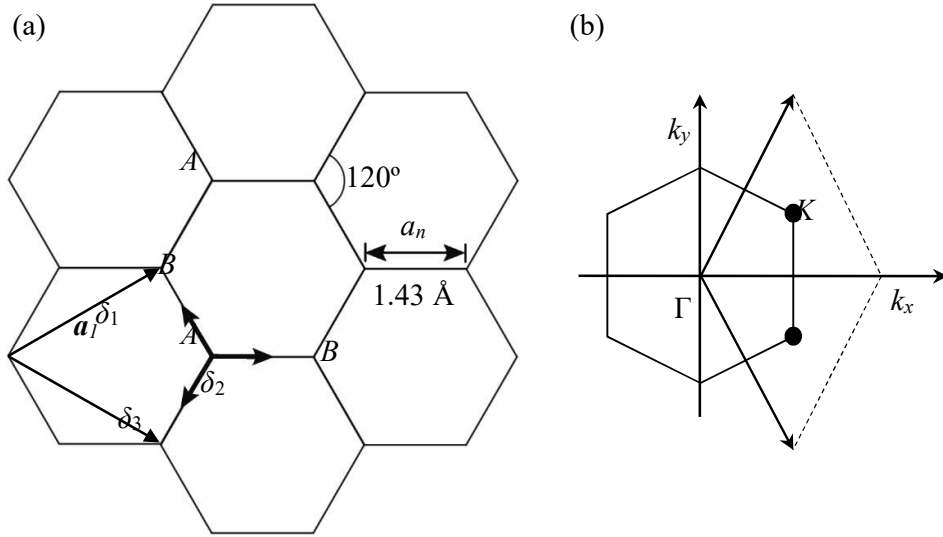


**Figure 2.8: (a) Honeycomb lattice arrangement found in graphene.  $A$  and  $B$  is the lattice point,  $a_i$  is the lattice vector and  $\delta_i$  is the sub-lattice vector. (b) The  $K$  and  $K'$  point in the hexagonal Brillouin zone where the Dirac points are located. The bond length  $a_n$  of C-C atoms is 1.43 Å (Harrison, 2012).**

Graphene was first experimentally demonstrated by Novoselov et. al. (2004) through mechanical exfoliation of graphite using Scotch tape and today, large area graphene is successfully synthesized by using CVD methods (Xu et al., 2017). For carbon, hexagonal lattice is the most possible lattice arrangement for carbon to appear in a 2D form as shown in Figure 2.8.

Consider a free form and purely flat hexagonal graphene sheet. For a single atom's carbon C, its electronic structure is  $[\text{He}] (2s)^2 (2p)^2$ . Additionally, for silicon, its electronic structure is  $[\text{Ne}] (3s)^2 (3p)^2$ . The inert 1s electron maintains its form in the solid-state form. Interestingly, 2s and 2p may change its form for  $sp^3$  hybridization. For carbon, having these orbitals naturally will

create a tetrahedral bond pattern which use up all the valence electrons thus forming a diamond lattice structure. When all of the valence electrons are being used, there is no free electron for conduction. This creates a large band gap in diamond at around 5 eV. Another form of  $sp^3$  hybridization is in the form of methane,  $CH_4$ . Instead of  $sp^3$  hybridization,  $sp^2$  hybridization can also occur. With  $sp^2$  orbitals formed,  $2p_z$  is left in the atom as  $(2s)^2$  orbital is hybridized with the  $2p_x$  and  $2p_y$  orbitals. In this condition, the lattice is in hexagonal shape as shown in Figure 2.8 and Figure 2.9 (a). The  $sp^2$  will form a bond with the adjacent carbon and  $2p_z$  will form an out-of-plane  $\pi$  bond from the lattice structure. The leftover  $p_z$  orbitals also create a linear band dispersion that is closing at  $K$  point (Fuhrer, Chun and MacDonald, 2010).

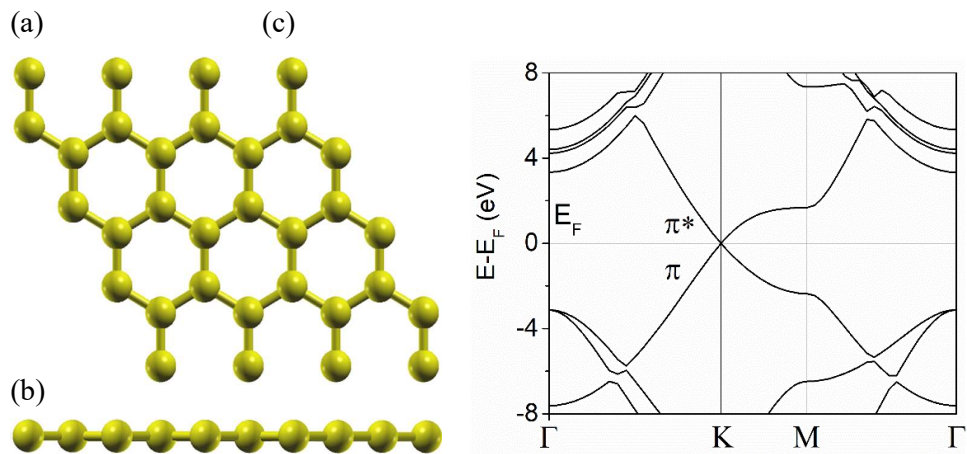


**Figure 2.9: (a) Top view and (b) side view of the monolayer graphene atomic structure. (c) Electronic band structures of monolayer graphene along the high symmetry direction in the Brillouin zone.**

Graphene's dispersion shows a remarkable feature near the  $K$  point of the Brillouin zone. The energy-momentum shows a linear dispersion and the

point where the conduction band touches the valence band is known as Dirac point, as shown in Figure 2.9 (c) (Das Sarma et al., 2011; Castro Neto et al., 2009). Therefore, pristine graphene sheet essentially is a zero-bandgap semiconductor with a linear dispersion around the  $K$  point instead of a parabolic one which is commonly observed in bulk semiconductors. Another interesting property is near the Dirac point where the effective mass of graphene is zero. This means that the electrons can travel as if they were photons albeit with a speed about of 1/300 smaller than the speed of light (Drut and Lähde, 2013). This becomes one of the main motivations of the researchers to explore graphene and utilize the material to develop high speed electronic devices.

The electron mobility of a suspended monolayer graphene was predicted to be around  $2 \times 10^5$  cm<sup>2</sup>/Vs that is two orders higher than bulk silicon (Novoselov et al., 2004; Chen et al., 2008; Borysenko et al., 2010; Hirai et al., 2014). As mention, graphene in its pristine form is gapless. Consequently, monolayer graphene cannot be used effectively in FET devices due to high leakage current at OFF-state. Nevertheless, by exploiting the high electron speed in graphene, graphene has a potential to generate THz radiation by using QBER concept (Abidin et al., 2017).

### **2.3.2 Silicene**

Silicene can be described as the silicon equivalent of graphene (Jose and Datta, 2014) with its hexagonal lattice arrangement shown in Figure 2.8. Silicene sheet can be formed by condensing vaporized silicon on a silver

substrate (Vogt et al., 2012). The term silicene itself was first used by Guzman-Verri et al. (Guzman-Verri and Lew Yan Voon, 2007). Despite having a similar hexagonal lattice structure and possess the same number of valence electrons, silicene has distinct mechanical and electronic properties from its counterpart, graphene.

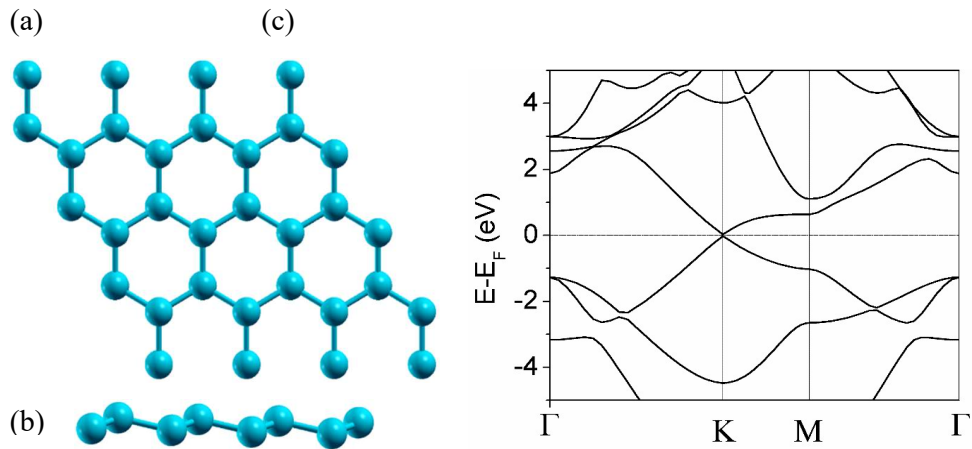


**Figure 2.10: (a) Top view and (b) side view of the monolayer silicene atomic structure. (c) Electronic band structures of monolayer silicene along the high symmetry direction in the Brillouin zone.**

Unlike graphene, silicene prefers a buckled structure (Jose and Datta, 2012) as shown in Figure 2.10 (b). Theoretical studies found the buckling value was around  $0.44 \text{ \AA}$  (Lew Yan Voon et al., 2010; Qin et al., 2012; Roman and Cranford, 2014). This was caused by the larger Si-Si bond length in silicene (Lew Yan Voon et al., 2010) which weaken the  $\pi$ - $\pi$  interaction and resulted in a distinct coupling of  $\sigma$  and  $\pi$  bonds. Tensile stiffness of silicene was reported to be around  $6.6 \text{ N/m}$  (Zhao, 2012; Qin et al., 2012; Roman and Cranford, 2014; Mortazavi et al., 2016). Meanwhile, low-buckled pristine silicene is gapless

with Dirac cones and linear dispersion as shown in Figure 2.10 (c), similar to those observed in graphene (Jose and Datta, 2014). Thus, the charge carriers in the 2D system are expected to behave like massless Dirac-Fermions. However, the linear dispersion is only extended up to 0.4 eV from the  $K$  point presumably results from the weakening of  $\pi$ - $\pi$  coupling.

The mobility of pristine silicene was reported to be around  $1200 \text{ cm}^2/\text{Vs}$  (Li et al., 2013; Abidin et al., 2017). In contrast to graphene, tuning the silicene bandgap should be easier because of the broken inversion symmetry between sub-lattices (Lay, 2015). With the changing in the degree of buckling, Liu et al. reported that spin-orbital coupling will induce a band gap opening of 1.55 meV at the Dirac point (Liu, Feng and Yao, 2011). Also, a study had shown that the scattering rate in silicene is much higher than graphene (Li et al., 2013). Silicon is more likely to take  $sp^3$  hybridization. This makes silicene cannot exist naturally as graphite, a multiple stack of graphene bounded by the weak Van der Waals bonding. Thus, mechanical exfoliation method that is commonly used to produce graphene from graphite cannot be used to isolate silicene from bulk silicon.

Silicene grown on Ag(111) substrate was experimentally demonstrated using CVD method under ultra-high-vacuum condition (Vogt et al., 2012; Fleurence et al., 2012; Feng et al., 2012). Other forms of silicene such as nanoribbons (Aufray et al., 2010), oxygen-capped sheets (Nakano et al., 2016) and free-standing Si multilayers (Kim et al., 2011) also had been reported. In terms of practical application, theoretical studies have shown that silicene can

be used as a material for spin property devices (Ahmed, Ashama and Phillips, 2018; Xu, 2018; Ezawa, 2013). Silicene has a strong spin orbit interaction that creates a strong spin-valley dependence and spin Hall effect. Opening of the band gap from electric field interaction will lead to topological phase transition in silicene. Furthermore, gate voltage can be used to control the conductance where spin and valley polarized current can be generated (Ezawa, 2013; Ahmed, Ashama and Phillips, 2018). Despite that, experimental works on silicene based devices were not widely reported because silicene is not stable in open air (Quhe, Wang and Lü, 2015).

Tao et al. (2015) demonstrated the first silicene device in the form of field effect transistor (FET). The silicene was grown on top of Ag(111) thin film that rested on a mica. Then, the silicene was capped with alumina to protect it from oxidation when exposed to ambient. The alumina/silicene/Ag stack was detached and deposited onto SiO<sub>2</sub> substrate where the alumina layer was attached to the SiO<sub>2</sub> substrate. Subsequently, the Ag layer was selectively removed through etching, thus forming a source and drain's contact for back-gate FET. The whole process is illustrated in Figure 2.11. The silicene FET yielded an ON/OFF ratio of 10 and with a measured mobility of ~100 cm<sup>2</sup>/Vs (Tao et al., 2015). The mobility was about one order lower than free-standing silicene as mentioned in the previous discussions. The mobility degradation is attributed to the synergistic effects of the charge impurity in the substrate, surface optical phonon scattering, and renormalization of the Fermi velocity induced by the alumina substrate (Yeoh et al., 2016; Chen, Zhong and Weinert, 2016).

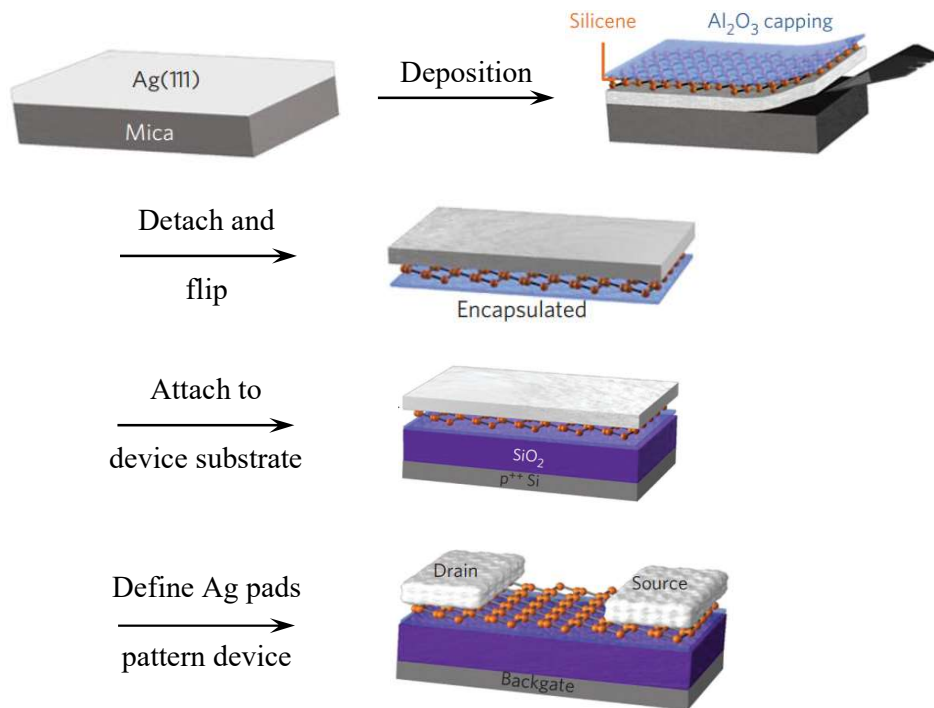


**Figure 2.11: Fabrication process of a back-gate silicene FET. Illustration adapted from Tao et al. (2015).**

To date, unlike graphene, the research works especially on the charge transport properties of silicene were not widely reported. Currently, the possibilities of the silicene as an active material for THz signal generation and detection were not being explored although silicene shares many similarities with graphene. Table 2.2 summarizes the comparison between the mechanical and electronics properties between graphene and silicene.

**Table 2.2: Comparison between mechanical and electronic properties of graphene and silicene at 300 K.**

Mateal	Graphene	Silicene
Tensile stiffness (N/m)	42 <sup>a</sup>	6.6 <sup>b,a</sup>
Thermal conductivity (W/mK)	1.69×10 <sup>3</sup> - 1.81×10 <sup>3</sup> <sup>c</sup>	9.4 <sup>d</sup>
Buckling (nm)	0	0.44 <sup>e</sup>
Thickness	3.4 <sup>a</sup>	4.0 <sup>f</sup>
Bond length (Å)	1.43 <sup>g</sup>	2.25 <sup>e</sup>
Fermi velocity (cm/s)	1.0×10 <sup>8</sup> <sup>h</sup>	5.8×10 <sup>7</sup> <sup>i</sup>
Electron mobility (cm <sup>2</sup> /Vs)	1.0×10 <sup>6</sup> <sup>h</sup>	1.2×10 <sup>3</sup> <sup>i</sup>
Dielectric constant	2.35 <sup>j</sup>	34.33 <sup>k</sup>

Data taken from <sup>a</sup> Lee et al. (2008), <sup>b</sup> Mortazavi et al. (2016), <sup>c</sup> Xu et al. (2014), <sup>d</sup> Xie, Hu and Bao (2014), <sup>e</sup> Lew Yan Voon et al. (2010), <sup>f</sup> Tao et al. (2015), <sup>g</sup> Harrison (2012), <sup>h</sup> Borysenko et al. (2010), <sup>i</sup> Li et al. (2013), <sup>j</sup> Hwang et al. (2012) and <sup>k</sup> Mohan, Kumar and Ahluwalia (2014).

<sup>a</sup> Value is an average from armchair and zigzag silicene.

## 2.4 Quasi Ballistic Electron Reflection (QBER)

Ballistic electron transport happens when the electron escapes the imperfection and avoiding the electron-phonon scattering and electron-electron scattering. This effect leads to drift velocity overshoot when the electrons moved from stationary (Hess, 1981). With a suitable field distribution, devices can obtain a high speed during its operation. The theoretical concept of THz signal generation using QBER was first proposed in a double-barrier heterostructure of InAlAs/InGaAs/InAlAs by Ong and Hartnagel (2007).

The mechanism of QBER requires electrons in the 2D material to be confined in a potential well. An AC bias is applied across the potential well and the electrons will drift according to the applied electric field direction. In the first cycle of the AC bias, once the drifted electron hit the potential barrier during its flight, a reflection will occur and bouncing the electron away from the potential barrier. After the reflection happened, the electrons will drift in the direction opposing the electric field direction. Eventually, the electron speed will drop as it moves in the opposite direction to the electric field until it reduced to zero. The electrons will reach a turning point where the direction of motion is reversed and drifting again in the external electric field direction. These accelerated and decelerated of the electron's motion back and forth from the potential barrier creates a radiated signal in THz frequency. The motion will die off due to kinetic energy losses during the scattering process. This process will be repeated at the next cycle of AC bias.

Figure 2.12(a) shows an electron starts at low energy point **A** is having its wave vector at  $+\mathbf{k}_1$ . Once it reaches the boundary at point **B**, the electron has a new energy state and wave vector  $+\mathbf{k}_2$ . When the reflection occurs, the wave vector changes its direction to  $-\mathbf{k}_2$  and has the same energy as before reflection at point **C**. After that, as the particle moves in the opposite direction, it will lose the kinetic energy and back to point **A** and the whole processes repeat. The cycle from point **A** to **C** will become smaller over the time because the total energy is lost from the scattering processes when the particle drifting from point **A** to **B** and **C** to **A**.

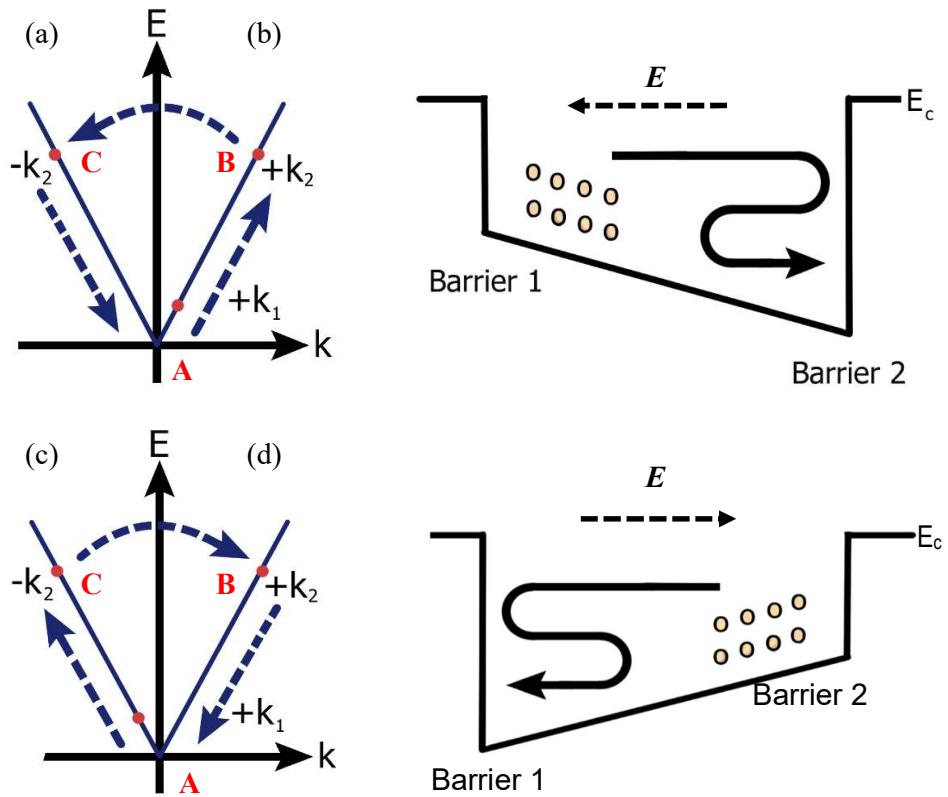


Figure 2.12: Schematic illustrations of QBER mechanism for the carrier in a simplified (a) E-k diagram and (b) potential well for the first half of the AC bias. For the second half of the AC cycle, the E-k diagram and potential well is illustrated in (c) and (d) respectively.

## CHAPTER 3

### CHARGE TRANSPORT THEORY AND MONTE CARLO METHOD

#### 3.1 Introduction

An accurate description of electronic band structure is important to properly model the electronic transport properties of a material. When an electron moves in a crystal lattice, it will encounter scattering which can be derived from the first order time-dependent perturbation theory. The analytical band structure and scattering mechanisms of two different low dimensional materials i.e. graphene and silicene are incorporated into the Monte Carlo model in order to study the electron transport properties and the possibility of THz signal generation through quasi-ballistic electron swing. The procedure to develop a Monte Carlo model for the study of electron transport properties in graphene and silicene will be discussed in this chapter. Additionally, using this Monte Carlo framework, the methodology of generating THz signal based on quasi-ballistic electron reflection concept are also outlined.

#### 3.2 Analytical band Structure

Full band structure can be calculated using several approaches such as local empirical pseudopotential method (Cohen and Chelikowsky, 1989), **k.p**

method (Kane, 1956) and non-local pseudopotential method (Zunger and Cohen, 1978). Inclusion of a full band structure in the Monte Carlo simulations requires high computational resources although it can give results with high accuracy compared to the experimental measurements. This approach is known as full-band Monte Carlo method and it is widely used for investigating charge properties under the influence of high electric field. However, for the case of low energy transport, electrons tend to populate at the band minimum and Monte Carlo simulation can be carried out using the analytical band method. For conventional bulk semiconductors, the analytical band can be modelled as parabolic spherical valleys corrected by a non-parabolic factor (Cardona and Pollak, 1966).

The charge transport properties of graphene and silicene can be adequately modelled using the analytical band approach since state of the art nanoscale devices usually operate at low energy and therefore the electron transport tends to occur in the Dirac cone region. For pristine free-standing graphene and silicene, energy dispersion relation at  $K$  point at the hexagonal lattice can be approximated by:

$$E = \hbar v_f |\mathbf{k}| \quad (3.1)$$

where  $\hbar$  is the reduced Planck constant,  $v_f$  is the Fermi velocity and  $|\mathbf{k}|$  is the magnitude of the wave vector relative to the  $K$  point in  $\mathbf{k}$ -space. The linear dispersion limit used in Monte Carlo simulation for graphene and silicene was reported to be 1 eV and 0.4 eV, respectively (Yeoh et al., 2016; Rengel, Couso

and Martin, 2013). The  $v_f$  for graphene and silicene are  $10^8$  cm/s and  $5.8 \times 10^7$  cm/s, respectively.

Analytical band Monte Carlo (AMC) modelling in 2D material was first carried out by Shishir and Ferry (2009), but Chauhan and Guo (2009) published simultaneously a very relevant paper with a similar Monte Carlo model to investigate the electron drift velocity saturation in graphene. Similar Monte Carlo modelling. Modelling of graphene with analytical band Monte Carlo model was also carried out to investigate various factors such as electron-electron interactions, impurity, diffusivity and field strength (Fang et al., 2011; Bresciani et al., 2010; Rengel and Martín, 2013; Sule et al., 2014; Borowik, Thobel and Adamowicz, 2017). Hirai et al. (2014), Rengela, Pascual and Martín (2014), and Li et al. (2010) studied the effects of underlying substrate on graphene. Modelling of graphene devices such as diodes and FET by incorporating analytical band in the Monte Carlo framework had been reported (Harada, Ohfuti and Awano, 2008; Harada et al., 2011; David, Register and Banerjee, 2012). Full band Monte Carlo modelling of silicene was done by Gaddemane et al. (2018). The analytical charge scattering equations for silicene are formulated by Li et al. (2013) through first-principles calculation. By incorporating these equations into the AMC model, Yeoh et al. (2016) performed analysis on the effects of  $\text{Al}_2\text{O}_3$  substrate on the charge transport properties of silicene. Later Abidin et al. (2017) investigated the effects of carrier concentrations on the transport properties of silicene at low energy by using the analytical band structure as described by equation (3.1). AMC method was also successfully used by Borowik, Thobel and Adamowicz (2016) to

calculate the electron diffusion coefficient in silicene. Similar approach was also used to investigate the effect of flexural phonon of the silicene on its transport (Rengel et al., 2018).

### **3.3 Scattering Mechanism**

The changes of lattice spacing under external perturbation such as temperature, pressure or electric field can cause change of the crystal potential. This in turn will affect the carrier transport properties. The vibrational energy due to the lattice vibration is quantized and termed as phonon. If the atoms in the lattice vibrate in a coherent manner deviating from their equilibrium positions the phonons are known as acoustic phonon. On the other hand, if the oscillation does not move the centre of mass of the crystal cell, the phonons arise are termed as optical phonon. For both optical and acoustic phonon, in longitudinal mode, the vibration is in the direction of wave propagation (LA, LO) while in transverse mode the vibration happens perpendicular to the wave propagation (TA, TO). However, in 2D material, there is another phonon mode which is known as flexural mode where the vibration is out-of-plane. Similarly, the out-of-plane phonon can be either due to acoustic (ZA) or optical phonon (ZO). However, in graphene, studies have shown that ZA and ZO values are very low compared to other modes which can be ignored (Castro Neto et al., 2009; Borysenko et al., 2010; David, Register and Banerjee, 2012). To simplify this for graphene simulation, the LA and TA modes are combined into a single acoustic phonon (AP) mode. Similarly, the LO and TO modes are combined into a single optical phonon (OP) mode. This approach has been successfully

used and validated (Shishir and Ferry, 2009; David, Register and Banerjee, 2012; Hirai et al., 2014). The AP and OP scattering mechanisms are treated as isotropic processes. While the OP phonon is an inelastic process, the AP scattering can be either elastic or inelastic process (Borysenko et al., 2010). The analytical solution of elastic scattering rate (David, Register and Banerjee, 2012) is given by:

$$S_{ac}^{elas} = \frac{E_D^2 k_b T}{4\hbar^3 v_f^2 v_s^2 \rho_s} E \quad (3.2)$$

where  $E_D$ ,  $\rho_s$ ,  $v_s$  and  $v_f$  is the deformation potential, graphene mass density, sound velocity and Fermi velocity, respectively. Inelastic OP and AP scattering rates can be expressed in the following form:

$$S_{op(ac)}^{inel} = \frac{D_f^2}{\hbar^2 \rho_s \omega_{op(ac)} v_f^2} [(E + \hbar\omega_{op(ac)})N + (E - \hbar\omega_{op(ac)})(N + 1) \times \Theta(E - \hbar\omega_{op(ac)})] \quad (3.3)$$

where  $\Theta(x)$  is the Heaviside function that ensures the energy is sufficient to emit a phonon,  $D_f$  is the deformation potential,  $\hbar\omega$  is the phonon energy and  $N$  is the Bose-Einstein distribution for phonon.

Scattering mechanisms of silicene share many similarities with graphene since both are derived from Group IV element with a hexagonal lattice. However, in contrast to graphene, ZO and ZA scattering in silicene cannot be excluded in the Monte Carlo simulation. The out-of-plane scattering rate in

silicene is at least two orders larger than graphene due to the buckled geometry which originate from the weak  $\pi$  bonding (Li et al., 2013). The analytical expression for intravalley scattering rate by TA, LA or ZA mode is given by:

$$S_{ac}^{elas} = \frac{E_D^2 k_B T}{\hbar^3 v_f^2 v_s^2 \rho_s} E \quad (3.4)$$

where  $E_D$ ,  $\rho_s$ ,  $v_s$  and  $v_f$  is the deformation potential, silicene mass density, sound velocity and Fermi velocity, respectively. This acoustic intravalley scattering rate is treated as an elastic process. On the other hand, the intravalley AP scattering rate (LA, TA and ZA) and both intervalley and intravalley OP scatterings rates (ZO, TO and LO) are inelastic processes. The analytical expression for these types of scattering mechanism can be calculated using equation (3.5) (Li et al., 2013):

$$S_{op(ac)}^{inel} = \frac{D_f^2}{2\hbar^2 \omega_{op(ac)} \rho_s v_f^2} [(E - \hbar\omega_{op(ac)})(N+1) \\ \times \Theta(E - \hbar\omega_{op(ac)}) + (E + \hbar\omega_{op(ac)})N] \quad (3.5)$$

where  $\Theta(x)$  is Heaviside function that ensures the energy is sufficient to emit a phonon.  $D_f$ , and  $\hbar\omega_o$  is the deformation potential and optical phonon energy, respectively.

### 3.4 Monte Carlo Method

Monte Carlo method is a type of computational algorithms that depends on statistical sampling through random number to solve problems that might be deterministic. Monte Carlo simulation was first carried out by Enrico Fermi to investigate neutron diffusion. Over the years, with the rapid development of computational resources, the Monte Carlo method is going popular fast. Beginning of 1960s, Kurowasa (1966) started to develop Monte Carlo code to investigate the charge transport properties in bulk semiconductor. Recently, research using Monte Carlo method has been extended to model the electronic transport properties in 2D materials.

Ensemble Monte Carlo method is widely used to study the electron transport in semiconductor material with good accuracy. In the Ensemble Monte Carlo method, a group of super particles as a representative of carriers are injected into the semiconductor material. These super particles will drift under the influence of electric field for a finite free-flight time that is determined from a randomly drawn number between 0 and 1. At the end of the free-flight time these particles will encounter a scattering process. The type of scattering process that occur is chosen from a pre-computed look-up table which consists of the scattering process probability with the aid of a random number. The scattering probability has energy as its function. A virtual self-scattering mechanism is also being considered as one of the scattering process. If self-scattering is chosen, the particle continues the free flight. After the scattering event the energy and momentum of the particle may change depending on the scattering

mechanism. The whole process is repeated for each super particle. Statistical sampling is carried out at each pre-determined time interval to calculate the carrier charge transport properties. The whole process is summarized in Figure 3.1.

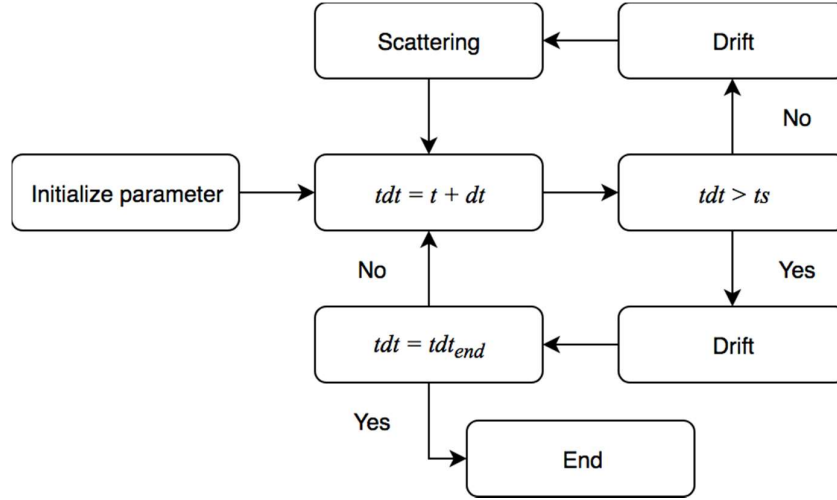


**Figure 3.1 : Flow chart of analytical band Monte Carlo simulation.**

The probability per unit time  $P(\tau)$  of a carrier during the free-flight  $\tau$  is given by:

$$P(\tau) = \Gamma \exp(-\Gamma \tau) \quad (3.6)$$

where  $\Gamma$  is largest value of the summation of all possible scattering rate. The summation of all possible scattering rates is a function of energy which can be expressed as:

$$W_T(\varepsilon_k) = \sum_{j=1}^N W_j(\varepsilon_k) \quad j=1,2,3,4,5...N \quad (3.7)$$

where  $j$  denotes each type of scattering up to  $N$  possible scattering mechanisms.

Therefore,  $\tau$  can be computed as

$$\tau = -\frac{\ln(r_1)}{\Gamma} \quad (3.8)$$

where  $r_1$  is a random number from 0 to 1. If an electric field is applied to the semiconductor material, the carrier drifts for a finite time,  $\tau$  (also known as free-flight time) before the motion is terminated by a scattering event. At the end of the free-flight, the wave vector of the carrier need to be updated. The change of wave vector  $\Delta k$  can be calculated as

$$\Delta k = -\frac{qE}{\hbar} \tau \quad (3.9)$$

where  $E$  is the electric field,  $\hbar$  is the reduced Planck constant and  $q$  is the elementary charge. The  $\tau$  can be calculated from equation (3.8). Additionally, at this stage, the carrier may encounter different scattering mechanisms. The type of scattering mechanism that the carrier encountered can be determined based on cumulative summation of different scattering rates normalized by  $\Gamma$ .

$$\Lambda_n(\varepsilon_k) = \frac{\sum_{j=1}^n W_j(\varepsilon_k)}{\Gamma} \quad j = 1, 2, 3, 4, 5 \dots N \quad (3.10)$$

where  $j$  denotes each type of scattering up to  $N$  possible scattering mechanisms. A second random number  $r_2$  between 0 to 1 is drawn and the  $n$ -th scattering mechanism is selected if the condition in equation (3.10) is met.

$$\Lambda_{n-1}(\varepsilon_k) < r_2 \leq \Lambda_n(\varepsilon_k) \quad (3.11)$$

Subsequently, the carrier energy need to be updated depending on whether the scattering is an elastic or an inelastic process. For silicene and graphene simulations all the scatterings are treated as isotropic process where the probability of the carrier being scattered in any of the direction is the same. In contrast to bulk material, the simulation in present work is confined to 2D  $\mathbf{k}$ -space since graphene and silicene are 2D material. Hence, by using random number  $r_3$  the azimuthal angle,  $\phi$  of the wave vector can be computed as shown in equation (3.12)

$$\phi = 2\pi r_3 \quad (3.12)$$

Based on equation (3.12) and (3.1), the wave vector component in the direction of  $x$  and  $y$  can be calculated as:

$$k_x = k \cos \phi, \quad k_y = k \sin \phi \quad (3.13)$$

### 3.5 Degeneracy Effect

Ensemble Monte Carlo is a semiclassical technique that simulates the motion of electrons in a material according to a classical mechanics which in reality, electrons are fermions. Hence, they must obey the Pauli exclusion principle where for each quantum number that is available, at most only two electrons can occupy it which must differ in their spin numbers. The Pauli exclusion principle can be thought as many body interactions that limits the phase space available for electronic transitions. Typically, for a bulk semiconductor, Pauli exclusion principle need to be considered if the carrier concentration is above  $10^{17} \text{ cm}^{-3}$ . However, for graphene, previous work has shown the Pauli exclusion principle needs to be incorporated in the Monte Carlo frame work even for carrier concentration from  $10^{11} \text{ cm}^{-2}$  to  $10^{13} \text{ cm}^{-2}$  (Shishir and Ferry, 2009). These values are close to the graphene intrinsic carrier concentration as reported experimentally (David, Register and Banerjee, 2012).

Usually the Pauli exclusion principle is included into the Monte Carlo code by adding a sub-routine which is commonly known as the rejection routine. The essence of the rejection routine is to determine whether the selected final state after a scattering process can be occupied by the carrier using the Pauli exclusion principle. In the present model, the degeneracy effect due to Pauli exclusion principle is adopted from the work by Lugli and Ferry (1985). The method uses discretization of reciprocal of  $k$ -space function to define the maximum number of super-particles that can occupy the  $k$ -space grid. A brief explanation on this rejection routine are discussed in following paragraph.

In  $\mathbf{k}$ -space, the density of the wave vector for a particular spin is given as:

$$n_k = \frac{A}{(2\pi)^2} \quad (3.14)$$

where  $A$  is the area of the 2D material. A two-dimensional grid in  $\mathbf{k}$  space is set up where the area of the elementary cell can be computed as:

$$\Omega_c = \Delta k_x \Delta k_y \quad (3.15)$$

Each elementary cell can accommodate at maximum  $N_c$  carrier which is given by:

$$N_c = \frac{2\Omega_c A}{(2\pi)^2} \quad (3.16)$$

where the factor 2 is due to the carrier spin and additionally for graphene and silicene, the factor is 4 because of spin and valley pseudo spin. A distribution function,  $f_c$  is established in each cell by first counting the number of carriers in the cell and then normalized it by dividing  $N_c$ . After a scattering process has occurred and the chosen final state is located in a particular cell,  $f_c$  in that particular cell is compared with a randomly drawn number,  $r$  between 0 and 1. The selected final state can be occupied by the carrier if  $r > f_c$ . On the other hand, if  $r < f_c$  the carrier is being rejected from occupying the selected state and no scattering will occur. This rejection routine has been widely used in ensemble

Monte Carlo simulation in bulk material (Gelmont, Kim and Shur, 1993; Siddiqua and O’Leary, 2018) as well as 2D material (Hirai et al., 2014; Rengel, Couso and Martin, 2013; Borowik, Thobel and Adamowicz, 2016). The rejection routine to capture the degeneracy effect is summarized in the flow chart in Figure 3.2.

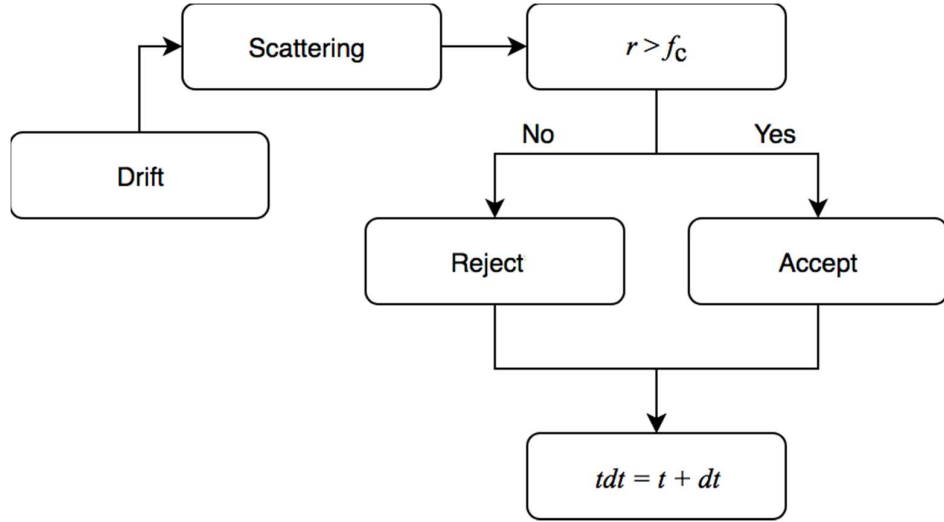


**Figure 3.2 : Rejection routine in the ensemble Monte Carlo model.**

### 3.6 Monte Carlo Model for QBER Device

The possibility of generating THz signal based on QBER concept by using low dimensional material (i.e. graphene or silicene) is investigated in this work. The general frame work of Monte Carlo model was described in section 3.4 can be used to model the QBER phenomenon. Space charge density distribution calculation using *cloud-in-cell* method is used (Tomizawa, 1993). The space charge density distribution information is needed for potential

calculation using the Poisson equation implemented in finite difference scheme. The following paragraphs explain the Monte Carlo model for QBER devices.

The QBER model is constructed with a device length  $L$  where it is divided by a number mesh column,  $N$ . An equal number of super-particles will be assigned on each space cell of length  $\Delta x$ . Each of the cell is assigned with a uniform electron density value where this value is divided by each super-particle in each mesh. Therefore, the calculation of electron density in the device model is done by counting the number of particles in each space cell. Each cell is identified by a grid point ( $i$ ) and calculating the cell electron density is done by calculating the number of particles surrounding the grid point in the space cell using equation (3.17)

$$n(i) = N(i) \times N_{pp} / \Delta x \quad (3.17)$$

where  $n(i)$  is carrier density for cell ( $i$ ),  $N(i)$  is the number of particle inside the cell ( $i$ ),  $N_{pp}$  is the number of electron per super-particles and  $\Delta x$  is the cell length. The charge associated to the particle is treated as a cloud of charge with same size of cell ( $i$ ). By calculating the displacement of the particles from point ( $i$ ), portion of the charge cloud that is not in the cell belong to the adjacent cell ( $i + 1$ ) or ( $i - 1$ ) where the excess charge cloud is located. Therefore, cell ( $i$ ) is not having the full value of electron density carried by the particle but a portion of charge cloud that only located inside its cell.

When an electron moves across the device to another cell, the instantaneous electron density on the cell changes and modifies the local electric field. Therefore, instead having a constant electric field like in bulk material simulation, the electric field in equation (3.9) must be calculated first. The change in local electric field can be calculated using Poisson equation in equation (3.18).

$$\nabla^2 V = -\rho / \varepsilon \quad (3.18)$$

where  $\varepsilon$  is the permittivity of the material and  $\rho$  is charge density. For one dimensional device model, the Poisson equation will be in one dimensional form

$$\frac{\partial^2 V}{\partial x^2} = -\rho / \varepsilon \quad (3.19)$$

which can be discretized to

$$\frac{V_{i-1} - 2V_i + V_{i+1}}{\Delta x^2} = -\rho_i / \varepsilon \quad (3.20)$$

where  $V_i$  is the potential value in the cell  $i$ ,  $\rho_i$  is the charge density inside the cell taken from carrier density value from equation (3.17), and  $\Delta x$  is the cell length. In this Monte Carlo model, bias is applied on one side of the barrier while the opposite barrier is grounded. The simulation process for QBER device is summarized Figure 3.3.

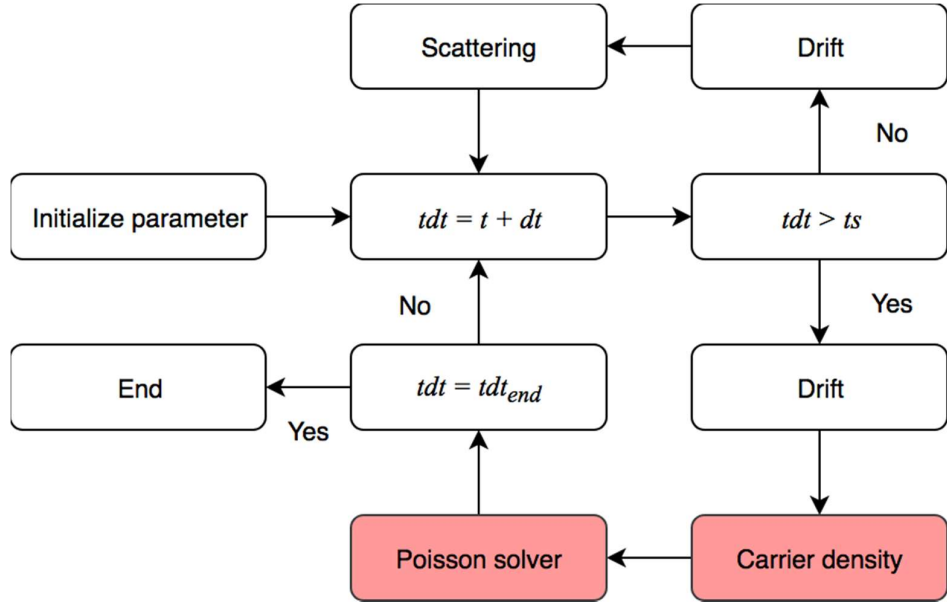


**Figure 3.3: Analytical band Monte Carlo simulation flow for QBER device.**

The particle drift velocity  $v_x$  is defined by equation (3.21) and can be translated into current density by using Shockley-Ramo theorem (Shockley, 1938; Ramo, 1939)

$$v_x = v_f \frac{k_x}{|\mathbf{k}|} \quad (3.21)$$

$$J = \frac{qv_x}{L} N_{pp} \quad (3.22)$$

where  $q$  is elementary charge,  $L$  is the device length and  $N_{pp}$  is the number of electron per super-particles. Spectral analysis is done on the recorded current waveform evaluated by using Fourier transform on the oscillation intensity in a

single bias pulse. A period of AC bias will have two level of bias pulses.

Radiation is estimated from the current oscillation by

$$E_{rad} \propto \frac{dJ(t)}{dt} \quad (3.23)$$

Fourier transform is carried out on the radiation intensity obtained from the autocorrelation function (Ong and Hartnagel, 2007) in equation (3.24).

$$I(\tau) \propto \int_{-\infty}^{+\infty} E_{rad}(t)E_{rad}(t-\tau)dt \quad (3.24)$$

## CHAPTER 4

### MODELLING OF CHARGE TRANSPORT IN TWO-DIMENSIONAL MATERIALS

#### 4.1 Introduction

Modelling of charge transport using full band Monte Carlo (FMC) method allowed us to obtain computational results with a good accuracy based on first-principles calculation of the band structure and scattering mechanisms. However, the FMC method requires high computational resources. Another approach is to use analytical band Monte Carlo (AMC) method where the band structure and scattering mechanisms are incorporated into the Monte Carlo framework in the form of analytical equations. This method has been widely used to study the charge transport properties in bulk semiconductors in the past few decades using parabolic band structure at the band minima (Gelmont, Kim and Shur, 1993; Kukita and Kamakura, 2013; Siddiqua and O’Leary, 2018). Recently, the AMC method has been employed to investigate the charge transport properties in 2D materials such as graphene (Borowik, Thobel and Adamowicz, 2016; 2017) and silicene (Yeoh et al., 2016; Borowik, Thobel and Adamowicz, 2016) with good accuracy. In this chapter, charge transport properties of graphene and silicene are studied by using AMC method where a linear band structure is used. The simulations here are confined at low energy

region because at high energy region, the linearity of the band structure for graphene and silicene is not preserved.

## 4.2 The Applicability of Analytical Monte Carlo

The unique properties of graphene have motivated many researchers to search for other potential 2D materials. Silicon shared the same elementary group with carbon in periodic table and recently, monolayer silicon (silicene) has attracted a lot of attention especially with the experimental demonstration of silicene based field effect transistor (FET) (Tao et al., 2015). The crystal lattice of silicene is hexagonal but in contrast to graphene, it is buckled and not perfectly flat. Similar to graphene, silicene also possess Dirac cone at the  $K$  point of the hexagonal Brillouin zone which could result in relativistic massless electron (Lew Yan Voon et al., 2015). Silicene shares several similarities with graphene in terms of the charge transport properties.

The scattering parameters used in this work for graphene and silicene are taken from Hirai et al. (2014) and Yeoh et al. (2016), respectively. To re-validate these fitting parameters, the drift velocity for graphene and silicene are calculated and the results are presented in Figure 4.1. For graphene, the result fits well with the first-principles calculation by Li et.al. (2010; 2011). Similarly, for silicene, the drift velocity curve is in good agreement with the published data from Li et al. (2013). The drift velocities are simulated by AMC model up to 20 kV/cm for graphene and 40 kV/cm for silicene. The electron highest energy at the respective electric field is found less than 1 eV for graphene and 0.6 eV for

silicene. Within these energy windows, the linearity of the Dirac cone is preserved as shown in Figure 4.2. The material and scattering parameters for graphene and silicene are tabulated in Table 4.1.

**Table 4.1: Graphene and silicene simulation parameters used in this work. These parameters are taken from Hirai et al. (2014)<sup>1</sup> and Yeoh et al (2016)<sup>2</sup>.**

<b>Graphene Parameter<sup>1</sup></b>	<b>Value</b>		
Intervalley acoustic phonon energy (eV)	0.124		
Intervalley acoustic phonon deformation potential (eV/cm)	$3.5 \times 10^8$		
Acoustic phonon deformation potential (eV)	4.5		
Optical phonon deformation potential (eV/cm)	$1 \times 10^9$		
Optical phonon energy (eV)	0.164		
Fermi velocity (cm/s)	$1 \times 10^8$		
<b>Silicene Parameter<sup>2</sup></b>	<b>Out-of-Plane</b>	<b>Transverse</b>	<b>Lateral</b>
Intravalley acoustic phonon energy (eV)	2.4	17	3.2
Intervalley acoustic phonon deformation potential (eV/cm)	$6.1 \times 10^7$	$14 \times 10^7$	$4.2 \times 10^7$
Acoustic phonon deformation potential (meV)	13.2	23.7	13.2
Optical phonon deformation potential (eV/cm)	$6.3 \times 10^7$	$70 \times 10^7$	$65 \times 10^7$
Optical phonon energy (meV)	50.6	50.6	61.7
Fermi velocity (cm/s)	$5.8 \times 10^7$		

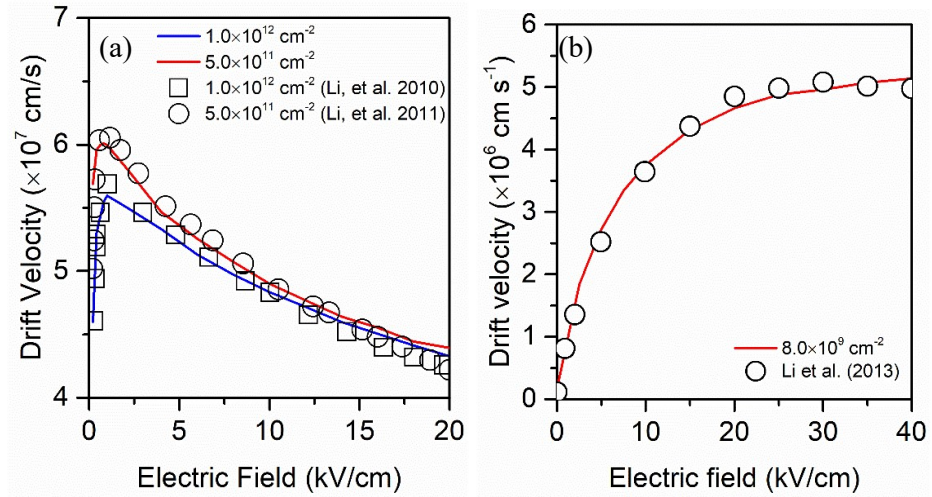


**Figure 4.1: (a) Drift velocity against applied electric field for suspended monolayer graphene in comparison to the works done by Li et al. (2010; 2011). (b) The scattering parameters used to calculate the silicene drift velocity are taken from Yeoh et al. (2016). The results are exactly the same as those published by Yeoh et al. since the same Monte Carlo code was used to calculate the drift velocity in this work.**

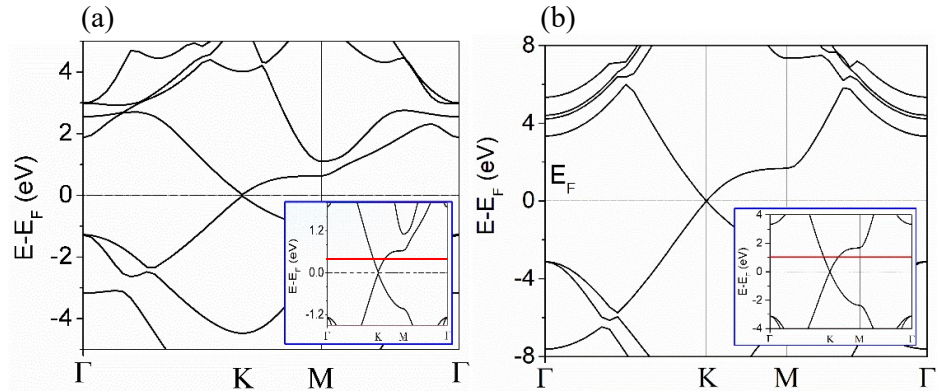


**Figure 4.2: Energy band diagram for monolayer (a) graphene and (b) silicene. The inset in (a) and (b) shows expanded view of the Dirac cone. As shown by the red line, linearity of the band structure is maintained at 1eV for graphene and 0.6 eV for silicene.**

### 4.3 Electron Transport in Graphene

As expected from the work done by Li et al. (2010; 2011), the carrier concentration shows an influence to the electron drift velocity in graphene as shown in Figure 4.3. Here, the carrier concentration is the representative of intrinsic carrier density that is present in graphene. The simulation was done with different carrier densities from  $1 \times 10^{11} \text{ cm}^{-2}$  to  $1 \times 10^{13} \text{ cm}^{-2}$ . The drift velocity increases with lower carrier concentrations across all the tested electric fields and more apparent when the electric field is less than 5 kV/cm. For example, at 1 kV/cm, the drift velocity drops from  $6.5 \times 10^7 \text{ cm/s}$  to  $2.3 \times 10^7 \text{ cm/s}$  when carrier concentration increases from  $1 \times 10^{11} \text{ cm}^{-2}$  to  $1 \times 10^{13} \text{ cm}^{-2}$ . When the carrier concentration increases, the electron energy is heavily influenced by the degeneracy effects due to Pauli exclusion principle leading the electrons to occupy the higher energy states away from the Dirac point. This effect is shown in Figure 4.4 where the electron energy drops as the carrier concentration decreases. On the other hand, the electron-phonon scattering rate increases at higher energy level as evident from the results in Figure 4.5. Therefore, it is expected that the electron drift velocity reduces with higher carrier concentrations consistent with the results in Figure 4.3. Additionally, Figure 4.3 also shows a higher drift velocity near zero electric field with a lower carrier concentration. For example, the drift velocity reaches  $6.6 \times 10^7 \text{ cm/s}$  at  $1 \times 10^{11} \text{ cm}^{-2}$  and  $2.2 \times 10^7 \text{ cm/s}$  at  $1 \times 10^{13} \text{ cm}^{-2}$ . This corresponds to 0.1 eV and 0.25 eV of the electron energy for carrier concentrations of  $1 \times 10^{11} \text{ cm}^{-2}$  and  $1 \times 10^{13} \text{ cm}^{-2}$ , respectively. It is worth mentioning that at 0.1 eV, the emission mode of

optical phonon and intervalley acoustic phonon scatterings are absent. Therefore, the electron can reach a very high drift velocity at this condition.

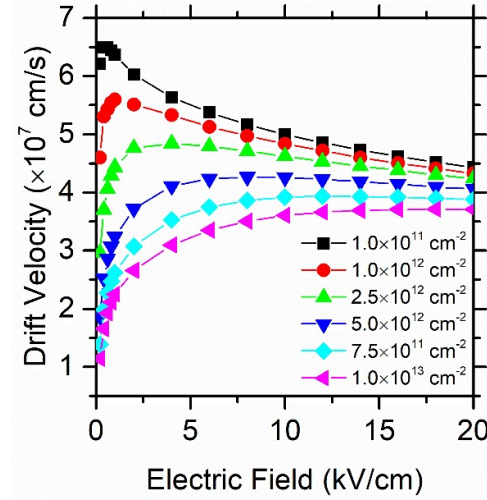


**Figure 4.3: Drift velocity against applied electric field with carrier concentration ranging from  $10^{11}$  cm $^{-2}$  to  $10^{13}$  cm $^{-2}$ .**

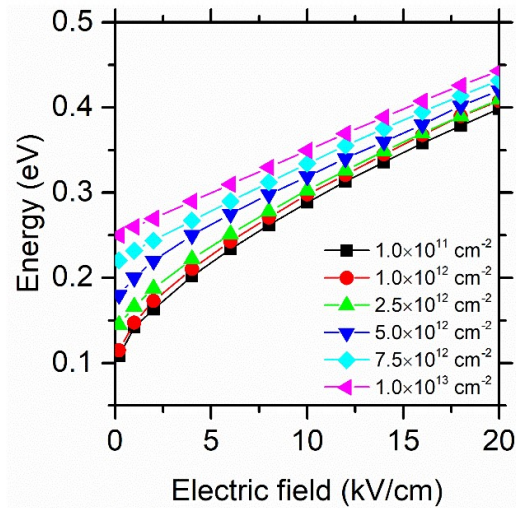


**Figure 4.4: Average energy against applied electric field with carrier concentration ranging from  $10^{11}$  cm $^{-2}$  to  $10^{13}$  cm $^{-2}$ .**

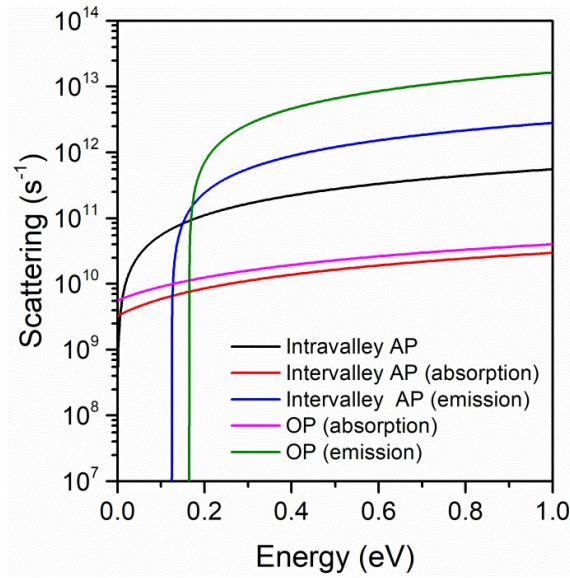


**Figure 4.5: Electron scattering rate for graphene at room temperature for acoustic phonon and optical phonon. AP and OP denotes acoustic phonon optical phonon respectively.**

The electron energy distribution in graphene for different applied electric fields and carrier concentrations are illustrated in Figure 4.6. It is important to take note that for all cases, the electron energy is less than 1 eV where the energy dispersion is still in the linear region of the Dirac cone as shown in Figure 4.2 (a). Overall, the electron energy distribution skews to a higher energy level with the increases of carrier concentration. Such phenomenon is attributed to the degeneracy effect. Additionally, the peak of electron energy distribution varied by the carrier concentration changes by 0.09 eV at 20 kV/cm in comparison to 0.20 eV at 1 kV/cm. These results may also provide an explanation on the convergence of the drift velocities as the electric field increases (see Figure 4.3) at different carrier concentrations.

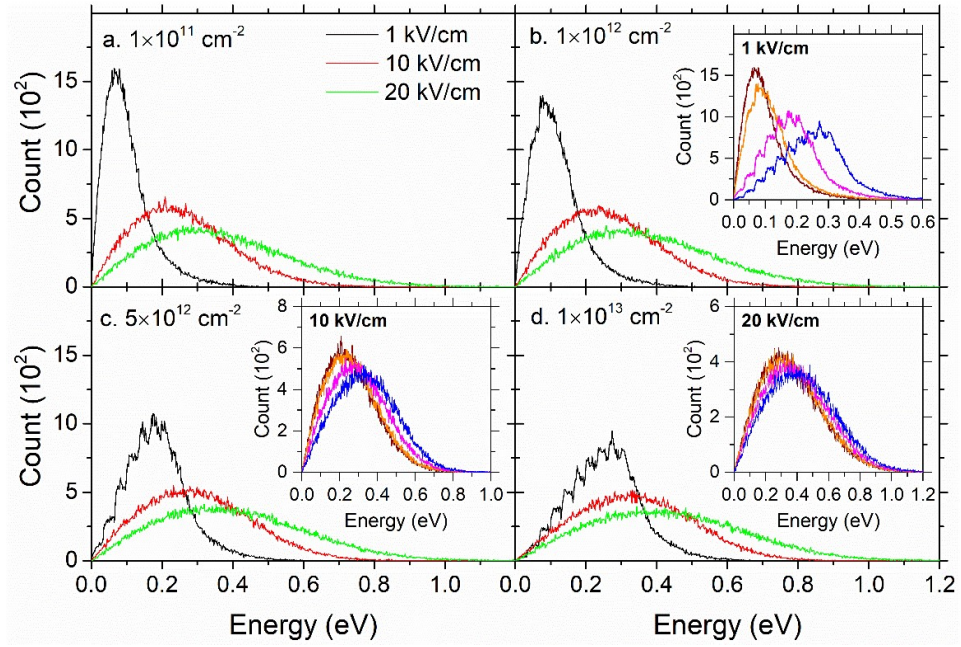


**Figure 4.6: Electron energy distribution for suspended monolayer graphene at applied fields of 1 kV/cm, 10 kV/cm and 20 kV/cm. Subplot in (b), (c) and (d) shows the same plot that overlapping 1 kV/cm, 10 kV/cm and 20 kV/cm with different carrier concentrations. Brown, orange, purple and blue refer respectively to  $1 \times 10^{11} \text{ cm}^{-2}$ ,  $1 \times 10^{12} \text{ cm}^{-2}$ ,  $5 \times 10^{12} \text{ cm}^{-2}$  and  $1 \times 10^{13} \text{ cm}^{-2}$ .**

Figure 4.7 shows the standard deviation of the wave vector,  $k_x$  which increases with the carrier concentration. The standard deviation for  $k_x$  starts to converge as the electric field is augmented. As a result, the drift velocity does not change much with the carrier concentrations at higher electric fields. This is consistent with the previous discussions where the drift velocity for different carrier concentrations starts showing sign of convergence at higher electric fields. Near zero electric field, the range of the standard deviation  $k_x$  from  $1 \times 10^{11} \text{ cm}^{-2}$  to  $1 \times 10^{13} \text{ cm}^{-2}$  is  $0.16 \text{ nm}^{-1}$  and at 20 kV/cm, the range changes to

0.08 nm<sup>-1</sup>. Since the distribution of  $k_x$  also increases with applied electric field and carrier concentration, the probability of electrons occupying higher energy states is higher which in turn increases the probability of phonon scattering.

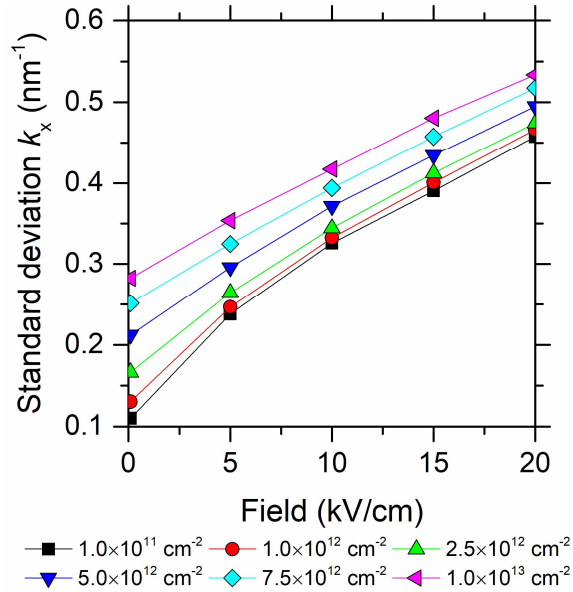


**Figure 4.7: Standard deviation of  $k_x$  as a function of electric field and carrier concentration for suspended monolayer graphene**

In Figure 4.8, the electron mobility for graphene is calculated as a function of carrier density. Theoretically, the intrinsic carrier density of graphene is found to be around  $9 \times 10^{10}$  cm<sup>-2</sup> (Fang et al., 2007) while experimentally it is in the range of  $2 \times 10^{11}$  cm<sup>-2</sup> to  $2.7 \times 10^{12}$  cm<sup>-2</sup> depending on the sample impurity and measurement setup (Zhang et al., 2005; Novoselov et al., 2004; Tan et al., 2007; Bolotin et al., 2008). Through first-principles method, the electron mobility at room temperature of a pristine monolayer graphene was calculated to be  $9.5 \times 10^5$  cm<sup>2</sup>/Vs (Borysenko et al., 2010). In present work, the electron mobility at carrier concentration of  $1 \times 10^{11}$  cm<sup>-2</sup> can reach up to

$9.88 \times 10^5 \text{ cm}^2/\text{Vs}$ , which is about 4 % higher than the previously reported value (Borysenko et al., 2010). Table 4.2 shows the electron mobility of the graphene from this study in comparison with other semiconductor materials.

**Table 4.2: Comparison between electron mobility of the graphene obtained from this study with other semiconductor materials.**

Semiconductor Materials	Electron Mobility ( $\text{cm}^2/\text{Vs}$ )	Ref.
Graphene	$9.88 \times 10^5$	This study
InSb	$7.7 \times 10^4$	(Rode, 1971)
GaN	440	(Crouch, Debnam and Fripp, 1978)
$\text{Al}_x\text{Ga}_{1-x}\text{As}$	$\sim 1.2 \times 10^3$	(Liu, 1990)
InGaAs	$1.2 \times 10^4$	(Somogyi and Pfeifer, 1992)
$\text{Ga}_x\text{In}_{1-x}\text{P}$	$\sim 1.0 \times 10^3$	(Shitara and Eberl, 1994)

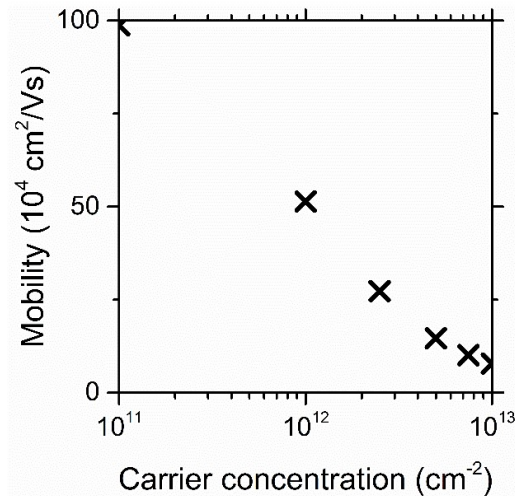


**Figure 4.8: Electron mobility of suspended monolayer graphene as a function of carrier concentration.**

Experimentally, the reported electron mobility for a free-standing graphene is  $2 \times 10^5 \text{ cm}^2/\text{Vs}$  (Bolotin et al., 2008; Chen et al., 2008). However, the measured

mobility may not be applicable to a pristine graphene because in their experiment the graphene is contaminated with residual impurities. Hirai et al. reported mobility  $2 \times 10^6 \text{ cm}^2/\text{Vs}$  from the AMC method. This mobility discrepancy originates from the rejection technique used in the simulation where Hirai et al. employed a simplified form of rejection technique in their calculations (Hirai et al., 2014).

The electron mobility degrades as the carrier concentration increases. For example, when the carrier concentration increases from  $1 \times 10^{11} \text{ cm}^{-2}$  to  $1 \times 10^{13} \text{ cm}^{-2}$ , the electron mobility drops by 96 % to  $7.9 \times 10^4 \text{ cm}^2/\text{Vs}$ . This effect has been explained in the previous discussion on the electron energy and phonon scattering rate relationship. Briefly, as the degeneracy effect becomes more apparent at higher carrier concentrations, the electrons tend to occupy higher energy levels from the Dirac point. Electrons at higher energy levels experience higher phonon scatterings as shown in Figure 4.5. The probability of the momentum randomization increases with scattering, hence slows the electron movement and its mobility.

Figure 4.9(a) shows the simulated drift velocity against distance travelled in a free-standing monolayer graphene. The distance travelled during the transient state increases as the applied electric field becomes weaker. This happens because as the external electric field is increased, electrons are able to gain energy faster from the field, which results in experiencing higher phonon scatterings as their energy increases. This in turn reduced the overshoot drift velocity with distance at a higher field.

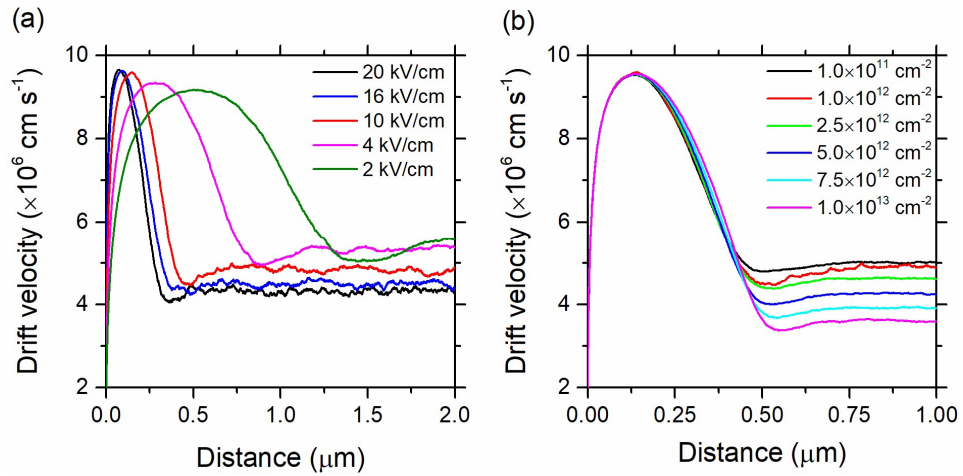


**Figure 4.9: Electron drift velocity against travelled distance in a monolayer graphene. In (a) the carrier concentration is fixed at  $1 \times 10^{12} \text{ cm}^{-2}$  whereas in (b) the applied electric field is fixed at 10 kV/cm.**

Figure 4.9(b) shows the drift velocity against the distance travelled with various carrier concentrations ranging from  $10^{11} \text{ cm}^{-2}$  to  $10^{13} \text{ cm}^{-2}$  at a fixed applied electric field of 10 kV/cm. During the initial stage of the transport, there is no significant change in the drift velocity overshoot profiles for different carrier concentrations. However, the steady-state drift velocity becomes lower as the carrier concentrations in the graphene increases.

To gain a deeper insight into this phenomenon, the electron mean free path of graphene at different carrier concentrations and applied electric fields are calculated as shown in Figure 4.10.

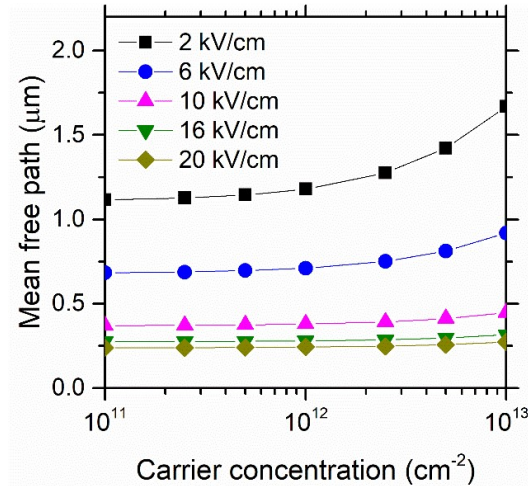


**Figure 4.10: Mean free path of a suspended monolayer graphene**

It is well known that in the Monte Carlo semi-classical transport model electrons gain energy from the electric field with no scattering event within the mean free path region. This region is correlated to the distance of the electron travels during the transient state (Hess, 1981). For a given electric field, the mean free path remains almost constant up to carrier concentration of  $2.5 \times 10^{12} \text{ cm}^{-2}$ . Thereafter, it increases slowly. A closer inspection on Figure 4.10 reveal that the distance travelled by the electron during the transient stage for carrier concentration less than  $2.5 \times 10^{12} \text{ cm}^{-2}$  is almost the same. Recall Figure 4.9 (b) when steady-state is reached, the drift velocity is lower with higher carrier concentrations. At high carrier concentrations, the degeneracy effect becomes critical. As discussed previously, the interplay between the degeneracy effect, phonon scattering rate and electron energy forces the electron to occupy higher energy level, thus the drift velocity degrades because of the higher scattering phonon experienced by the highly energetic electrons. The previously measured mean free path for a suspended monolayer graphene at room temperature is 75 nm (Du et al., 2008), 0.46  $\mu\text{m}$  (Dragoman et al., 2009) and 1.2  $\mu\text{m}$  (Bolotin et

al., 2008). However, not much information is given in their work regarding the carrier concentrations in their graphene sample. Therefore, a direct comparison of their measured mean free path is not possible. However, these values are within the range with those reported in this work.

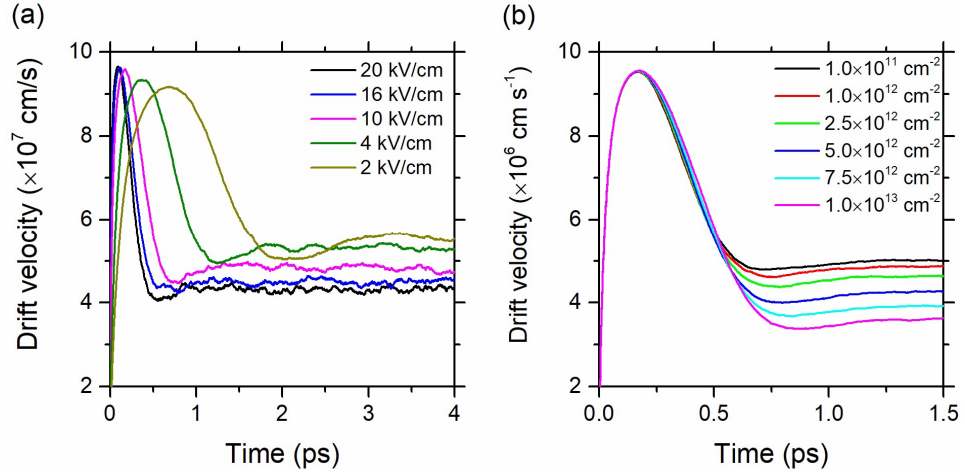


**Figure 4.11: Electron drift velocity against time with a fixed (a) carrier concentration at  $1 \times 10^{12}$  cm $^{-2}$  and (b) applied field at 10 kV/cm in a suspended monolayer graphene.**

The graphene's instantaneous drift velocity at different applied electric fields are shown in Figure 4.11. For all cases, drift velocity overshoot can be observed. At a given carrier concentration, as the electric field decreases the duration of the drift velocity overshoot becomes longer. On the other hand, at a fixed electric field, the drift velocity profile is almost similar at the transient stage and when it reaches steady-state the drift velocity is lower with higher carrier concentrations. The physical explanations on the results obtained in Figure 4.11 are similar to those in Figure 4.9 which have been discussed previously.

#### 4.4 Electron Transport in Silicene

It has been reported that experimental grown silicene, has intrinsic carrier concentrations around  $8 \times 10^9 \text{ cm}^{-2}$  (Tao et al., 2015). Similar to graphene, carrier concentrations have a profound impact on the electron drift velocity in silicene (Abidin et al., 2017; Shishir and Ferry, 2009) as illustrated in Figure 4.12. The simulation in Figure 4.12 was done for different carrier densities ranging from  $10^{11} \text{ cm}^{-2}$  to  $10^{13} \text{ cm}^{-2}$ . Overall, when the carrier concentration is increased, the drift velocity saturation tends to occur at a higher electric field.

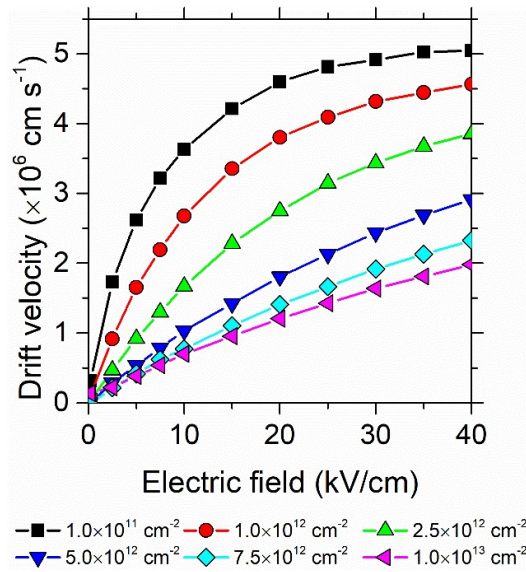


**Figure 4.12: Drift velocity against applied electric field with carrier concentration ranging from  $10^{11} \text{ cm}^{-2}$  to  $10^{13} \text{ cm}^{-2}$ .**

For graphene, it is well known that the rest mass is zero due to the linear dispersion near the Dirac point. However, the cyclotron mass is not zero. It was further demonstrated that the cyclotron mass increases with the carrier density and electron energy (Novoselov et al., 2005). Silicene shared many similarities

with graphene. As expected, the electron drift velocity in silicene increases as the carrier concentration drops since the reduction of carrier concentration implies the cyclotron mass of the silicene is smaller. Similar to graphene, the electron energy scales with the carrier concentrations as shown in Figure 4.13. For example, at 20 kV/cm, the carrier energy increases from 0.08 eV at  $1 \times 10^{11} \text{ cm}^{-2}$  to 0.16 eV at  $1 \times 10^{13} \text{ cm}^{-2}$  which corresponds to the increment of 92 %.

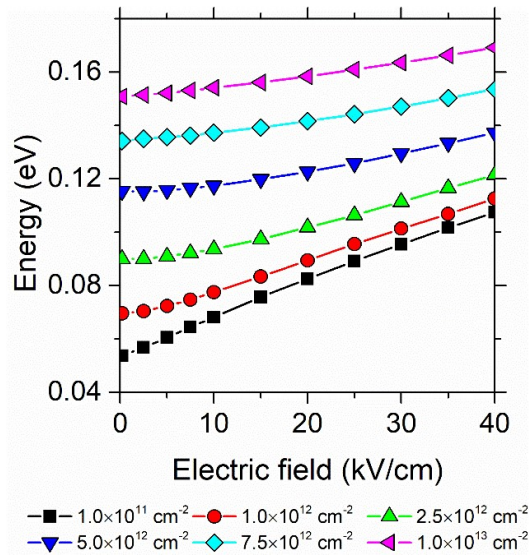


**Figure 4.13: Average energy attained by the electrons as a function electric field with carrier concentration ranging from  $10^{11} \text{ cm}^{-2}$  to  $10^{13} \text{ cm}^{-2}$ .**

When the carrier concentration is higher, the degeneracy effects becomes more apparent. Due to Pauli exclusion principle, electrons at a higher concentration move further away from the Dirac cone to higher energy states. This could also offer elucidation on the higher electron energy when the carrier concentration increases. On the other hand, with higher energy, the scattering rate increases as illustrated in Figure 4.14. This in turn degrades the electron drift velocity.

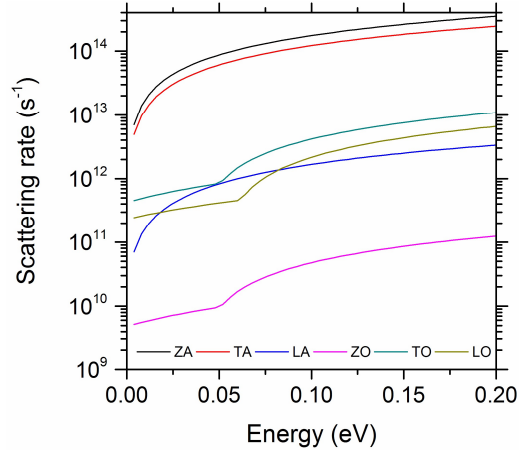


**Figure 4.14: Electron scattering rates in silicene at room temperature for different phonon modes. ZA, TA, LA, ZO, TO and LO denote out-of-plane acoustic, transverse acoustic, longitudinal acoustic, out-of-plane optical, transverse optical and longitudinal optical respectively.**

Figure 4.15 shows the electron energy distribution at different carrier densities. At high field and low carrier concentration, the electron energy distribution is wider. Surprisingly, as the carrier concentrations go higher, the applied electric field has minimal impact on the electron energy distribution. In this condition, the mean energy is less dependent on the applied electric field. Indeed, the energy also increases alongside the applied electric field but this dependency is less apparent when the carrier concentrations are high. This observation is consistent with the results in Figure 4.13. At low carrier concentrations, due to the degeneracy effects, there are more states available for the electrons to occupy after a scattering event. With the increase of electric field, the phonon scattering will become more pronounced. From a physical point of view, a high scattering rate will lead to a higher probability of the electron wavenumber in the direction of the applied field,  $k_x$  being randomized

at a given applied electric field. This could allow for a justification on the wide electron energy distribution in the case of silicene with low carrier concentrations and high electric field. On the other hand, further increase of the carrier concentration could lead to less empty states available at low energy. Therefore, the electron energy distribution is skewed to the higher energy as illustrated in Figure 4.15 (d).

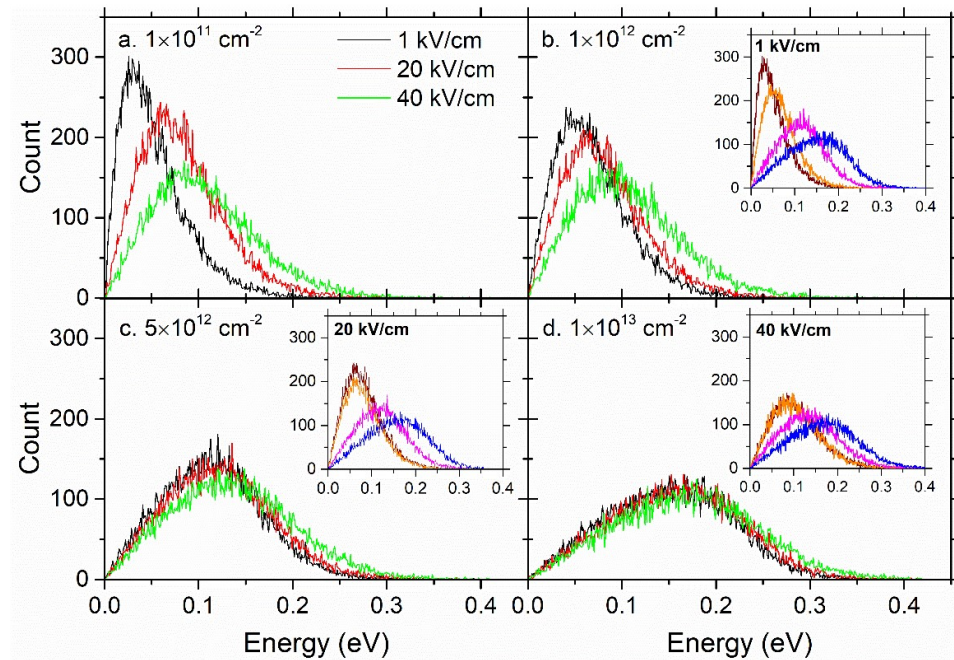


**Figure 4.15: Electron energy distribution in a suspended monolayer silicene with applied fields of 1 kV/cm, 20 kV/cm and 40 kV/cm. The distribution was simulated with  $10^5$  particles and mesh size of 50 meV. The energy distribution is skewed to higher energy level with a higher carrier concentration due to degeneracy effect. Subplot in (b), (c) and (d) shows the same plot that overlapping 1 kV/cm, 20 kV/cm and 40 kV/cm with different carrier concentrations. Brown, orange, purple and blue refer respectively to  $1 \times 10^{11} \text{ cm}^{-2}$ ,  $1 \times 10^{12} \text{ cm}^{-2}$ ,  $5 \times 10^{12} \text{ cm}^{-2}$  and  $1 \times 10^{13} \text{ cm}^{-2}$ .**

To quantify the effects of the electric field and carrier densities on the  $k_x$  distribution, the standard deviation of  $k_x$  as a function of electric field is plotted and presented in Figure 4.16. A large standard deviation of  $k_x$  indicates a wider distribution of electron energy. For instance, at electric field 40 kV/cm, the standard deviation of  $k_x$  at carrier concentration  $1 \times 10^{11} \text{ cm}^{-2}$  is 52 % of the standard deviation at  $1 \times 10^{13} \text{ cm}^{-2}$ . As the carrier concentration goes higher, the Fermi level is pushed higher from the Dirac point. Consequently, the probability occupancy of high energy states becomes higher and hence the standard deviation of  $k_x$  becomes larger. Near zero electric field, the range of the standard deviation  $k_x$  from  $1 \times 10^{11} \text{ cm}^{-2}$  to  $1 \times 10^{13} \text{ cm}^{-2}$  is  $0.18 \text{ nm}^{-1}$  and at 40 kV/cm, the range changes to  $0.12 \text{ nm}^{-1}$ .

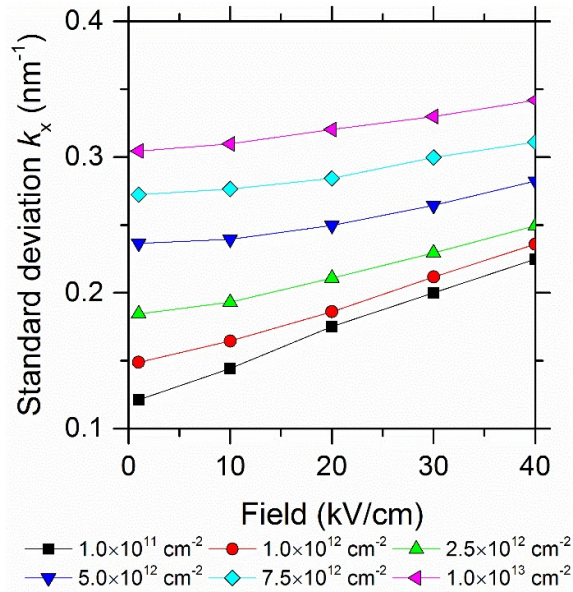


**Figure 4.16: Standard deviation of  $k_x$  against the electric field and carrier concentration for suspended monolayer silicene.**

Figure 4.17 shows the electron mobility of suspended monolayer silicene against the carrier concentration. This study found that at low carrier concentrations i.e.  $1 \times 10^{11} \text{ cm}^{-2}$ , the electron mobility is  $1104 \text{ cm}^2/\text{Vs}$ . This value is close to the reported value of  $1200 \text{ cm}^2/\text{Vs}$ , which is obtained through first-principles calculations (Li et al., 2013). As expected our value is slightly lower than  $1200 \text{ cm}^2/\text{Vs}$  as the calculations carried out in (Li et al., 2013) did not take the degeneracy effects into consideration. In consistency with graphene, silicene electron mobility reduces exponentially with higher carrier concentrations (Hirai et al., 2014). As pointed out by Hirai et al. (2014), as the carrier concentration increases, due to degeneracy effects, Fermi level is pushed further away from the Dirac point and simultaneously phonon scattering rate increases. These effects lower the electron mobility.

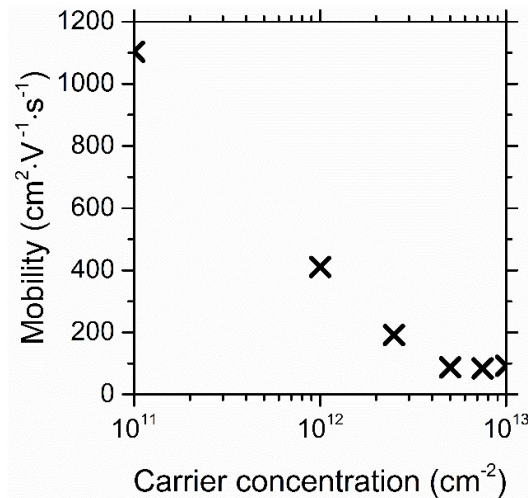


**Figure 4.17: Electron mobility of a suspended monolayer silicene as a function of carrier concentration.**

Figure 4.18 shows the comparison of electron drift velocity against the travelled distance at various electric fields and carrier concentrations. The

distance where the highest drift velocity overshoot occurs is larger with higher carrier concentrations. For example, at carrier concentration of  $1 \times 10^{13} \text{ cm}^{-2}$ , the electrons drift at a velocity higher than the steady-state value with the distance is around 47 nm, which is about 2.4 times larger compared to the case where the carrier concentration is reduced to  $1 \times 10^{11} \text{ cm}^{-2}$ . To gain further insight into this phenomenon, the mean free path of electron for the first free flight as a function of carrier concentrations were plotted.

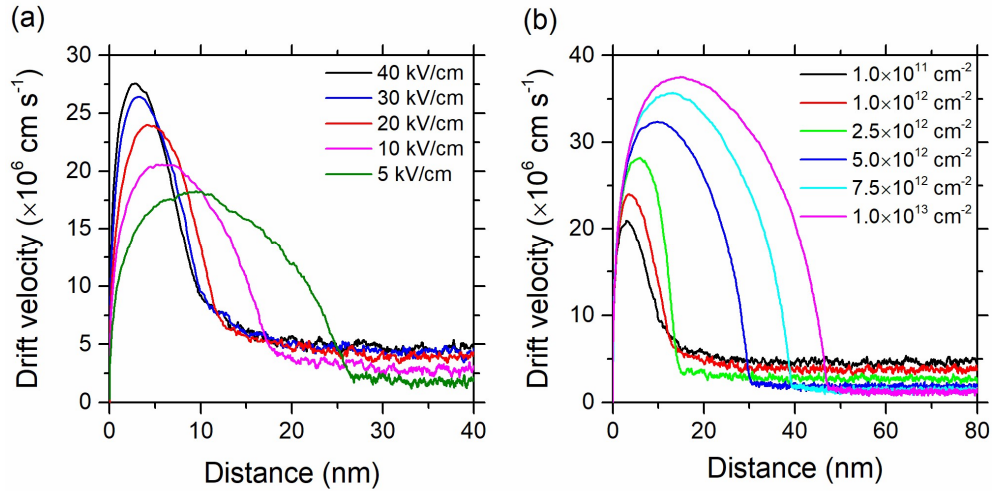


**Figure 4.18: (a) Electron drift velocity in a suspended monolayer silicene against the travelled distance for various electric fields with fixed carrier density  $1 \times 10^{12} \text{ cm}^{-2}$ . (b) Comparison of the electron drift velocities attained with carrier concentrations varied from  $1 \times 10^{11} \text{ cm}^{-2}$  to  $1 \times 10^{13} \text{ cm}^{-2}$ . The electric field is fixed at 20 kV/cm.**

Clearly, the mean free path is longer with higher carrier concentrations as illustrated in Figure 4.19. Recall that in the previous discussions, the electron energy increases with carrier concentration but phonon scattering tends to reduce the electron drift velocity. Within the mean free path region, electrons

gain energy from the electric field and experience no scattering event. Therefore, the drift velocity overshoot in Figure 4.18 (b) is higher with larger carrier concentrations. This tells that the transport characteristic is actually ballistic as what has been suggested by Ong, Rees and David (2003). Furthermore, in the cone-like band structure near the Dirac point, a large carrier concentration will lead to more electrons populate at higher energy states. This implies that more energetic electrons can response to the applied electric field initially and attaining higher speed, thus contribute to higher peak of transient velocity.

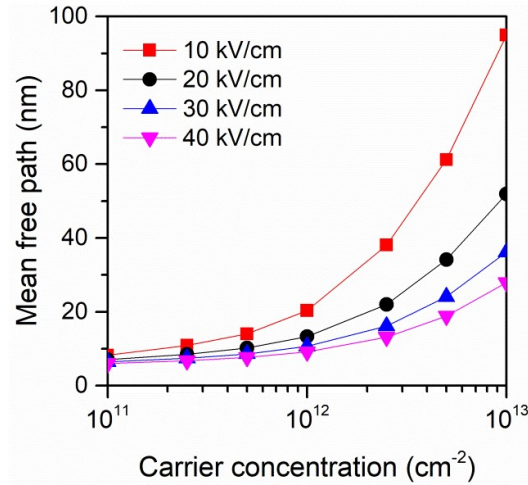


**Figure 4.19: Electron mean free path of suspended monolayer silicene against the carrier concentrations for various applied electric fields.**

Figure 4.20 (a) shows the instantaneous drift velocity with carrier concentration of  $1 \times 10^{12} \text{ cm}^{-2}$  at various electric fields and Figure 4.20 (b) shows the instantaneous drift velocity at different applied electric fields with carrier concentration of  $1 \times 10^{12} \text{ cm}^{-2}$ . Drift velocity overshoot is clearly observed at all tested applied fields. The duration of drift velocity overshoot is prolonged at lower electric fields up to 0.2 picoseconds at 2 kV/cm. During the initial

transport phase, electrons obtained its energy from the applied electric field with minimum phonon scattering and the electron drift velocity can reach a peak value of  $15 \times 10^6$  cm/s at 2 kV/cm. As expected, the drift velocity overshoot is higher with higher carrier concentrations, which is shown in Figure 4.20 (b). Similarly, the duration of drift velocity overshoot is longer with higher carrier concentrations and thereafter becomes smaller as the carrier concentration decreases. The presence of high drift velocity overshoot can be beneficial to the silicene based FETs for high frequency switching applications (Kaneko et al., 2014; Vali, Dideban and Moezi, 2016).

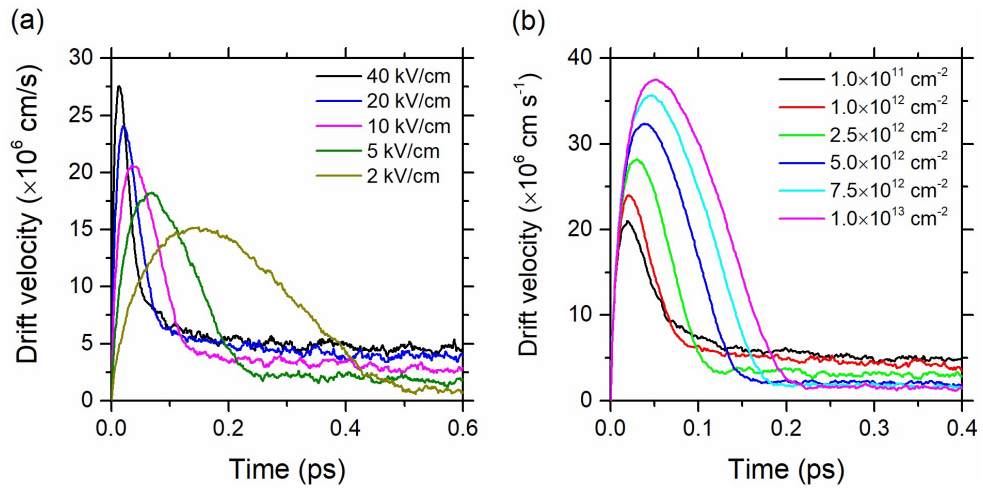


**Figure 4.20: Time evolution of instantaneous drift velocity of suspended monolayer silicene with (a) carrier concentration of  $1 \times 10^{12}$  cm<sup>-2</sup> (b) carrier concentrations varied from  $1 \times 10^{11}$  cm<sup>-2</sup> to  $1 \times 10^{13}$  cm<sup>-2</sup> with fixed electric field at 20 kV/cm.**

## 4.5 Summary

A systematic study on the effects of carrier densities on the charge transport properties in suspended graphene and silicene was presented. An ensemble semi-classical analytical band Monte-Carlo model was developed for the purpose of these studies. For both graphene and silicene, increasing the carrier concentration will suppress the steady-state drift velocity due to the synergistic effects of degeneracy and the dependency of the scattering rate and electron energy. Overall, the steady-state drift velocity with the same carrier concentration and applied field for graphene is higher than that of silicene. The electron mobility of graphene is 3-order of magnitude higher than silicene. This is expected because in comparison to silicene, graphene has lower coupling in optical and acoustic out-of-plane (ZA and ZO) scatterings. Additionally, due to the low coupling of ZA and ZO modes, the mean free path for graphene is larger than silicene. For example, at carrier concentrations of  $1 \times 10^{13} \text{ cm}^{-2}$ , the mean free path for graphene is 6 times longer than that of silicene. This feature makes graphene an excellent candidate for electron devices that require ballistic electron transport.

## CHAPTER 5

### TERAHERTZ SIGNAL GENERATION IN TWO-DIMENSIONAL MATERIALS

#### 5.1 Introduction

Graphene has been looked up as a potential candidate to replace silicon especially for producing high speed devices due to its stability in room temperature and high carrier mobility (Novoselov et al., 2004). Graphene is a unique material with linear band structure near the K point. Here, the band structure can be viewed as two cones touching at the Dirac point. Experimental work has shown that suspended graphene has a very high electron mobility i.e.  $> 10^5 \text{ cm}^2/\text{Vs}$  (Bolotin et al., 2008) and the electron mobilities are in the order of  $10^4 \text{ cm}^2/\text{Vs}$  and  $10^5 \text{ cm}^2/\text{Vs}$  when it is deposited on top of  $\text{SiO}_2$  and h-BN substrates, respectively (Hirai et al., 2014). This has a huge advantage in developing high speed devices which utilize ballistic electron transport. Graphene based field-effect transistors (FETs) have been experimentally demonstrated to operate in radio frequency (Andersson, Zhang and Stake, 2016; Generalov et al., 2016; Hu et al., 2014). With this, graphene has been an active research material in the area of high speed electronics. The ability of solid state devices to generate THz radiation has been experimentally and theoretically demonstrated (Nakajima and Hangyo, 2004; Reklaitis, 2006; Ascazubi et al., 2006; Zhu et al., 2013; Dragoman, Dinescu and Dragoman, 2016). Previous

works have shown that graphene is capable of operating in THz region using photo-excited carriers (Meric et al., 2008; Li et al., 2015; Parmentier et al., 2016). Having a similar linear band structure, silicene also garners some interest from researchers. Electrons in silicene have been reported to reach drift velocity of  $3.8 \times 10^7$  cm/s (Abidin et al., 2017). However, research in silicene based electronic devices is not widely reported.

## 5.2 Device Structure and Simulation Approach

In this work, the concept of quasi-ballistic electron reflections (QBER) proposed by Ong and Hartnagel (2007; 2008; 2015) is applied on a suspended monolayer of graphene and silicene to explore possibility of these materials in generating THz signal. The QBER effect is implemented by having electrons moving back and forth in a potential well powered by an external AC bias. The energy diagram for QBER devices is shown in Figure 5.1. Well length is taken with consideration to be longer than the calculated mean free path of the materials.

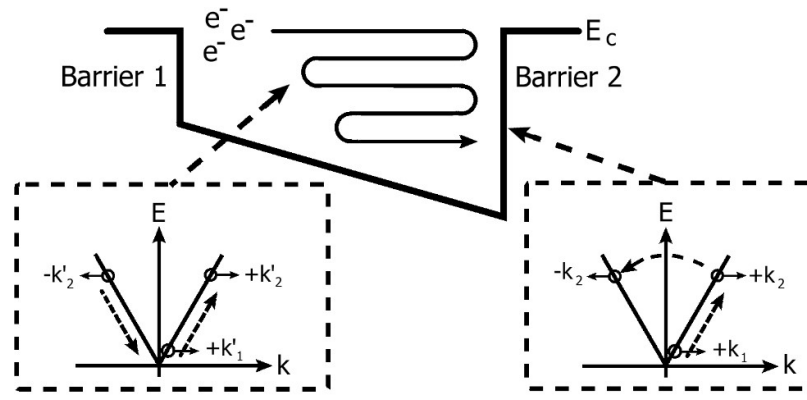


**Figure 5.1: Schematic diagram of the quasi-ballistic electrons experiencing multiple reflection at the potential barriers.**

To simulate the QBER in the two-dimensional materials, the electron will be confined in a potential well where alternating bias is applied across it. A one-dimensional (1D) self-consistent Monte Carlo model coupled with a Poisson solver is developed to study the QBER effects in graphene and silicene. The Monte Carlo code takes into the consideration of intrinsic optical and acoustic phonon scatterings as highlighted in Chapter 3. Pauli exclusion principle is incorporated in the QBER model using the rejection technique as proposed by Lugli and Ferry (1985). All reflections at the barrier will be treated as elastic and the Klein tunnelling through the barrier is neglected to evaluate only the electron reflection resonance. All simulations were performed at 300 K with a total duration of 240 ps. The 240 ps is selected because the duration is long enough for the electron to reached a steady-state as shown in Figure 4.11 and Figure 4.20 where current form is stable at every potential cycle. On that note, examining the simulation beyond 240 ps does not further improve the obtained results. The charge transport parameters used in the QBER model for graphene and silicene is similar to those presented in Chapter 3 Table 3.1.

The first part of the simulation is focused on suspended monolayer graphene where the device is excited using square-wave and sinusoidal potentials. Next, the possibility of generating THz signal using silicene is explored where only square wave potential is applied. No visible oscillation appeared using sinusoidal potential on silicene due physical properties of silicene that already explained in Chapter 4.4 and further explained in Chapter 5.4.

### 5.3 Graphene Based Structure

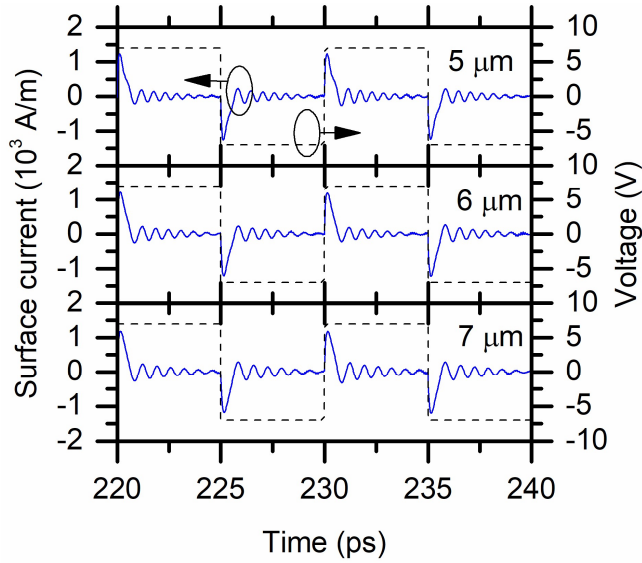
From the simulation in Chapter 4, the range of applied field applicable to the graphene AMC model is up to 20 kV/cm at room temperature. In this work, the device length is varied and for each case a square wave or sinusoid potential is applied across the device. The frequency for both of the excitations signal is fixed at 100 GHz. The radiation frequencies for different device lengths are calculated and analysed.

The simulation is done with a space interval  $dx$  of 1 nm, where 100 super-particles are assigned within each  $dx$ . The time interval for each simulation is 1 fs and initial condition for doped carrier concentration is  $1 \times 10^{12}$  cm<sup>-2</sup> for graphene which near to its intrinsic value (Castro Neto et al., 2009). The thickness for the monolayer graphene is 3.4 Å (Lee et al., 2008) while the relative permittivity for the monolayer graphene is taken as 2.35 (Hwang et al., 2012).

#### 5.3.1 Square Wave Bias Excitation

Figure 5.2 shows the current oscillation in a suspended monolayer graphene when a square-wave potential is applied across it. The device length is varied from 5 μm to 7 μm. During the first-half cycle of the square-wave signal, electrons are accelerated by the external electric field from one end of the energy barrier to another which results in a peak transient current of ±1200 A/m. The electrons are reflected at the opposing energy barrier and travel in the

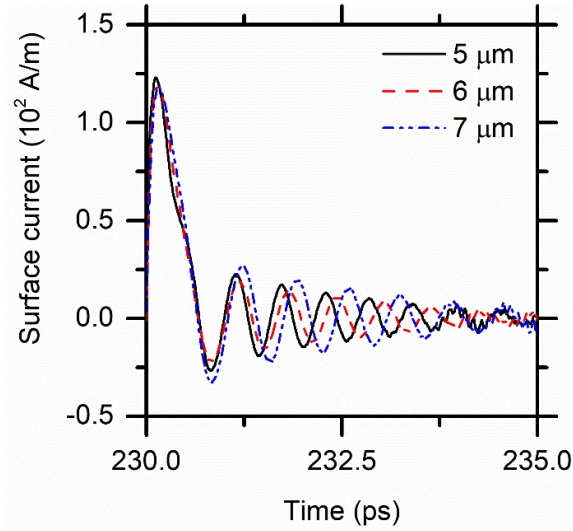
direction against the applied electric field. This phenomenon can be observed in Figure 5.2 where the current has a negative value. The electrons oscillates back and forth between the two energy barriers and gradually, their energy is reduced due to phonon scattering. Eventually, the current dies-off after 4 ps to 5 ps, indicating the electrons momentum are fully randomized and in equilibrium condition. The whole process is repeated again during the second-half cycle of the AC signal.



**Figure 5.2: Blue lines indicate the temporal evolution of electron current under  $\pm 7$  V square wave bias (black dotted line) at switching frequency of 100 GHz. The device length is varied from 5  $\mu\text{m}$  to 7  $\mu\text{m}$ .**

To gain further insight into the current oscillation due to QBER effect, the expanded view of the instantaneous surface current for different device lengths are plotted in Figure 5.3. The excitation signal is a  $\pm 7$  V square wave. For clearer visualization, only the current response for the first-half cycle of the AC signal is shown in Figure 5.3. The transit time is less than 1 ps for the

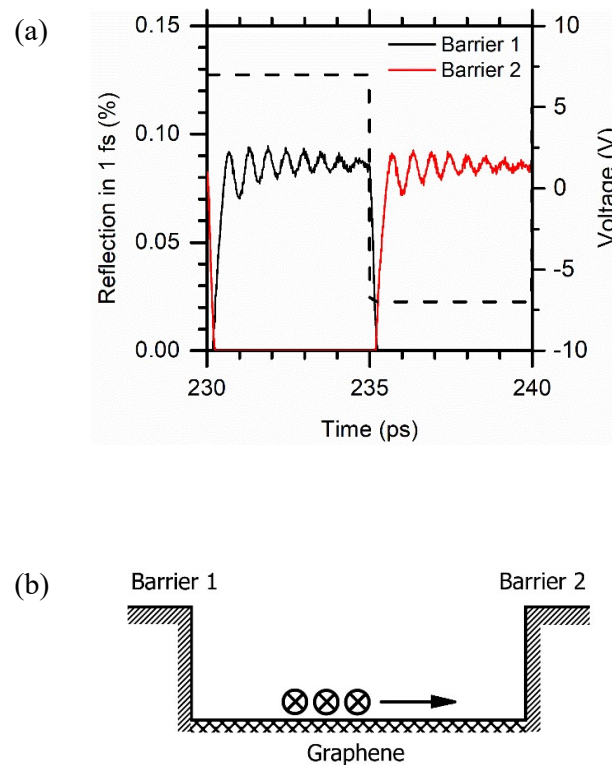
electron to reach the opposing barrier, indicating the electrons travel at a very high speed and quasi-ballistic.



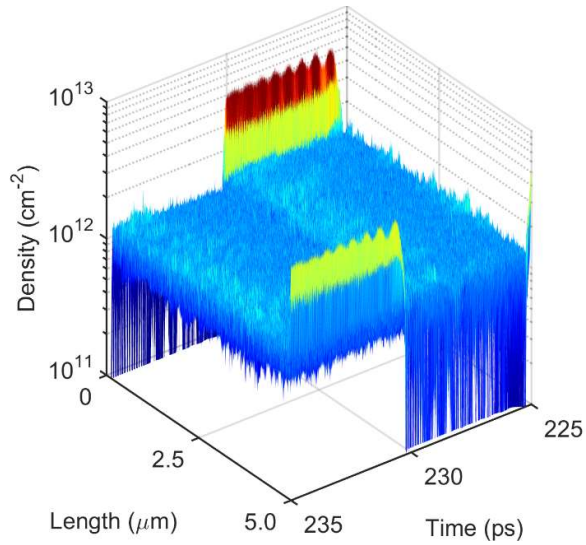
**Figure 5.3: Expanded view of the electron current oscillation in Figure 5.2 for the first-half cycle of the square-wave.**

Figure 5.4 shows the ratio of the electrons reaching the potential barrier and reflected to the total number of electrons in the device per fs. Here a 5  $\mu\text{m}$  device with  $\pm 7$  V bias is used as the representative device. During the positive cycle of the square wave, electrons are accelerated to barrier 1 (see Figure 5.4 (b) ) and travel back and forth due to quasi-ballistic reflection. This effect can clearly be observed from the oscillation of the fractional electron in Figure 5.4 (a) from 230 ps to 235 ps. When the bias changes its polarity, the electrons now move towards barrier 2. Therefore, during the second-half of the AC cycle which corresponds to the time from 235 ps to 240 ps, electrons are being reflected multiple times at barrier 2. These phenomena can also be described by a 3-dimensional (3D) plot as shown in Figure 5.5. It is worth mentioning that

not all electrons are reflected. In fact, over the time electrons will accumulate at both barriers as shown in Figure 5.5. Clearly, the electrons density at the barrier is oscillating, suggesting the electrons experience multiple reflections.



**Figure 5.4: (a) Fractional electron reflection per fs. The applied bias is  $\pm 7$  V with switching frequency 100 GHz. The device length is 5  $\mu\text{m}$ . (b) Schematic diagram of the electrons in graphene confined between two potential barriers.**



**Figure 5.5: Electron density distribution as a function of position and time propagation. The device is bias with  $\pm 7$  V square wave potential. The switching frequency is 100 GHz and the device length is 5  $\mu\text{m}$ .**

As discussed in Chapter 3, the time derivative of the electron current oscillation is proportional to the electromagnetic radiation intensity. Through Fourier transform of the auto-correlation radiation intensity, the frequency range of the radiation can be identified as given by equation 3.23. Figure 5.6 shows the radiation spectra of a graphene based QBER device. The device length is varied from 5  $\mu\text{m}$  to 7  $\mu\text{m}$ . The peak radiation frequency increases from 1.5 THz to 1.8 THz as the device length decreases from 7  $\mu\text{m}$  to 5  $\mu\text{m}$ . As the device length shrinks, its length is closer to the mean free path of the electron and furthermore the electric field becomes stronger. This results in the electrons oscillate at higher frequency, thus the radiation frequency increases.

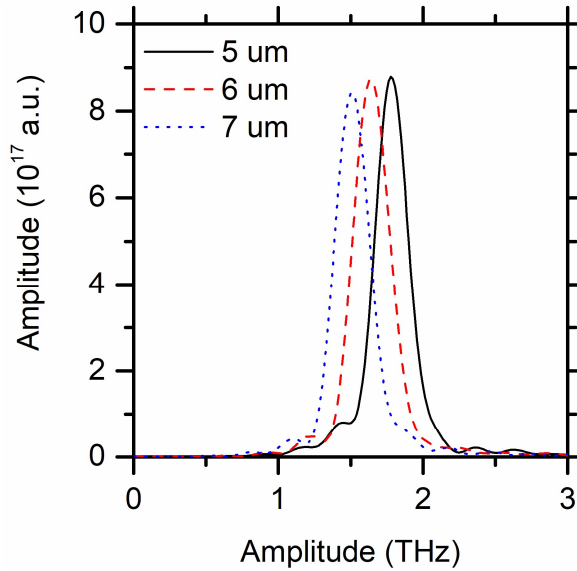


**Figure 5.6: Radiation spectra for the graphene QBER devices with  $\pm 7$  V excitation signal at switching frequency of 100 GHz.**

Patterning graphene with precise dimension maybe a challenging task. When voltage is applied across the graphene, changes in the device length or the size of the graphene can change the electric field substantially because the external electric field is inversely proportional to the device length for a fixed bias. In Figure 5.7, the peak radiation frequency is plotted against the different device lengths under different applied biases. All of the peak radiations frequency are above 1 THz. The peak radiation frequency decreases as the device length increases. When the device bias is  $\pm 7$  V, the radiation frequency can be controlled from 1.23 THz to 1.78 THz by reducing the device length from 10  $\mu\text{m}$  to 5  $\mu\text{m}$ . For a smaller device, the electrons only need to travel a shorter distance before reaching the opposing barrier. During this period of time, they encounter less phonon scattering and hence their energies are preserved,

allowing them to oscillate faster. Additionally, as the device length getting shorter, its length is closer to the electron mean free path.

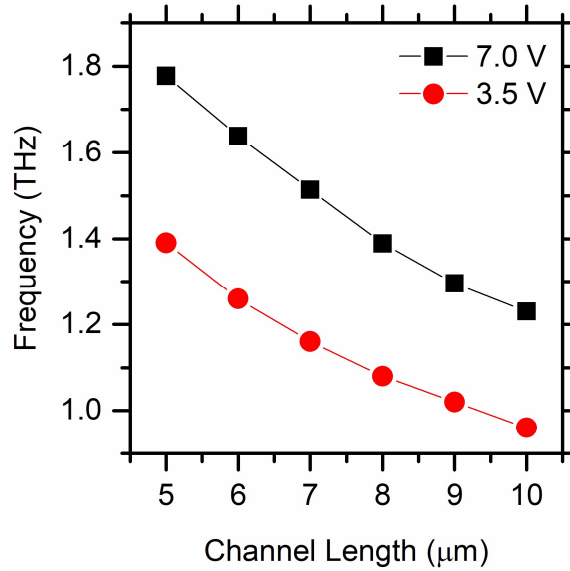


**Figure 5.7: Peak radiation frequency against device length at different bias.**

Further reduction of the potential bias to 3.5 V results in smaller peak radiation frequency. At this applied bias, the peak radiation frequency can be tuned from 0.96 THz to 1.39 THz. This reduction in frequency is correlated with the relationship between the radiation frequency and the device length. This is easily understandable because as the electric field decreases, naturally the electrons become less energetic thus reduces the oscillation frequency. It is also important to note that at 20 kV/cm, the average electrons energy is still less than 1 eV. In other words, the energy dispersion of graphene is still in the linear regime of Dirac cone, hence the accuracy of the simulations should not be affected.

### 5.3.2 Sinusoidal Wave Bias Excitation

For practical application, the generation of high frequency perfect square wave signal is challenging. Hence, sinusoid signal is often used as the AC signal. Figure 5.8 shows the current oscillation in device with active region of  $5\ \mu\text{m}$ ,  $6\ \mu\text{m}$  and  $7\ \mu\text{m}$  lengths when a  $\pm 10\ \text{V}_p$  ( $7\ \text{V}_{\text{rms}}$ ) sinusoidal potential is applied. Similar to the square-wave excitation, the electrons are accelerated towards the opposing energy barrier, reflected and travel against the external applied field induced by the first-cycle of the sinusoid wave. The electrons move back and forth and losses energy gradually due to phonons scattering and eventually the current dies-off. The electrons oscillate again in the same manner in second-cycle of the AC signal. Peak transient current density between  $-600\ \text{A/m}$  to  $600\ \text{A/m}$  can be observed for all cases, as shown in Figure 5.8.

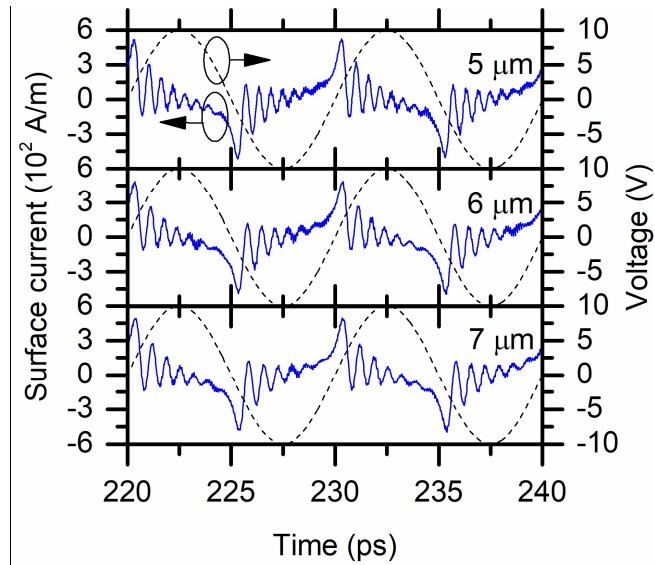


**Figure 5.8:** Blue lines indicate the temporal evolution of electron current under  $\pm 10\ \text{V}_p$  ( $7\ \text{V}_{\text{rms}}$ ) sinusoid potential (black dotted line) at switching frequency of  $100\ \text{GHz}$ . The device length is varied from  $5\ \mu\text{m}$  to  $7\ \mu\text{m}$ .

Figure 5.9 shows the expanded view of the instantaneous surface current density in Figure 5.9 for the first-half cycle of the sinusoid bias. The transit time of the electrons to travel to the opposing energy barrier is in the range of 1 ps, indicating the electron transport is quasi-ballistic. As expected, the electron current attenuates over time as they oscillate, indicating the electron energies reduced due to phonon scattering.

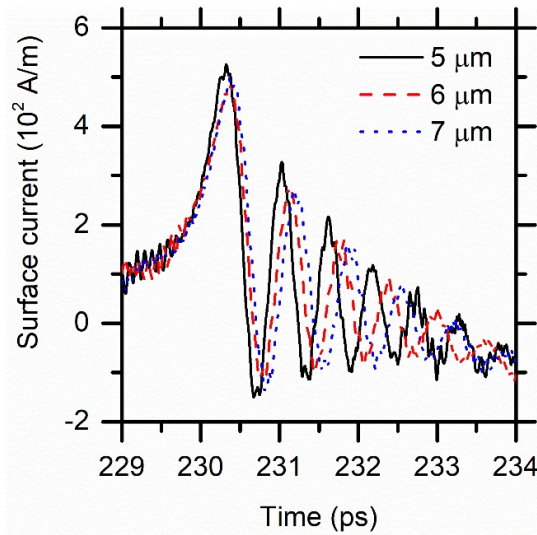


**Figure 5.9: Expanded view of the electron current oscillation in Figure 5.8 for the first-half cycle of the sinusoid bias.**

The ratio of the electrons reaching the potential barrier and reflected to the total number of electrons per fs is plotted in Figure 5.10. In Figure 5.10, a 5  $\mu\text{m}$  device with a  $\pm 10$   $V_p$  sinusoidal excitation signal is used as the representative device. In contrast to the square wave excitation, the fractional electron reaching the energy barrier per fs increases steadily up to 0.11 % at 232.5 ps and thereafter reduces to zero for the first cycle of the sinusoid

excitation signal. This result is expected because in the sinusoid signal, the potential increases over time, reaching a peak value and then reduces to zero again. Therefore, the percentage of electrons reaching the potential barrier naturally will follow the sinusoidal form. Within the sinusoid profile, the oscillation of the fractional electron is still visible, suggesting the electrons travel back and forth between two energy barriers.

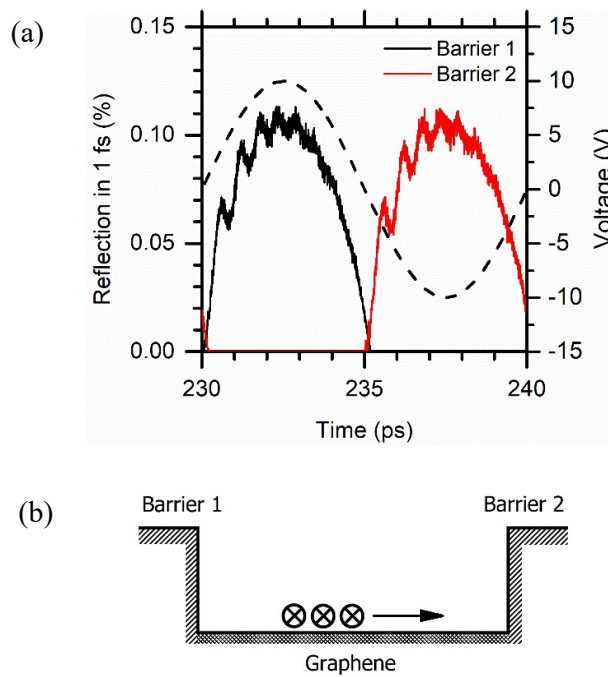


**Figure 5.10: (a) Fractional electron reflection per fs. The applied bias is  $\pm 10 V_p$  ( $10V_{rms}$ ) sinusoid signal with switching frequency of 100 GHz. The device length is  $5 \mu m$ . (b) Schematic diagram of the electrons in graphene confined between two potential barriers.**

A 3D plot of the electron density against position and propagation time is shown in Figure 5.11 for a  $5 \mu m$  device. Electron accumulation occurs at both ends of the energy barrier, suggesting not all electrons are reflected at these

barriers. Similar to those square-wave excitation, electron density fluctuates at the potential barriers which is a good indication the electrons experience multiple reflections. However, in this case the electron density fluctuations follow the sinusoid profile.

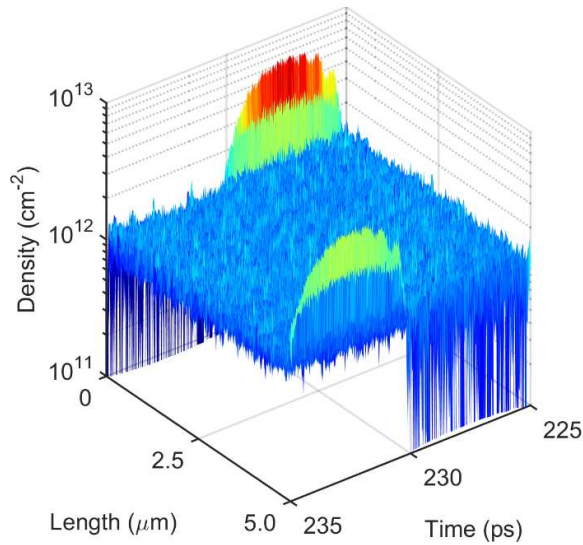


**Figure 5.11: Electron density distribution as a function of position and propagation time. The device is bias with  $\pm 10 V_p$  ( $10V_{rms}$ ) sinusoid signal. The switching frequency is 100 GHz and the device length is 5  $\mu m$ .**

The radiation spectra of the QBER devices are shown in Figure 5.12. The device length is varied from 5  $\mu m$  to 7  $\mu m$ . All peak radiation frequencies are above 1 THz. This shows that the QBER is a promising method in producing THz signal radiation. Following the same trend with those using square wave as excitation signal, the radiation frequency increases as the device length becomes smaller. The peak radiation frequency increase from 1.3 THz to 1.6 THz as device length decrease from 7  $\mu m$  to 5  $\mu m$ . As discuss previously, this effect is attributed to the higher electric field which enable the electrons to

oscillate at higher frequency. Additionally, with shorter device, its length is closer to the electron mean free path.

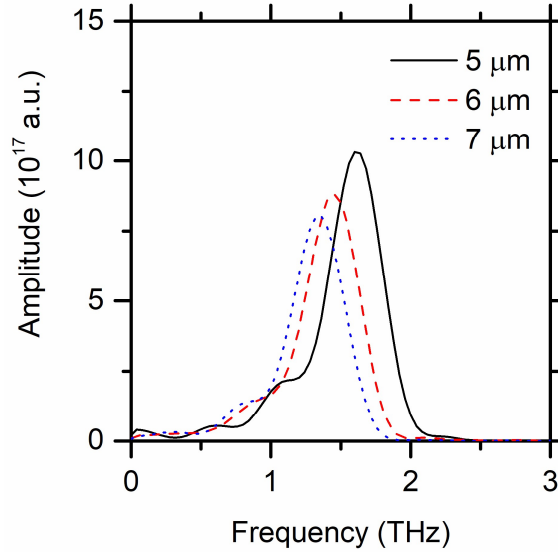


**Figure 5.12: Radiation spectra for the graphene QBER devices with  $\pm 10 V_p$  ( $7 V_{rms}$ ) excitation signal at switching frequency of 100 GHz.**

Figure 5.13 shows the peak radiation frequency from devices action region varied from 5  $\mu m$  to 10  $\mu m$ . The radiation frequency can be controlled from 1.12 (0.92) THz to 1.60 (1.32) THz when the device length is reduced from 10  $\mu m$  to 5  $\mu m$  at  $V_{rms}$  of 7 V (3.5V). Increasing the sinusoidal peak voltage is akin to increasing the external applied electric field. Therefore, the electrons energy increases and consequently this increases the radiation frequency. As explained in previous discussions, a shorter device length results in less phonon scattering encountered by the electrons when they transit across the potential well, thus the electrons energy is better conserved over the time. Overall, the

electrons energy is less than 1 eV which is still within the Dirac cone of the graphene. This indicates that the Monte Carlo code used here is still applicable.

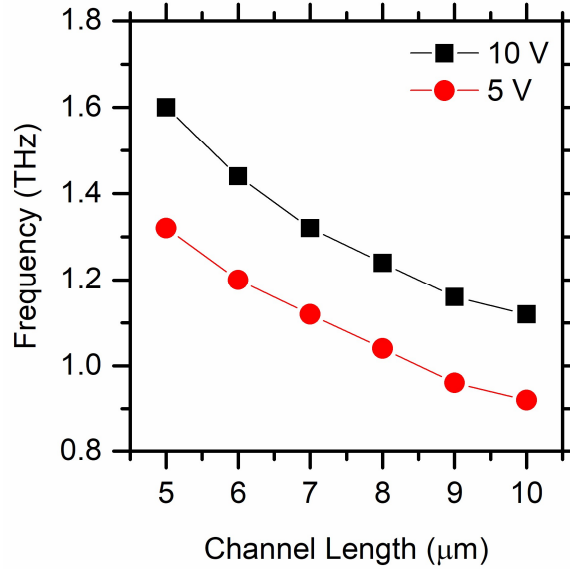


**Figure 5.13: Peak radiation frequency against device length at different bias.**

#### 5.4 Silicene Based Structure

The silicene device structure is similar to that of graphene. However, the device length used is shorter i.e. 50 nm to 200 nm since silicene mean free path is in the range of 10 nm with doped carrier concentration of  $1 \times 10^{11} \text{ cm}^{-2}$ . Consistent with the graphene based devices, the switching frequency of the silicene devices are fixed at 100 GHz. The simulation is done with a space interval  $dx$  of 0.1 nm, where 100 super-particles are assigned within each  $dx$ . The time interval for each simulation is 1 fs and initial condition for carrier concentration is  $8 \times 10^9 \text{ cm}^{-2}$  for silicene (Tao et al., 2015). The thickness for

monolayer silicene is 4.0 Å (Tao et al., 2015) and the dielectric constant is 34.33 (Mohan, Kumar and Ahluwalia, 2014).

#### 5.4.1 Square Wave Bias Excitation

The current density of the silicene based QBER device under the influence of  $\pm 0.2$  V square-wave switching frequency of 100 GHz is shown in Figure 5.14. In contrast to the graphene-based devices, it is not necessary to have the device length in the  $\mu\text{m}$  regime since the electron mean free path for silicene is less than 10 nm for carrier density  $1 \times 10^{11} \text{ cm}^{-2}$ . In fact, experimentally, the intrinsic carrier density of silicene was measured to be around  $8 \times 10^9 \text{ cm}^{-2}$  only (Tao et al., 2015). Therefore, the device length in Figure 5.14 is varied from 50 nm to 200 nm.

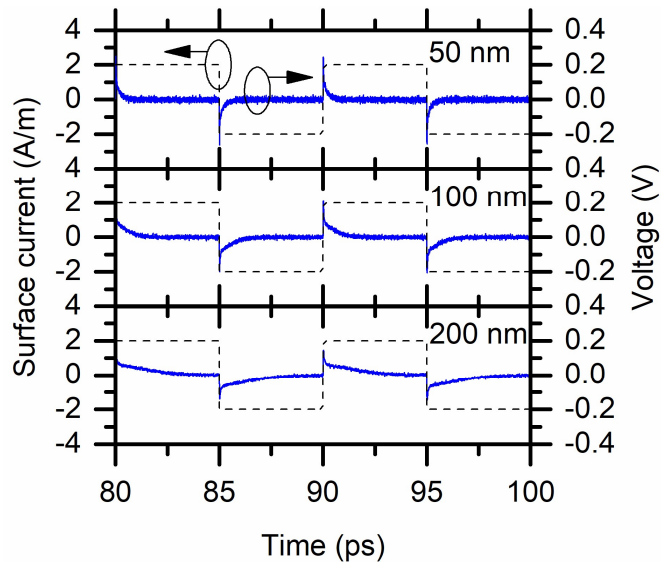


**Figure 5.14: Blue lines indicate the temporal evolution of electron current under  $\pm 0.2$  V square wave bias (black dotted line) at switching frequency of 100 GHz. The device length is varied from 50 nm to 200 nm.**

While in graphene-based devices electron oscillation can be observed clearly, in silicene based device for each cycle of the square wave, the electron current experienced overshoot and thereafter it degrades rapidly. This is because silicene has higher scattering rate compared to graphene. Additionally, silicene has a very significant out-of-plane mode phonon scattering (*ZA* and *ZO*) mode which is negligible for the case of graphene (Borysenko et al., 2010). Furthermore, the electron mean free path for silicene is at least 10 times lower than that of graphene as discussed in Chapter 4. Peak overshoot current density up to 2.4 A/m is observed for each case as illustrated in Figure 5.14.

Figure 5.15 shows the ratio of the electrons reaching the potential barrier and reflected to the total number of electrons in the device per fs. Device with 100 nm length is used as the representative device. The device is biased with  $\pm 0.2$  V square-wave at frequency of 100 GHz. Unlike graphene devices, the fractional electrons reaching the barrier does not show any oscillation over time instead it increases gradually then saturates at 2 %. This observation suggests that the electrons tend to accumulate at the opposing barrier. When the bias polarity is switched, the electrons will accelerate to the opposing barrier and accumulate there with minimum speed. A 3D plot showing the electron density as a function of the simulation time and position is illustrated in Figure 5.16.

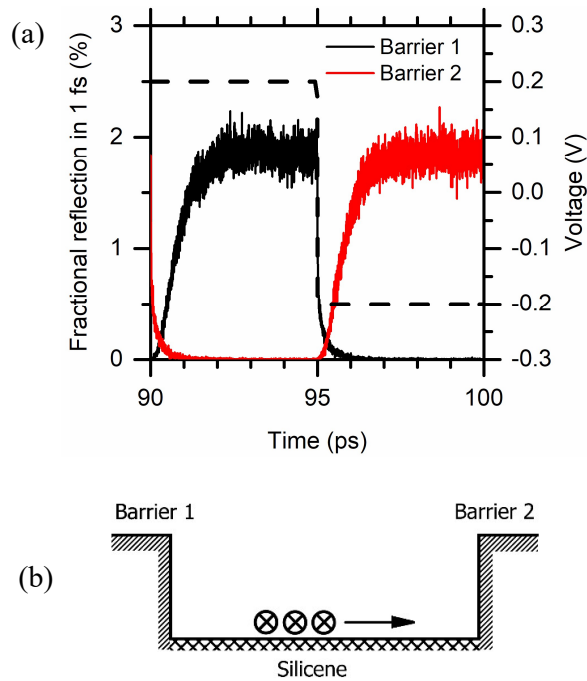


**Figure 5.15: (a) Fractional electron reflection per fs. The applied bias is  $\pm 0.2$  V square-wave with switching frequency of 100 GHz. The device length is 100 nm. (b) Schematic diagram of the electrons in silicene confined between two potential barriers.**

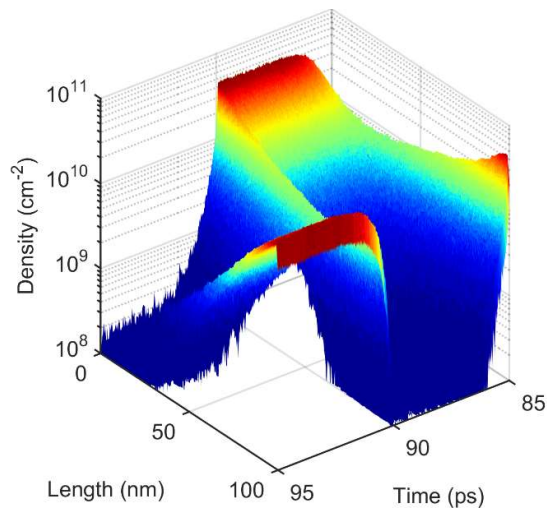


**Figure 5.16: Electron density distribution as a function of position and propagation time. The device is biased with  $\pm 0.2$  V. The switching frequency is 100 GHz and the device length is 100 nm.**

The device structure and bias conditions of Figure 5.16 are similar to those in Figure 5.15. The 3D plot clearly indicates the electron density tends to concentrate at one end of the energy barrier during the first-half cycle of the square wave and then move to the opposing barrier during the second-half cycle.

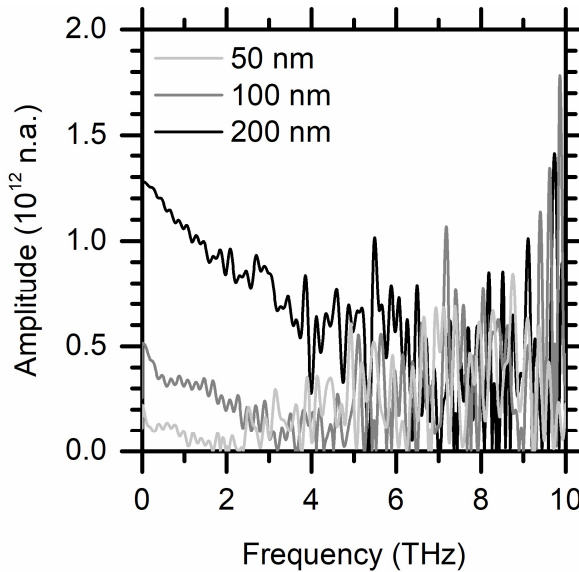


**Figure 5.17: Radiation spectra of the silicene based devices at different device lengths.**

Figure 5.17 shows the radiation spectra of the silicene devices with device length of 50 nm, 100 nm and 200 nm. All the devices are biased with  $\pm 0.2$  V square-wave with switching frequency of 100 GHz. The radiation spectra is noisy with no obvious peak radiation. In fact the amplitude of the radiation is at least 5 order lower compared to the radiation generated using graphene based devices. It is clear, THz radiation is not present. These results suggest unlike graphene, silicene is not a suitable material to be used to generate THz radiation based on QBER effect. This is attributed to the high scattering rate and a short electron mean free path of silicene. Both of these features results

in the electrons losing energy rapidly as they travel across the barrier, thus unable to oscillate upon the excitation of external bias. Note that the mean free path of silicene is an order lower than that of InGaAs (Thathachary et al., 2014) and 10 times smaller than that of graphene. Mobility of InGaAs is also 10 times higher than that of silicene (Oliver et al., 1981) where it has been shown that InGaAs can produce THz radiation via QBER effect (Ong and Hartnagel, 2007).

## 5.5 Summary

Simulation shows that graphene is a promising 2D material in generating THz signal using QBER effect due to the long mean free path and low phonon scattering rate. It was found that the THz frequency can be tuned by controlling the graphene length and the applied bias. Reducing the graphene length and increasing the applied bias are the key strategies in achieving higher radiation frequency. By varying the device length from 5  $\mu\text{m}$  to 10  $\mu\text{m}$ , the frequency of the THz radiation can be tuned from 0.92 THz to 1.32 THz by using a 3.5  $V_{\text{rms}}$  sinusoid signal with 100 GHz switching frequency. Further increment of the  $V_{\text{rms}}$  to 7  $V_{\text{rms}}$  will enhance the frequency of the radiation by 20 %. With shorter device and higher bias, the device length is closer to the electron mean free path and at the same time the electrons become more energetic. These combined effects allow the electrons to oscillate faster between the two-energy barriers, thus producing higher radiation frequency. In contrast, the studies in this work reveal that silicene is not a suitable material to generate THz signal using QBER approach due to its short mean free path (i.e. 10 times smaller than graphene) and high phonon scattering rate which could result in the electrons losing energy

rapidly. The accumulation and depletion of electrons on the energy barrier follows the switching frequency of the excitation bias. These properties can be further explored towards the development of high frequency switching device.

## CHAPTER 6

### CONCLUSIONS AND RECOMMENDATIONS

#### 6.1 Conclusions

In this dissertation, an AMC model is developed to investigate the electron transport properties of two low dimensional materials i.e. a free-standing monolayer graphene and silicene. The AMC model is known capable of replicating the results from full band Monte Carlo (FMC) simulations with good accuracy and faster computational time. The applicability of this model is validated against the FMC results in terms of the steady-state electron transport characteristics. The degeneracy effects induced by the carrier concentrations on the electron transport properties are taken into consideration by introducing rejection routine into the Monte Carlo framework. The Monte Carlo simulations only considered low energy carrier transport where the electrons energies are within the linear energy dispersion near the Dirac point.

This study shows that as the carrier concentration in graphene and silicene increases, the steady-state drift velocity degrades due to the degeneracy effects which force the electrons occupy higher energy states further away from the Dirac Point. It is well known that the phonon scattering for these materials increases with energy. This combined effect reduces the electron drift velocity and its mobility. Compared to graphene, the silicene mobility is at least 16 times

lower for all the tested carrier concentrations. This behaviour is attributed to the low Fermi velocity of silicene and silicene possess high ZA/ZO mode phonon scattering which is negligible in graphene. Furthermore, the simulation results show that the electron mean free path for silicene increases with the carrier concentrations for a given applied electric field. Following the same trend, for graphene, the electron mean free path is electric field and carrier concentrations dependent. However, the mean free path for graphene increases at a slower rate with carrier concentrations. As expected, due to the low phonon scattering and high Fermi velocity, the mean free path for graphene is at least an order higher than that of silicene. From the transient simulation, drift velocity overshoot is clearly present in both graphene and silicene. During the initial transport, the phonon scattering is minimum, and electrons gain energy from the electric field. Hence the electron drift velocity is able to reach a peak value of  $15 \times 10^6$  cm/s and  $9.1 \times 10^7$  cm/s at 2 kV/cm for silicene and graphene, respectively. For both cases, the duration of drift velocity is extended with higher carrier concentrations.

The AMC model is modified to incorporate a Poisson solver in order to explore the possibility of using graphene and silicene in generating THz radiation through QBER effect. A simple device consists of graphene or silicene sandwiched between two wide bandgap materials that serve as energy barrier is used to demonstrate this effect. Upon the excitation of an AC signal, the electrons in the potential well oscillate back and forth between the two energy barrier, generating current oscillations thus resulting in radiation of THz signals. Using  $7 V_{\text{rms}}$  sinusoid signal with switching frequency of 100 GHz, the radiation

frequency can be controlled from 1.12 THz to 1.60 THz by varying the device length from 5  $\mu\text{m}$  to 10  $\mu\text{m}$ . Unlike graphene, it is found that silicene is not a suitable material to be used to generate THz radiation using QBER effect. The electrons tend to accumulate at the potential barrier during each cycle of the AC bias. This is caused by the low electron mobility, short mean free path and high scattering rate of silicene which results in the electrons energy degrade rapidly and the electron unable to oscillate in the potential well.

## **6.2 Future Works**

Present work can be extended in following ways:

1. Present work only considers a free-standing graphene and silicene. It is undeniable that 2D materials need to be supported by a substrate for practical applications. Future work can be done by incorporating the effect of substrate into the Monte Carlo model. The presence of substrate is expected to further reduce the electron mobility of material due to surface phonon scattering and charge impurity present in the substrate. Previous works have shown that the Fermi velocity of graphene and silicene may change when they are deposited on different substrates (Hwang et al., 2012). This effect needs to be taken into consideration when developing the Monte Carlo model.
2. Other physical effects such as electron-electron scattering, chiral tunnelling and the surface impurity of silicene and graphene can be taken into consideration into the Monte Carlo model to mimic the actual

physical properties of those materials. It is worth to investigate how these effects can influence the frequency of the THz radiation that generated from QBER.

3. The generation of THz using QBER as discussed relies on electron confinement in a potential well. In fact, electron confinement was demonstrated with epitaxial graphene grown on SiC substrate (Berger et al., 2006). Another experimental results also shown that graphene nanoribbon bandgap is inversely proportional to its width (Han et al., 2007). For future work, graphene nanoribbon with different widths can be used as a new structure to demonstrate the QBER effect towards the generation of THz signal.
  
4. One of the important aspects in evaluating THz radiation is the output power. Previously, Schildbach et al. (2016) developed an equivalent circuit model to estimate the output power of a QBER based device. Similarly, present work can be extended to develop an equivalent circuit model to calculate the power conversion efficiency and thus the output power of the graphene based QBER device.

## REFERENCES

Abidin, B.I., Yeoh, K.H., Ong, D.S. and Yong, T.K., 2017. Effects of carrier concentrations on the charge transport properties in monolayer silicene. *Journal of Physics D: Applied Physics*, 50(425103), 6pp.

Abidin, B.I., Yeoh, K.H., Yong, T.K. and Ong, D.S., 2017. THz radiation in graphene based on quasi-ballistic electron reflection. *2017 IEEE Asia Pacific Conference on Postgraduate Research in Microelectronics and Electronics (PrimeAsia)*, 31 October – 2 November 2017 Kuala Lumpur, Malaysia. IEEE Xplore, pp. 13-16.

Ahmed, I.S., Ashama, M.D. and Phillips, A.H., 2018. Spin-valleytronics of Silicene Based Nanodevices (SBNs). *Journal of Magnetism and Magnetic Materials*, 456, pp. 199-203.

Andersson, M.A., Zhang, Y. and Stake, J., 2016. A 185–215-GHz subharmonic resistive graphene FET integrated mixer on silicon. *IEEE Transactions on Microwave Theory and Techniques*, 65(1), pp. 165-172.

Ares, P., Palacios, J.J., Abellán, G., Herrero, J.G. and Zamora, F., 2017. Recent progress on antimonene: a new bidimensional material. *Advanced Materials*, 30(1703771), 27pp.

Armstrong, C.M., 2012, The truth about terahertz, 17 August, [Online], Available: <http://spectrum.ieee.org/aerospace/military/the-truth-about-terahertz> [2016 September 8].

Asada, M. and Suzuki, S., 2011. Terahertz oscillators using electron devices - an approach with resonant tunneling diodes. *IEICE Electronics Express*, 8, pp. 1110-1126.

Asada, M., Suzuki, S. and Kishimoto, N., 2008. Resonant tunneling diodes for sub-terahertz and terahertz oscillators. *Japanese Journal of Applied Physics*, 47(6), pp. 4375-4384.

Ascazubi, R., Wilke, I., Kim, K.J. and Dutta, P., 2006. Terahertz emission from GaInSb. *Physical Review B*, 74(075223), 5pp.

Aufray, B., Kara, A., Vizzini, S., Oughaddou, H., Léandri, C., Ealet, B. and Lay, G.L., 2010. Graphene-like silicon nanoribbons on Ag(110): a possible formation of silicene. *Applied Physics Letters*, 96(183102), 3pp.

Bampoulis, P., Zhang, L., Safaei, A., Gastel, R.v., Poelsema, B. and Zandvliet, H.J.W., 2014. Germanene termination of Ge<sub>2</sub>Pt crystals on Ge(110). *Journal of Physics: Condensed Matter*, 26(442001), 5pp.

Barker, R.J., 2005. Modern microwave and millimeter-wave power electronics, 1st ed., United States: Wiley-IEEE Press.

Berger, C., Song, Z., Li, X., Wu, X., Brown, N., Naud, C., Mayou, D., Li, T., Hass, J., Marchenkov, A.N., Conrad, E.H., First, P.N. and Heer, W.A.d., (2006). Electronic Confinement and Coherence in Patterned Epitaxial Graphene. *Science*, 312(5777), pp. 1191-1196.

Bolotin, K.I., Sikes, K.J., Jiang, Z., Klima, M., Fudenberg, G., Hone, J., Kim, P. and Stormer, H.L., 2008. Ultrahigh electron mobility in suspended graphene. *Solid State Communications*, 146(9-10), pp. 351-355.

Booske, J.H., 2008. Plasma physics and related challenges of millimeter wave to terahertz and high power microwave generation. *Physics of Plasmas*, 15(055502), 16pp.

Booske, J.H., Dobbs, R.J., Joye, C.D., Kory, C.L., Neil, G.R., Park, G.S., Park, J. and Temkin, R.J., 2011. Vacuum electronic high power terahertz sources. *IEEE Transactions on Terahertz Science and Technology*, 1(1), pp. 54-75.

Borowik, P., Thobel, J.L. and Adamowicz, L., 2016. Monte Carlo studies of low - field electron transport in monolayer silicene and graphene. *Physica Status Solidi (a)*, 213(11), pp. 2916-2920.

Borowik, P., Thobel, J.L. and Adamowicz, L., 2016. Monte Carlo study of electron transport in monolayer silicene. *Semiconductor Science and Technology*, 31(115004), 11pp.

Borowik, P., Thobel, J.L. and Adamowicz, L., 2017. Modified Monte Carlo method for study of electron transport in degenerate electron gas in the presence of electron–electron interactions, application to graphene. *Journal of Computational Physics*, 341, pp. 397-405.

Borowik, P., Thobel, J.L. and Adamowicz, L., 2017. Monte Carlo study of electron relaxation in graphene with spin polarized, degenerate electron gas in presence of electron-electron scattering. *Semiconductor Science and Technology*, 32(125006), 4pp.

Borysenko, K.M., Mullen, J.T., Barry, E.A., Paul, S., Semenov, Y.G., Zavada, J.M., Nardelli, M.B. and Kim, K.W., 2010. First-principles analysis of electron-phonon interactions in graphene. *Physical Review B*, 81(121412), 4pp.

Brandstetter, M., Kainz, M.A., Zederbauer, T., Krall, M., Schönhuber, S., Detz, H., Schrenk, W., Andrews, A.M., Strasser, G. and Unterrainer, K., 2016. InAs based terahertz quantum cascade lasers. *Applied Physics Letters*, 108(011109), 4pp.

Bresciani, M., Palestri, P., Esseni, D. and Selmi, L., 2010, Simple and efficient modeling of the E-k relationship and low-field mobility in graphene nanoribbons. *Solid State Electronics*, 54(9), pp. 1015-1021.

Cardona, M. and Pollak, F.H., 1966. Energy-band structure of germanium and silicon: the  $k \cdot p$  method. *Physical Review*, 142(2), pp. 530-543.

Carr, G.L., Martin, M.C., McKinney, W.R., Jordan, K., Neil, G.R. and Williams, G.P., 2002. High-power terahertz radiation from relativistic electrons. *Nature*, 420, pp. 153-156.

Castro Neto, A.H., Guinea, F., Peres, N.M.R., Novoselov, K.S. and Geim, A.K., 2009. The electronic properties of graphene. *Reviews of Modern Physics*, 81(109), 55pp.

Chauhan, J. and Guo, J., 2009. High-field transport and velocity saturation in graphene. *Applied Physics Letter*, 95(023120), 3 pp.

Chen, J.H., Jang, C., Xiao, S., Ishigami, M. and Fuhrer, M.S., 2008. Intrinsic and extrinsic performance limits of graphene devices on SiO<sub>2</sub>. *Nature Nanotechnology*, 3, pp. 206-209.

Chen, M.X., Zhong, Z. and Weinert, M., 2016. Designing substrates for silicene and germanene: first-principles calculations. *Physical Review B*, 94(075409), 6pp.

Cohen, M.L. and Chelikowsky, J.R., 1989. *Electronic structure and optical properties of semiconductors*, 75th ed., Berlin, Heidelberg: Springer.

Crouch, R.K., Debnam, W.J. and Fripp, A.L., 1978. Properties of GaN grown on sapphire substrates. *Journal of Materials Science*, 13, pp. 2358-2364.

Das Sarma, S., Adam, S., Hwang, E.H. and Rossi, E., 2011. Electronic transport in two-dimensional graphene. *Reviews of Modern Physics*, 83(2), pp. 407-470.

David, J.K., Register, L.F. and Banerjee, S.K., 2012. Semiclassical Monte Carlo analysis of graphene FETs. *IEEE Transactions on Electron Devices*, 59(4), pp. 976-982.

Deacon, D.A.G., Elias, L.R., Madey, J.M.J., Ramian, G.J., Schwettman, H.A. and Smith, T.I., 1977. First operation of a free-electron laser. *Physical Review Letters*, 38(16), pp. 892-894.

Dhillon, S.S., Vitiello, M.S., Linfeld, E.H., Davies, A.G., Hoffmann, M.C., Booske, J., Paoloni, C., Gensch, M., Weightman, P., Williams, G.P., Castro-Camus, E., Cumming, D.R.S., Simoens, F., Escorcia-Carranza, I., Grant, J., Lucyszyn, S. and Kuwata-Gonokami, M., 2017. The 2017 terahertz science and technology roadmap. *Journal of Physics D: Applied Physics*, 50(143001), 49pp.

Dragoman, M., Dinescu, A. and Dragoman, D., 2016. Room temperature on-wafer ballistic graphene field-effect-transistor with oblique double-gate. *Journal of Applied Physics*, 119(244305), 6pp.

Dragoman, M., Dragoman, D., Deligiorgis, G., Konstantinidis, G., Neculoiu, D., Cismaru, A. and Plana, R., 2009. Current oscillations in a wide graphene sheet. *Journals of Applied Physics*, 106(044312), 4pp.

Drut, J.E. and Lähde, T.A., 2013. Velocity Renormalization in Graphene From Lattice Monte Carlo. 31st International Symposium on Lattice Field Theory LATTICE 2013, Mainz, Germany.

Ducournau, G., Szriftgiser, P., Beck, A., Bacquet, D., Pavanello, F., Peytavit, E., Zaknune, M. and Akalin, T., 2014. Ultrawide-bandwidth single-channel 0.4-thz wireless link combining broadband quasi-optic photomixer and coherent detection. *IEEE Transactions on Terahertz Science and Technology*, 4(3), pp. 328-337.

Du, X., Skachko, I., Barker, A. and Andrei, E.Y., 2008. Approaching ballistic transport in suspended graphene. *Nature Nanotechnology*, (3), pp. 491-495.

Ezawa, M., 2013. Spin Valleytronics in Silicene: Quantum spin hall–quantum anomalous hall insulators and single-valley semimetals. *Physical Review B*, 87(155415), 6pp.

Fang, T., Konar, A., Xing, H. and Jena, D., 2011. High-field transport in two-dimensional graphene. *Physical Review B*, 84(125450), 7 pp.

Fang, T., Konar, A., Xing, H. and Jena, D., 2007. Carrier statistics and quantum capacitance of graphene sheets and ribbons. *Applied Physics Letters*, 91(092109), 3pp.

Fatholouloumi, S., Dupont, E., Chan, C.W.I., Wasilewski, Z.R., Laframboise, S.R., Ban, D., Mátyás, A., Jirauschek, C., Hu, Q. and Liu, H.C., 2012. Terahertz quantum cascade lasers operating up to  $\sim 200$  k with optimized oscillator strength and improved injection tunneling. *Optic Express*, 20(4), pp. 3866-3876.

Feng, B., Ding, Z., Meng, S., Yao, Y., He, X., Cheng, P., Chen, L. and Wu, K., 2012. Evidence of silicene in honeycomb structures of silicon on Ag(111). *Nano Letters*, 12(7), pp. 3507-3511.

Fleurence, A., Friedlein, R., Ozaki, T., Kawai, H., Wang, Y. and Yamada-Takamura, Y., 2012. Experimental evidence for epitaxial silicene on diboride thin films. *Physical Review Letters*, 108(245501), 5pp.

Fuhrer, M.S., Chun, N.L. and MacDonald, A.H., 2010. Graphene: materially better carbon. *MRS Bulletin*, 35(4), pp. 289-295.

Gaddemane, G., Vendenberghe, W.G., Put, M.L.V.d., Chen, E. and Fischetti, M.V., 2018. Monte-Carlo study of electronic transport in non- $\sigma$ -symmetric two-dimensional materials: silicene and germanene. *Journal of Applied Physics*, 124(044306), 8 pp.

Gelmont, B., Kim, K. and Shur, M., 1993. Monte Carlo simulation of electron transport in gallium nitride. *Journal of Applied Physics*, 74(1818), 4pp.

Generalov, A.A., Andersson, M.A., Yang, X. and Stake, J., 2016. Optimization of THz graphene FET detector integrated with a bowtie antenna. *2016 10th European Conference on Antennas and Propagation (EuCAP)*, 10 - 15 April 2016 Davos, Switzerland, IEEE Xplore, pp. 1-3

Guzman-Verri, G.G. and Lew Yan Voon, L.C., 2007. Electronic structure of silicon-based nanostructures. *Physical Review B*, 76(075131), 10pp.

- Hangyo, M., 2015. Development and future prospects of terahertz technology. *Japanese Journal of Applied Physics*, 54(120101), 16pp.
- Han, M.Y., Özyilmaz, B., Zhang, Y. and Kim, P., 2007. Energy band-gap engineering of graphene nanoribbons. *Physical Review Letters*, 98(206805), 4pp.
- Harada, N., Awano, Y., Sato, S. and Yokoyama, N., 2011. Monte Carlo simulation of electron transport in a graphene diode with a linear energy band dispersion. *Journal of Applied Physics*, 109(104509), 7pp.
- Harada, N., Ohfuti, M. and Awano, Y., 2008. Performance estimation of graphene field-effect transistors using semiclassical Monte Carlo simulation. *Applied Physics Express*, 1(024002), 3pp.
- Harrison, W.A., 2012. *Electronic structure and the properties of solids: the physics of the chemical bond*, 1st ed., New York: Dover Publications.
- Hauri, C.P., Ruchert, C., Vicario, C. and Ardana, F., 2011. Strong-field single-cycle THz pulses generated in an organic crystal. *Applied Physics Letters*, 99(161116), 3 pp.
- Hebling, J., Almási, G., Kozma, I.Z. and Kuhl, J., 2002. Velocity matching by pulse front tilting for large-area THz-pulse generation. *Optic Express*, 10(21), pp. 1161-1166.
- Hess, K., 1981. Ballistic electron transport in semiconductor. *IEEE Transaction on Electron Devices*, 28(8), pp. 937-940.
- Hirai, H., Tsuchiya, H., Kamakura, Y., Mori, N. and Ogawa, M., 2014. Electron mobility calculation for graphene on substrates. *Journal of Applied Physics*, 116(083703), 6pp.
- Houssa, M., Dimoulas, A. and Molle, A., 2015. Silicene: a review of recent experimental and theoretical investigations. *Journal of Physics: Condensed Matter*, 27(253002), 19pp.
- Hu, Z., Sinha, D.P., Lee, J.U. and Liehr, M., 2014. Substrate dielectric effects on graphene field effect transistors. *Journal of Applied Physics*, 115(194507), 6pp.

Hwang, C., Siegel, D.A., Mo, S.K., Regan, W. and Ismach, A., 2012. Fermi velocity engineering in graphene by substrate modification. *Scientific Reports*, 2(590), 4pp.

Iijima, S., 1991. Helical microtubules of graphitic carbon. *Nature*, 354(1), pp. 56-58.

Intel Corporation, 2017, *Intel Support* [Online]. Available at: <https://www.intel.com/content/www/us/en/support/articles/000005725/network-and-i-o/wireless-networking.html> [Accessed: 16 July 2018].

Ishibashi, T., Muramoto, Y., Yoshimatsu, T. and Ito, H., 2014. Unitraveling-carrier photodiodes for terahertz applications. *IEEE Journal of Selected Topics in Quantum Electronics*, 20(6), 10pp.

Ito, H., Nakajima, F., Furuta, T. and Ishibashi, T., 2005. Continuous THz-wave generation using antenna-integrated uni-travelling-carrier photodiodes. *Semiconductor Science and Technology*, 20(7), pp. S191-S198.

Jazbinsek, M., Mutter, L. and Gunter, P., 2008. Photonic applications with the organic nonlinear optical crystal DAST. *IEEE Journal of Selected Topics in Quantum Electronics*, 14(5), pp. 1298-1311.

Jose, D. and Datta, A., 2012. Understanding of the buckling distortions in silicene. *The Journal of Physical Chemistry C*, 116(46), pp. 24639–24648.

Jose, D. and Datta, A., 2014. Structures and chemical properties of silicene: unlike graphene. *Accounts of Chemical Research*, 47(2), pp. 593-602.

Kamal, C. and Ezawa, M., 2015. Arsenene: Two-dimensional buckled and puckered honeycomb arsenic systems. *Physical Review B*, 91(185423), 10pp.

Kane, E.O., 1956. Energy band structure in p-type germanium and silicon. *Journal of Physics and Chemistry of Solids*, 1(1-2), pp. 82-99.

Kaneko, S., Tsuchiya, H., Kamakura, Y., Mori, N. and Ogawa, M., 2014. Theoretical performance estimation of silicene, germanene, and graphene nanoribbon field-effect transistors under ballistic transport. *Applied Physics Express*, 7(035102), 4pp.

Kang, S., Kim, D., Urteaga, M. and Seo, M., 2017. State of the art THz integrated circuits in InP HBT technologies. *2017 IEEE International*

*Symposium on Radio-Frequency Integration Technology (RFIT)*, 30 August – 1 September 2017 Seoul, South Korea. IEEE Xplore, pp. 25-27.

Kim, U., Kim, I., Park, Y., Lee, K.Y., Yim, S.Y., Park, J.G., Ahn, H.G., Park, S.H. and Choi, H.J., 2011. Synthesis of Si nanosheets by a chemical vapor deposition process and their blue emissions. *ACS Nano*, 5(3), pp. 2176-2181.

Kobylinski, M.M., Ruhmlieb, C., Kornowski, A. and Mews, A., 2018. Hexagonally shaped two-dimensional tin(ii)sulfide nanosheets: growth model and controlled structure formation. *The Journal of Physical Chemistry C*, 122(10), pp. 5784–5795.

Koenig, S.P., Doganov, R.A., Schmidt, H., Castro Neto, A.H. and Özyilmaz, B., 2014. Electric field effect in ultrathin black phosphorus. *Applied Physics Letters*, 104(103106), 4pp.

Köhler, R., Tredicucci, A., Beltram, F., Beere, H.E., Linfield, E.H., Davies, A.G., Ritchie, D.A., Iotti, R.C. and Rossi, F., 2002. Terahertz semiconductor-heterostructure laser. *Nature*, 417, pp. 156-159.

Kroto, H.W., Heath, J.R., O'Brien, S.C., Curl, R.F. and Smalley, R.E. (1985) 'C60: buckminsterfullerene. *Nature*, 318(1), pp. 162-163.

Kukita, K. and Kamakura, Y., 2013. Monte Carlo simulation of phonon transport in silicon including a realistic dispersion relation. *Journal of Applied Physics*, 114(154312), 8pp.

Kurosawa, K., 1966. Monte Carlo calculation of hot electron problems. *Journal of the Physical Society of Japan*, 21, pp. 424-426.

Lay, G.L., 2015. 2D materials: silicene transistors. *Nature Nanotechnology*, 10(1), pp. 202-203.

Lee, C., Wei, X., Kysar, J.W. and Hone, J., 2008. Measurement of the elastic properties and intrinsic strength of monolayer graphene. *Science*, 321(5887), pp. 385-388.

Lew Yan Voon, L.C., Lopez-Bezanilla, A., Wang, J., Zhang, Y. and Willatzen, M., 2015. Effective hamiltonians for phosphorene and silicene. *New Journal of Physics*, 17(025004), 10pp.

Lew Yan Voon, L.C., Sandberg, E., Aga, R.S. and Farajian, A.A., 2010. Hydrogen compounds of group-IV nanosheets. *Applied Physics Letters*, 97(163114), 3pp.

Lewis, R.A., 2014. A review of terahertz sources. *Journal of Physics D: Applied Physics*, 14(374001), 4pp.

Li, X., Barry, E.A., Zavada, J.M., Nardelli, M.B. and Kim, K.W., 2010. Surface polar phonon dominated electron transport in graphene. *Applied Physics Letters*, 97(232105), 3pp.

Li, X., Borysenko, K.M., Nardelli, M.B. and Kim, K.W., 2011. Electron transport properties of bilayer graphene. *Physical Review B*, 84(195453), 4pp.

Li, X., Mullen, J.T., Jin, Z., Borysenko, K.M., Nardelli, M.B. and Kim, K.W., 2013. Intrinsic electrical transport properties of monolayer silicene and MoS<sub>2</sub> from first principles. *Physical Review B*, 87(115418), 9pp.

Li, Q., Tian, Z., Zhang, X., Singh, R., Du, L., Gu, J. and Han, J., 2015. Active graphene-silicon hybrid diode for terahertz waves. *Nature Communications*, 6(7082), 6pp.

Liu, W.C. (1990) 'Investigation of electrical and photoluminescent properties of MBE-grown Al<sub>x</sub>Ga<sub>1-x</sub>As layers. *Journals of Materials Science*, 25(3), pp. 1765-1772.

Liu, S., 2018. High peak power THz source for ultrafast electron diffraction. *AIP Advances*, 8(015029), 6pp.

Liu, C., Feng, W. and Yao, Y., 2011. Quantum spin hall effect in silicene and two-dimensional germanium. *Physical Review Letters*, 107(176802), 4pp.

Lugli, P. and Ferry, D.K. (1985) 'Degeneracy in the ensemble Monte Carlo method for high field transport in semiconductor. *IEEE Transaction on Electron Devices*, 32(11), pp. 2431-2437.

Ma, J., Karl, N.J., Bretin, S., Ducournau, G. and Mittleman, D.M., 2017. Frequency-division multiplexer and demultiplexer for terahertz wireless links. *Nature Communications*, 8(729), 8pp.

Mak, K.F., Lee, C., Hone, J., Shan, J. and Heinz, T.F., 2010. Atomically thin MoS<sub>2</sub>: a new direct-gap semiconductor. *Physical Review Letters*, 105(136805), 4pp.

Meric, I., Han, M.Y., Young, A.F., Ozyilmaz, B., Kim, P. and Shepard, K.L., 2008. Current saturation in zero-bandgap, top-gated graphene field-effect transistors. *Nature Nanotechnology*, 3, pp. 654 – 659.

Mittleman, D.M., 2018. Twenty years of terahertz imaging [Invited]. *Optic Express*, 26(8), 15pp.

Mohan, B., Kumar, A. and Ahluwalia, P.K., 2014. Electronic and dielectric properties of silicene functionalized with monomers, dimers and trimers of B, C and N atoms. *RSC Advances*, 4(60), pp. 31700-31705.

Mortazavi, B., Rahaman, O., Makaremi, M., Dianat, A., Cuniberti, G. and Rabczuk, T., 2016. First-principles investigation of mechanical properties of silicene. *Physica E: Low-dimensional Systems and Nanostructures*, 87, pp. 228-232.

Muller, A.S., 2010. Accelerator-based sources of infrared and terahertz radiation, *Reviews of Accelerator Science and Technology*, 3(1), pp. 165-183.

Nagatsuma, T., Ducournau, G. and Renaud, C.C., 2016. Advances in terahertz communications accelerated by photonics. *Nature Photonics*, 10, pp. 371-279.

Nakajima, M. and Hangyo, M. (2004) 'Study of THz radiation from semiconductor surfaces excited by femtosecond laser pulses under laser illumination. *Semiconductor Science and Technology*, 19(4), 4pp.

Nakano, H., Mitsuoka, T., Horibuchi, M.H., Nozaki, H., Takahashi, N., Nonaka, T., Seno, Y. and Nakamura, H., 2016. Soft synthesis of single-crystal silicon monolayer sheets . *Angewandte Chemie*, 45(38), pp. 6303-6306.

Novoselov, K.S., Geim, A.K., Morozov, S.V., Jiang, D., Katsnelson, M.I., Grigorieva, I.V., Dubonos, S.V. and Firsov, A.A., 2005. Two-dimensional gas of massless dirac fermions in graphene. *Nature*, 438, pp. 197-200.

Novoselov, K.S., Geim, A.K., Morozov, S.V., Jiang, D., Zhang, Y., Dubonos, S.V., Grigorieva, I.V. and Firsov, A.A. (2004) 'Electric field effect in atomically thin carbon films. *Science*, 306(5696), pp. 666-669.

Oliver, J.D., Eastman, L.F., Kirchner, P.D. and Schaff, W.J., 1981. Electrical characterization and alloy scattering measurements of LPE  $\text{Ga}_x\text{In}_{1-x}\text{As}/\text{InP}$  for high frequency device applications. *Journal of Crystal Growth*, 54(1), pp. 64-68.

Ong, D.S. and Hartnagel, H.L., 2007. Generation of THz signals based on quasi-ballistic electron reflections in double-heterojunction structures. *Semiconductor Science and Technology*, 22(9), pp. 981-987.

Ong, D.S. and Hartnagel, H.L., 2008. Enhanced THz frequency multiplier efficiency by quasi-ballistic electron reflection in double-heterojunction structures. *Europhysics Letters*, 81(48004), 6pp.

Ong, D.S. and Hartnagel, H.L., 2015. THz radiation by quasi-ballistic electron reflection in  $\text{AlSb}/\text{InAs}/\text{AlSb}$  heterostructures. *Europhysics Letters*, 109(38004), 6pp.

Ong, D.S., Rees, G.J. and David, J.P.R. (2003) 'Avalanche speed in thin avalanche photodiodes. *Journal of Applied Physics*, 93(4232), 8pp.

Parmentier, F.D., Serkovic-Loli, L.N., Roulleau, P. and Glatli, D.C., 2016. Photon-assisted shot noise in graphene in the terahertz range. *Physical Review Letters*, 116(227401), 5pp.

Pearsall, T., Piskorski, M., Brochet, A. and Chevrier, J., 1981. A  $\text{Ga}_{0.47}\text{In}_{0.53}\text{As}/\text{InP}$  heterophotodiode with reduced dark current. *IEEE Journal of Quantum Electronics*, 17(2), pp. 255-259.

Qin, R., Wang, C.H., Zhu, W. and Zhang, Y., 2012. First-principles calculations of mechanical and electronic properties of silicene under strain. *AIP Advances*, 2(022159), 6pp.

Quhe, R.G., Wang, Y.Y. and Lü, J., 2015. Silicene transistors - a review. *Chinese Physics B*, 24(088105), 11pp.

Rahman, A., Rahman, A.K., Yamamoto, T. and Kitagawa, H., 2016. Terahertz sub-nanometer sub-surface imaging of 2D materials. *Journal of Biosensors & Bioelectronics*, 7(3), pp. 1-8.

Ramo, S., 1939. Currents induced by electron motion. *Proceedings of the IRE*, 27(9), pp. 584-585.

Reis, F., Li, G., Dudy, L., Bauernfiend, M., Glass, S., Hanke, W., Thomale, R., Schaefer, J. and Claessen, R., 2017. Bismuthene on a SiC substrate: a candidate for a high-temperature quantum spin hall material. *Science*, 357(6348), pp. 287-290.

Reklaitis, A., 2006. Monte Carlo analysis of terahertz oscillations of photoexcited carriers in GaAs. *Physical Review B*, 74(239903), 9pp.

Rengela, R., Pascual, E. and Martín, M.J., 2014. Influence of the substrate on the diffusion coefficient and the momentum relaxation in graphene: the role of surface polar phonons. *Applied Physics Letters*, 104(233107), 4 pp.

Rengel, R., Couso, C. and Martin, M.J., 2013. A Monte Carlo study of electron transport in suspended monolayer graphene. *2013 Spanish Conference on Electron Devices (CDE)*, 12 – 14 February 2013 Valladolid, Spain. IEEE Xplore, pp. 175-178.

Rengel, R., Iglesias, J.M., Hamham, E.M. and Martin, M.J., 2018. Damping of acoustic flexural phonons in silicene: damping of acoustic flexural phonons in silicene. *Semiconductor Science and Technology*, 33(6), 10 pp.

Rengel, R. and Martín, M.J., 2013. Diffusion coefficient, correlation function, and power spectral density of velocity fluctuations in monolayer graphene. *Journal of Applied Physics*, 114(143702), 9 pp.

Rieh, J.S., Jeon, S. and Kim, M., 2011. An overview of integrated THz electronics for communication applications. *2011 IEEE 54th International Midwest Symposium on Circuits and Systems (MWSCAS)*, 7 – 10 August 2011 Seoul, South Korea. IEEE Xplore, pp. 1-4.

Rode, D.L., 1971. Electron transport in InSb, InAs, and InP. *Physical Review B*, 3(10), pp. 3287-3299.

Roman, R.E. and Cranford, S.W., 2014. Mechanical properties of silicene. *Computational Materials Science*, 82, pp. 50-55.

Schildbach, C., Ong, D.S., Hartnagel, H. and Schmidt, L.P., 2016. Estimation of frequency conversion efficiency of thz devices using a ballistic electron wave swing circuit model. *Semiconductor Science and Technology*, 31(065003), 7pp.

Seifert, T., Jaiswal, S., Sajadi, M., Jakob, G., Winnerl, S., Wolf, M., Kläui, M. and Kampfrath, T., 2017. Ultrabroadband single-cycle terahertz pulses with

peak fields of  $300 \text{ kV cm}^{-1}$  from a metallic spintronic emitter. *Applied Physics Letters*, 110(252402), 5pp.

Sell, A., Leitenstorfer, A. and Huber, R., 2008. Phase-locked generation and field-resolved detection of widely tunable terahertz pulses with amplitudes exceeding  $100 \text{ MV/cm}$ . *Optic Letters*, 33(23), pp. 2767-2769.

Shishir, R.S. and Ferry, D.K., 2009. Velocity saturation in intrinsic graphene. *Journal of Physics: Condensed Matter*, 21(344201), 5pp.

Shitara, T. and Eberl, K., 1994. Electronic properties of ingap grown by solid - source molecular - beam epitaxy with a gap decomposition source. *Applied Physics Letters*, 65(3), pp. 356-358.

Shockley, W., 1938. Currents to conductors induced by a moving point charge. *Journal of Applied Physics*, 9(10), pp. 635-636.

Siddiqua, P. and O'Leary, S.K., 2018. Electron transport within the wurtzite and zinc-blende phases of gallium nitride and indium nitride. *Journal of Materials Science: Materials in Electronics*, 29(5), pp. 3511-3567.

Somogyi, K. and Pfeifer, J., 1992. Electron mobility measured in undoped InGaAs epitaxial layer grown on n-InP substrate. *Applied Physics Letters*, 61(18), pp. 2220-2221.

Song, H.J., Ajito, K., Hirata, A., Wakatsuki, A., Muramoto, Y., Furuta, T., Kukutsa, N., Nagatsuma, T. and Kado, Y., 2009. 8 Gbit/s wireless data transmission at 250 GHz. *Electronic Letters*, 45, pp. 1121-1122.

Sule, N., Willis, K.J., Hagness, S.C. and Knezevic, I., 2014. EMC/FDTD/MD simulation of carrier transport and electrodynamics in two-dimensional electron. *Journal of Computational Electronics*, 12(4), 9pp.

Suzuki, D., Oda, S. and Kawano, Y., 2016. A flexible and wearable terahertz scanner. *Nature Photonics*, 10, pp. 809-813.

Tan, Y.W., Zhang, Y., Bolotin, K., Zhao, Y., Adam, S., Hwang, E.H., Das Sarma, S., Stormer, H.L. and Kim, P., 2007. Measurement of scattering rate and minimum conductivity in graphene. *Physical Review Letters*, 99(246803), 4pp.

Tao, L., Cinquanta, E., Chiappe, D., Grazianetti, C., Fanciulli, M., Dubey, M., Molle, A. and Akinwande, D., 2015. Silicene field-effect transistors operating at room temperature. *Nature Nanotechnology*, 10, pp. 227-231.

Thathachary, A.V., Agrawal, N., Liu, L. and Datta, S., 2014. Electron transport in multigate  $\text{In}_x\text{Ga}_{1-x}\text{As}$  nanowire FETs: from diffusive to ballistic regimes at room temperature. *Nano Letters*, 14(2), pp. 626-633.

Tomizawa, K., 1993. *Numerical simulation of submicron semiconductor devices*, 1st ed. Boston: Artech House Publishers.

Tonouchi, M., 2007. Cutting-edge terahertz technology. *Nature*, 1, pp. 97-205.

Vali, M., Dideban, D. and Moezi, N., 2016. Silicene field effect transistor with high on/off current ratio and good current saturation. *Journal of Computational Electronics*, 15(1), pp. 138-143.

Vogt, P., Padova, P.D., Quaresima, C., Avila, J., Frantzeskakis, E., Asensio, M.C., Resta, A., Ealet, B. and Lay, G.L., 2012. Silicene: compelling experimental evidence for graphenelike two-dimensional silicon. *Physical Review Letters*, 108(155501), 5pp.

Wallace, P.R., 1947. The band theory of graphite. *Physical Review*, 71(1), pp. 622-634.

Xie, H., Hu, M. and Bao, H., 2014. Thermal conductivity of silicene from first-principles. *Applied Physics Letters*, 104(131906), 4pp.

Xu, N., 2018. Spin-polarized transport in multi-terminal silicene nanodevices. *Physics Letters A*, 382(4), pp. 220-223.

Xu, X., Pereira, L.F.C., Wang, Y., Wu, J., Zhang, K., Zhao, X., Bae, S., Bui, C.T., Xie, R., Thong, J.T.L., Hong, B.H., Loh, K.P., Donadio, D., Li, B. and Özyilmaz, B., 2014. Length-dependent thermal conductivity in suspended single-layer graphene. *Nature Communications*, 5(3689), 6pp.

Xu, X., Zhang, Z., Dong, J., Yi, D., Niu, J., Wu, M., Lin, L., Yin, R., Li, M., Zhou, J., Wang, S., Sun, J., Duan, X., Gao, P., Jiang, Y., Wu, X., Peng, H., Ruoff, R.S., Liu, Z., Yu, D. et al., 2017. Ultrafast epitaxial growth of metre-sized single-crystal graphene on industrial Cu foil. *Science Bulletin*, 62(15), pp. 1074-1080.

- Yang, X., Vorobiev, A., Generalov, A., Andersson, M.A. and Stake, J., 2017. A flexible graphene terahertz detector. *Applied Physics Letters*, 111(021102), 4pp.
- Yeoh, K.H., Ong, D.S., Raymond Ooi, C.H., K., Y.T. and K., L.S., 2016. Analytical band Monte Carlo analysis electron transport in silicene. *Semiconductor Science and Technology*, 31(065012), 6pp.
- Zak, A., Andersson, M.A., Bauer, M., Matukas, J., Lisauskas, A., Roskos, H.G. and Stake, J., 2014. Antenna-integrated 0.6 THz FET direct detectors based on CVD graphene. *Nano Letters*, 14(10), pp. 5834-5838.
- Zhang, Y., Tan, Y.W., Stormer, H.L. and Kim, P., 2005. Experimental observation of the quantum hall effect and Berry's phase in graphene. *Nature*, 438, pp. 201-204.
- Zhao, H., 2012. Strain and chirality effects on the mechanical and electronic properties of silicene and silicane under uniaxial tension. *Physics Letters A*, 376(46), pp. 3546-3550.
- Zhao, H., Mao, Y., Xin Mao, X.S., Xu, C., Wang, C., Zhao, H., Mao, Y., Mao, X., Shi, X., Xu, C., Wang, C., Zhang, S. and Zhou, D., 2018. Band structure and photoelectric characterization of GeSe monolayers. *Advance Function Materials*, 28(1704855), 10pp.
- Zhu, Z., Joshi, S., Grover, S. and Moddel, G., 2013. Graphene geometric diodes for terahertz rectennas. *Journal of Physics D: Applied Physics*, 46(185101), 6pp.
- Zunger, A. and Cohen, M.L., 1978. First-principles nonlocal-pseudopotential approach in the density-functional formalism: development and application to atoms. *Physical Review B*, 18(10), pp. 5449-5472.